

REPORT DOCUMENTATION PAGE			Form Approved OMB NO. 0704-0188		
<p>The public reporting burden for this collection of information is estimated to average 1 hour per response, including the time for reviewing instructions, searching existing data sources, gathering and maintaining the data needed, and completing and reviewing the collection of information. Send comments regarding this burden estimate or any other aspect of this collection of information, including suggestions for reducing this burden, to Washington Headquarters Services, Directorate for Information Operations and Reports, 1215 Jefferson Davis Highway, Suite 1204, Arlington VA, 22202-4302. Respondents should be aware that notwithstanding any other provision of law, no person shall be subject to any penalty for failing to comply with a collection of information if it does not display a currently valid OMB control number. PLEASE DO NOT RETURN YOUR FORM TO THE ABOVE ADDRESS.</p>					
1. REPORT DATE (DD-MM-YYYY) 12-10-2014		2. REPORT TYPE Ph.D. Dissertation		3. DATES COVERED (From - To) -	
4. TITLE AND SUBTITLE Hydrodynamic and Mass Transport Properties of Microfluidic Geometries			5a. CONTRACT NUMBER W911NF-11-1-0161		
			5b. GRANT NUMBER		
			5c. PROGRAM ELEMENT NUMBER 206022		
6. AUTHORS Thomas F. Leary			5d. PROJECT NUMBER		
			5e. TASK NUMBER		
			5f. WORK UNIT NUMBER		
7. PERFORMING ORGANIZATION NAMES AND ADDRESSES Research Foundation CUNY - The City Col 160 Convent Avenue New York, NY 10031 -9101			8. PERFORMING ORGANIZATION REPORT NUMBER		
9. SPONSORING/MONITORING AGENCY NAME(S) AND ADDRESS (ES) U.S. Army Research Office P.O. Box 12211 Research Triangle Park, NC 27709-2211			10. SPONSOR/MONITOR'S ACRONYM(S) ARO		
			11. SPONSOR/MONITOR'S REPORT NUMBER(S) 58975-EG-REP.9		
12. DISTRIBUTION AVAILABILITY STATEMENT Approved for public release; distribution is unlimited.					
13. SUPPLEMENTARY NOTES The views, opinions and/or findings contained in this report are those of the author(s) and should not be construed as an official Department of the Army position, policy or decision, unless so designated by other documentation.					
14. ABSTRACT Microfluidic geometries allow direct observation of microscale phenomena while conserving liquid volumes. They also enable modeling of experimental data using simplified transport equations and static force balances. This is possible because the length scales of these geometries ensure low Re conditions approaching the Stokesian limit, where the fluid flow profile is laminar, viscous forces are dominant and inertial forces are negligible. This work presents results on two transport problems in microfluidic geometries. The first examines heterogeneous binding kinetics in a microbead array, where beads with different chemical functionalities are sequentially captured in a					
15. SUBJECT TERMS microtextured surfaces, microfluidics, high throughput screening, hydrodynamic slip					
16. SECURITY CLASSIFICATION OF:		17. LIMITATION OF ABSTRACT		15. NUMBER OF PAGES	19a. NAME OF RESPONSIBLE PERSON
a. REPORT UU	b. ABSTRACT UU	c. THIS PAGE UU	UU		Charles Maldarelli
					19b. TELEPHONE NUMBER 212-650-8160

Report Title

Hydrodynamic and Mass Transport Properties of Microfluidic Geometries

ABSTRACT

Microfluidic geometries allow direct observation of microscale phenomena while conserving liquid volumes. They also enable modeling of experimental data using simplified transport equations and static force balances. This is possible because the length scales of these geometries ensure low Re conditions approaching the Stokesian limit, where the fluid flow profile is laminar, viscous forces are dominant and inertial forces are negligible. This work presents results on two transport problems in microfluidic geometries. The first examines heterogeneous binding kinetics in a microbead array, where beads with different chemical functionalities are sequentially captured in a well geometry over which analyte solution is flowed. Finite element simulations identified the flow rates and microbead surface receptor densities at which the binding rate approaches the kinetic limit, validating the results for the prototype NeutrAvidin biotin assay. The second part of this work discusses the dielectrophoretic motion of surfactant stabilized water droplet pairs in a microchannel as they approach and coalesce under a uniform electric field. Experimental data measuring droplet-droplet separation distance versus time were fitted to a model using the quasistatic force balance between the attractive electrostatic force and the resistive hydrodynamic force with a single adjustable parameter representing the drag force coefficient between each droplet and the adjacent microchannel walls. For glass microchannels, the drag force coefficient generates no slip. However, PDMS microchannels have significantly lower coefficient values corresponding to hydrodynamic slip lengths of 1-2 microns. These large slip lengths demonstrate that nanoporosity plays an important role in the hydrodynamics of PDMS microchannels.

Hydrodynamic and Mass Transport Properties of Microfluidic Geometries



Thomas F. Leary

Department of Chemical Engineering

The City College of City University of New York

A thesis submitted for the degree of

Doctor of Philosophy

December 2013

-
1. Reviewer: Professor Morton Denn

 2. Reviewer: Professor Alexander Couzis

 3. Reviewer: Professor Ilona Kretzschmar

 4. Reviewer: Professor Peter Ganatos

 5. Reviewer: Dr. Mohsen Yeganeh

 6. Reviewer: Professor Charles Maldarelli (Advisor)

Thesis Defense Date: December 16, 2013

Signature from Head of PhD Committee:

Abstract

Microfluidic geometries allow direct observation of microscale phenomena while conserving liquid volumes. They also enable modeling of experimental data using simplified transport equations and static force balances. This is possible because the length scales of these geometries ensure low Re conditions approaching the Stokesian limit, where the fluid flow profile is laminar, viscous forces are dominant and inertial forces are negligible. This work presents results on two transport problems in microfluidic geometries. The first examines heterogeneous binding kinetics in a microbead array, where beads with different chemical functionalities are sequentially captured in a well geometry over which analyte solution is flowed. Finite element simulations identified the flow rates and microbead surface receptor densities at which the binding rate approaches the kinetic limit, validating the results for the prototype NeutrAvidin-biotin assay. The second part of this work discusses the dielectrophoretic motion of surfactant-stabilized water droplet pairs in a microchannel as they approach and coalesce under a uniform electric field. Experimental data measuring droplet-droplet separation distance versus time were fitted to a model using the quasi-static force balance between the attractive electrostatic force and the resistive hydrodynamic force with

a single adjustable parameter representing the drag force coefficient between each droplet and the adjacent microchannel walls. For glass microchannels, the drag force coefficient values demonstrate no-slip. However, PDMS microchannels have significantly lower coefficient values corresponding to hydrodynamic slip lengths of 1-2 μm . These large slip lengths demonstrate that nanoporosity plays an important role in the hydrodynamics of PDMS microchannels.

To my beloved parents, Brian and Thana, whose enduring patience
and love have made this contribution possible.

Acknowledgements

This work was funded by the Army Research Office. Agreement
W911NF1110161

The Internship Opportunity at ExxonMobil Research and Engineering
Company in Clinton, NJ is gratefully acknowledged

Contents

List of Figures	v
1 Introduction	1
1.1 Background	1
1.2 Scope of Research	7
2 Mass Transfer Study of a Prototype Bioassay in a Spatially-Indexed Microbead Well Array	13
2.1 Background	13
2.2 Transport Simulations	24
2.3 Experimental Setup	35
2.3.1 Device design	35
2.3.2 Device fabrication	36
2.3.3 Microbead functionalization	37
2.3.4 Microbead capture and Spatial Indexing Without Encoding	38
2.3.5 Prototype assay	40
2.4 Conclusions	40
3 Hydrodynamic Slip at an Oil/Polydimethylsiloxane Surface From Measurements of the Dielectrophoretic Motion of Water Droplets	47
3.1 Background	47

CONTENTS

4	Electrocoalescence of Water-in-Crude Oil Emulsions in Two Dimensions	61
4.1	Background	61
4.2	Experimental Setup	64
4.3	Droplet Force Calculation	66
5	Future Work	73
5.1	Background	74
5.2	Proposed Research	76
5.3	Preliminary Results	81
	Appendix A	83
	Appendix B	93
B.1	Materials	93
B.1.1	Aqueous Phase	93
B.1.2	Microfluidic Cell Fabrication	94
B.2	Force Expressions	95
B.2.1	Interpolation Formula for the Electrostatic Force Between Conducting Spheres as a Function of Sphere-Sphere Sepa- ration Distance	95
B.2.2	Analytical Solution for the Hydrodynamic Drag Force Due to Approaching Spheres as a Function of Sphere-Sphere Separation Distance in an Infinite Medium, $\mathcal{R}(s/a)$	95
B.2.3	Hydrodynamic Drag Force on a Single Sphere Translating Between and Parallel to Two Parallel Walls	97
	References	99

List of Figures

2.1	Idealized schematic of the assembly of a microbead array by the gravitational settling of microbeads into wells incorporated as the bottom of a broad channel of rectangular cross section in a microfluidic cell.	19
2.2	(a) Velocity in the \tilde{y} direction (normalized by the average velocity U) as a function of \tilde{z} , in the plane $\tilde{x} = 0$, at the center of the well ($\tilde{y} = 0$) and at an upstream location inside the well and between the bead and the well wall ($\tilde{y}=28/80$) in the presence and absence of a microbead. (b) Magnitude of the velocity in the plane $\tilde{x} = 0$ inside the well in the absence and presence of a microbead. All simulations are for $\mathfrak{Re}=1$	41

LIST OF FIGURES

- 2.3 Target binding to probes on a circular patch on a microchannel wall and on the surface of a microbead in the well for $Pe = 10$: (a) The average nondimensional surface concentration on a surface patch and the surface of the microbead, $\bar{\Gamma}$, as a function of τ for $Da = 10, 10^2$ and 10^3 . (b)-(c) Target concentration boundary layers around, and the spatial distribution along either a surface patch (b), or the microbead in the well (c) for $\tau = 1, 15$ and 30 and $Da = 10$. For the microbead, the concentration boundary layer is in the plane $\tilde{x}=0$, and the surface concentration is the projection of the concentration on the hemisphere $\tilde{x} > 0$. $\varepsilon = .016$ and $k \rightarrow \infty$. Simulations at additional Pe and Da values are presented in Appendix A. 42
- 2.4 Target binding to probes on a circular patch on a microchannel wall and on the surface of a microbead in the well for $Pe = 10^4$: (a) The average nondimensional surface concentration on a surface patch and the surface of the microbead, $\bar{\Gamma}$, as a function of τ for $Da = 10, 10^2$ and 10^3 . (b) Target concentration boundary layers around, and the spatial distribution along, either a surface patch (b) or the microbead in the well (c) for $\tau = 1, 5$ and 10 and $Da = 10$. For the microbead, the concentration boundary layer is in the plane $\tilde{x}=0$, and the surface concentration is the projection of the concentration on the hemisphere $\tilde{x} > 0$. $\varepsilon = .016$ and $k \rightarrow \infty$ 43
- 2.5 Bright field and fluorescence images of sequential bead array in two fields of view. 44

LIST OF FIGURES

2.6	Normalized binding curves for prototype NeutrAvidin-biotin assay compared to finite element simulation results at equal Pe . $C_\infty = 4.2 \times 10^{-9}M$	45
3.1	Measurement of microchannel slip at an oil/PDMS surface by observing the dielectrophoretic merging of water droplets in oil moving in close proximity to the PDMS channel wall.	49
3.2	Dielectrophoretic merging of $40 \mu\text{m}$ radius droplets at the oil/PDMS surface: Frame captures of the pairwise merging at time intervals of .12 sec, flow direction from bottom to top and time (t) as function of the measured edge-to-edge scaled separation s/a from the images. The continuous line is a fit for a value for the droplet-wall drag coefficient, α	53
3.3	The drag coefficient f_m as a function of s/a for no-slip ($\lambda = 0$) and $\lambda = 1 \mu\text{m}$ for $d = 1 \mu\text{m}$ (top) and $d = 100 \text{ nm}$ (bottom) for $h = 100 \mu\text{m}$ and $a = 40 \mu\text{m}$	56
3.4	Hydrodynamic drag coefficient α as a function of separation d/a for droplets of radius $37.5 \mu\text{m}$ (a) and $40 \mu\text{m}$ (b) for fixed height $h=100 \mu\text{m}$. Symbols with error bars are the experimentally fitted coefficients, the remaining symbols are from numerical simulation (the accompanying dotted lines are a guide), and the no-slip line is from the Feuillebois et al (1) correlation.	58
4.1	Schematic of PDMS microchannel geometry used in experiments.	64
4.2	Time sequence of electrocoalescence in water-in-crude oil emulsion.	65

LIST OF FIGURES

4.3	Two dimensional configuration of water droplets in crude oil with COMSOL model.	67
4.4	Plot of electrostatic forces between droplet pairs versus normalized separation distance.	70
5.1	Schematic of interfacial rheometer using oscillating electric field. .	77
5.2	COMSOL calculation of droplet in oil subject to uniform electric field ($\epsilon_{Oil} = 2.5$, $E = 500$ V/mm, $a = 1.5$ mm). (a) $\sigma = 30$ mN/m. (b) $\sigma = 15$ mN/m. Spherical droplets deform due to the applied field to reach a non-spherical equilibrium shape. Note the longer time required for the lower tension interface to reach equilibrium.	82
A.1	Normalized binding curves showing effect of Pe at $Da = 1$	83
A.2	Normalized binding curves showing effect of Pe at $Da = 10$. . .	84
A.3	Normalized binding curves showing effect of Pe at $Da = 100$. . .	84
A.4	Normalized binding curves showing effect of Da at $Pe = 10000$. .	85
A.5	Normalized binding curves showing effect of Da at $Pe = 1000$. .	85
A.6	Normalized binding curves showing effect of Da at $Pe = 10$. . .	86
A.7	Cross-section of concentration profile in microchannel for patch surface at $x = 0$, $Pe = 100$, $Da = 1$	86
A.8	Cross-section of concentration profile in microchannel for bead surface at $x = 0$, $Pe = 100$, $Da = 1$	87
A.9	Cross-section of concentration profile in microchannel for patch surface at $x = 0$, $Pe = 100$, $Da = 10$	87
A.10	Cross-section of concentration profile in microchannel for bead surface at $x = 0$, $Pe = 100$, $Da = 10$	87

LIST OF FIGURES

A.11	Cross-section of concentration profile in microchannel for patch surface at $x = 0$, $Pe = 100$, $Da = 100$	88
A.12	Cross-section of concentration profile in microchannel for bead surface at $x = 0$, $Pe = 100$, $Da = 100$	88
A.13	Cross-section of concentration profile in microchannel for patch surface at $x = 0$, $Pe = 1000$, $Da = 1$	88
A.14	Cross-section of concentration profile in microchannel for bead surface at $x = 0$, $Pe = 1000$, $Da = 1$	89
A.15	Cross-section of concentration profile in microchannel for patch surface at $x = 0$, $Pe = 1000$, $Da = 10$	89
A.16	Cross-section of concentration profile in microchannel for patch surface at $x = 0$, $Pe = 1000$, $Da = 10$	89
A.17	Cross-section of concentration profile in microchannel for bead surface at $x = 0$, $Pe = 1000$, $Da = 10$	90
A.18	Cross-section of concentration profile in microchannel for patch surface at $x = 0$, $Pe = 1000$, $Da = 100$	90
A.19	Time sequence of fluorescent micrographs measuring binding of NeutrAvidin-Texas Red ($C = 4.16 \text{ E } -9 \text{ M}$) to biotin-functionalized glass microbeads ($\Gamma = 5.5 \text{ E } -9 \text{ M}$) at $Pe = 5600$	91
B.1	Viscosity of mineral oil as a function of temperature.	94
B.2	Normalized electrostatic force as a function of normalized separation distance as given by the exact bispherical calculation and the interpolating equation.	96

LIST OF FIGURES

- B.3 Hydrodynamic drag force on a single sphere translating between two parallel walls for no slip, $\lambda = 0 \mu\text{m}$ as a function of the sphere/wall separation distance d (edge-to-edge), comparing the Feuillebois correlation and our COMSOL calculation for two values of the channel height h relative to the sphere radius a 97

1

Introduction

1.1 Background

One of the main themes in the evolution of scientific research has been miniaturization. From early advances in optics that allowed direct observation of microscopic entities such as cells to the continued progress in semiconductor fabrication that enables increasingly fast (and increasingly portable) electronics, technological innovation is often synonymous with the ideas of making and observing on a progressively smaller scale. The ramifications of this miniaturization are manifold, but can almost always find application at much larger scales. Investigation of individual cells provides insight into the biology of living organisms, manufacture of microscale electronics enables communication over many kilometers, and the synthesis and characterization of nanoparticles improve the properties of bulk materials. Fabrication and observation of microscopic phenomena are invaluable tools, but in many instances the two are not performed simultaneously, precluding the opportunity of manipulating the microscopic entities in real time and consequently limiting the applicability of such experiments to macroscale dynamic processes. To make a microscale observation as valid as possible at the

1. INTRODUCTION

macroscale, it should be a direct miniaturization of the macroscale system, including all of its components and capturing all of its dynamics.

Such a miniaturized system can be called a lab-on-a-chip (LoC), implementing a macroscale process in a microscopically observable environment and exploiting the advantages of its small length scale to reduce the time and increase the precision of the process. The LoC concept was first introduced by the use of microelectromechanical system (MEMS) components in electronics. These components, such as actuators, gyroscopes and piezoelectric elements, are fabricated using the same photolithography techniques pioneered by the semiconductor industry to manufacture computer processors and circuitboards. Although integration of such components into a single chip has become ubiquitous in electronics, the LoC concept has been popularized by the use of photolithographically patterned materials to act as templates for fluid flow geometries.

Photolithography, the patterning of a substrate using light, has evolved substantially since its origins several decades ago, but the two principal components critical to its success as a pattern transfer technique have always been optics and materials. The optical path, and the wavelength of the light used, have a dramatic impact on the maximum achievable fidelity and resolution. To achieve feature sizes on the order of nanometers, currently the resolution limit for semiconductor fabrication, a light source with a comparable wavelength, such as an electron beam, or a high intensity discharge lamp (KrF or ArF) coupled with an optical stepper must be used. The tremendous cost of this equipment limits the availability of such capabilities to a small number of institutions. However, micrometer resolutions can be achieved by UV exposure sources without the need for an optical stepper or other expensive equipment. This resolution limit may

be inadequate for applications where the patterned feature density demands the highest possible resolution, such as microprocessors or MEMS, but is acceptable for the fabrication of fluidic channels, particularly when coupled with the comparable resolution of bright field and fluorescent microscopy methods commonly used to observe such systems.

The materials selected for the fabrication of MEMS and semiconductor components are dictated by precise consideration of their physical properties. In contrast, the materials used to construct fluidic channels are in most applications not critical to the process, provided they are chemically inert to the fluid(s) with which they come in contact, and are therefore selected primarily by considerations of cost and ease of fabrication. To fabricate fluidic geometries from glass or crystalline materials, an ablative technique such as etching is required. A number of etching methods exist, but they are either expensive (reactive ion etching) or time-consuming and dangerous (HF) to the point that they are of limited utility in the fabrication of devices that may only be used once. For this reason, photolithographic fabrication of fluid channels was not common until the late 1990s, when polymeric materials were used in the development of simple, inexpensive fabrication techniques known as soft lithography.

Soft lithography was pioneered by George Whitesides in the late 1990s ((2)) and it dramatically reduced the cost and difficulty of fabricating fluidic channels. Rather than use the patterned photoresist film as a protective layer to prevent regions of the underlying substrate from being etched or coated, soft lithography uses the developed film as a mold over which liquid monomer is poured and polymerized. The resulting solid is then simply peeled off the mold, taking advantage of the polymer's large elasticity (and, if necessary, chemical release agents applied

1. INTRODUCTION

to the photoresist surface prior to the application of the polymer). The photoresist film, typically consisting of a crosslinked epoxy, is extremely durable and can be repeatedly reused. Soft lithography therefore enables researchers to rapidly fabricate large numbers of devices from a single patterned photoresist mold at ambient conditions.

The most commonly used polymer in soft lithography is polydimethylsiloxane (PDMS). The chemistry of the dimethylsiloxane enables it to be oxidized to form silanol groups, which can react with other silanol groups in the presence of trace amounts of water to form siloxane bonds. This silane chemistry, and its elasticity, enable PDMS to be covalently bonded to itself, as well as to glass and silicon, simply by bringing the surfaces into conformal contact subsequent to oxidation via exposure to oxygen plasma. Cutting access ports into opposite ends of the PDMS layer prior to bonding allows fluid to be pumped into the fluidic channel. The transparency of the PDMS to optical light allows direct observation via brightfield microscopy, and the low fabrication cost allows the devices to be discarded after a single use.

Fluid-based LoCs have the same advantage as MEMS in terms of integrating multiple components (or simply multiple channels). Additionally, the small dimensions of the device require only a microliter scale volume, facilitating the conservation of potentially expensive analytes. However, the single most important advantage of these fluid-based LoCs is the ability to exploit the inherent properties of transport phenomena on small length scales to rapidly reproduce experimental conditions that are easily characterized and measured. The study of these phenomena in such devices is known as microfluidics.

The most fundamental transport process occurring in the microfluidic channel

is the fluid flow. The ability to precisely control this flow and characterize its hydrodynamics is central to accurate microfluidic experimentation. Fortunately, this is easily achieved because the small length scale ensures microchannel flows are well within the laminar flow regime. Consequently, fluid streamlines in the channel do not cross, but rather different fluid layers flow smoothly past one another in the classic conceptual sense. This allows the generation of stable, smooth interfaces between different fluids flowing in the same channel, miscible or immiscible. It also has important consequences with respect to mass transfer, because it makes mixing in microchannels extremely difficult. Not only are microchannel flows laminar, many approach the Stokesian limit, in which inertia is zero. This phenomenon allows the researcher to actuate the fluid flow with a precision not possible in macroscale flows like a faucet or a river by simply equilibrating inlet and outlet pressures across the microchannel to instantaneously stop the flow (in practice this is difficult due to limits in instrumentation). In theory, inertia is always present and the fluid must decelerate to stop, but the time scale for the deceleration is vanishingly small. No strict definition exists for the Reynolds number below which inertia can be neglected, but this assumption greatly simplifies the hydrodynamics of particles translating (and rotating) in the microchannel.

Neglecting inertia simplifies microchannel hydrodynamics to the Stokes equation, but analytical solutions can still be difficult to obtain due to the microchannel geometry. This is partially due to the binary nature of a single photoresist patterning step, resulting in a geometry that requires a two-dimensional solution. Such a solution exists for the simple case of an open rectangular duct channel, which simplifies to the well-known one dimensional solution when the aspect ra-

1. INTRODUCTION

tio of the duct cross-section is sufficiently large. Many microchannels, however, contain contractions, expansions, obstacles and other geometries that complicate the hydrodynamics. These cases require a numerical solution using finite element or another computational method. Once the solution for the fluid velocity profile has been obtained, it can be used to model heat and mass transport.

Microfluidics has found application in many areas, but is most commonly associated with biological research. Numerous reasons for this exist. A low cost, single use, biologically inert platform that is readily mounted for observation using a bright field or confocal microscope and has theoretical volume requirement in the microliters, microchannels have been used to incubate living cells, perform DNA conjugation and amplification, and perform bioassays. An entire literature has developed in the course of less than two decades describing different ways to exploit the novelty of microfluidic transport properties to enhance biological research. While many of the techniques presented in a biological context could in theory be applied to other areas, material compatibility between polymeric microchannels such as PDMS and many liquids is less than ideal. Specifically, strong solvents such as toluene and chloroform interact strongly with the PDMS material. However, as discussed earlier, fabrication of microfluidic devices from glass or crystalline materials is possible, and can be used to study chemical reactions and separations in microfluidic geometries; such microreactors are the focus of many studies.

Microchannels produced by soft lithography may be susceptible to solvents, but they can still be used with some non-polar liquids, specifically higher viscosity oils. These oils are inert and therefore of limited interest by themselves. However, their use as a carrier fluid for a dispersed phase is now a common area of research.

The dispersed phase could be a suspension of solid particles, and numerous studies of the hydrodynamics of such systems exist. More commonly, these oils serve as carrier fluids for liquid droplets which are generated in the microchannel by intersecting microchannel flows of the dispersed phase and the carrier fluid (continuous phase). This technique, called flow focusing, capitalizes on the laminar flow regime in the microchannel to form highly monodisperse droplets. Typically, surfactant is required at the liquid-liquid (or in some studies, liquid-gas) interface to sufficiently lower the surface tension to allow droplet formation. This interface is not the focus of study in many applications, and the droplets themselves are simply carriers for an analyte (or cell). However, the importance of interfacial dynamics in scientific fields from the clinical to the industrial makes research focusing on the droplet interface extremely interesting. In particular, investigations of droplet coalescence to predict emulsion stability and droplet wetting on solid surfaces to engineer self-cleaning surfaces have wide application and have attracted considerable attention in microfluidics. This is because the aforementioned advantages of microfluidics naturally lend themselves to the observation, manipulation and measurement of dynamic processes occurring at fluid-solid and fluid-fluid interfaces.

1.2 Scope of Research

This study will demonstrate the ability of microfluidic devices fabricated using simple soft lithography techniques to act as platforms for the quantitative study of interfacial dynamics in two applications. The first is a heterogeneous kinetics study of protein screening assays. This study employed a microfluidic geometry

1. INTRODUCTION

to fluidically capture and retain an array of functionalized glass microbeads to serve as substrates for a prototype heterogeneous bioassay. It demonstrated the ability to capture and retain beads at addressable locations in an array of microwells patterned into bottom wall of a PDMS microchannel. This retention not only allows observation of the microbead surfaces during the bioassay, but enables the deposition of multiple bead sets in sequence. By recording the locations of beads from each set as they are successively deposited in the well array, an addressable registry of bead surface functionality can be created. This eliminates the requirement to identify the microbeads using optical barcodes. Once completed, the microbead array is exposed to an aqueous solution of analyte that is flowed through the channel. The analyte binds to the probe molecule displayed on the microbead surfaces according to classic Langmuir kinetics, and the rate of binding is determined by measuring the change in fluorescent signal on the bead surfaces over time using a fluorescent microscope. The use of large n arrays of different bead functionalities effectively performs precise measurements of multiple assays simultaneously using a single analyte sample, a technique known as multiplexing.

To interrogate potential ligand-receptor pairings by observing which microbead surface functionalities the analyte molecule binds to, or to test a sample for the presence of a particular analyte using beads with a known conjugate receptor, precise measurement of the binding rate is not critical. Rather, a limit of detection in terms of the fluorescence intensity on the bead surface must be exceeded to identify a positive analyte-surface conjugation. However, the ability to measure binding rate data theoretically enables the calculation of the kinetic constant for the reaction. In the kinetic limit, the analyte concentration is constant and the surface concentration of the bound analyte as a function of time can be easily

calculated. However, real experimental conditions can only approach this limit, and if the rate of reaction at the surface is greater than the rate of diffusion to the surface, depletion of the analyte species from solution will occur. The result is a surface reaction in which the analyte concentration in the fluid layer at the microbead surface is less than in the bulk fluid, and fitting such data to calculate the kinetic constant by assuming the kinetic limit is valid would produce incorrect values. Instead, numerical simulations can be used to solve the fluid velocity field around the microbead and its retaining well. This time-independent velocity field can then be coupled to the unsteady state convective-diffusion equation to solve the mass transfer problem. By solving the concentration profile in the microfluidic geometry, the surface concentration of the bound analyte can be calculated as a function of time and the result compared to the kinetic limit. By varying the flow rate of the incoming analyte solution, as well as the reaction rate at the microbead surface, experimental conditions at which the binding is kinetically limited can be identified. These results are validated for the well-known avidin-biotin conjugation using glass microbeads conjugated with biotin to assay a solution containing a known concentration of NeutrAvidin (a proprietary form of the protein avidin) that has been fluorescently labeled with Texas Red dye. Performing the same assay at different flow rates allows measurement of the fluorescent signal on the microbead surfaces in each experiment to be compared to the simulation results.

The second part of this work is a hydrodynamics study of droplet electrocoalescence. PDMS microchannels containing a flow focusing orifice are used to generate monodisperse, surfactant-stabilized water droplets in mineral oil. The flow rates of the two fluids through the orifice determine the droplet spacing,

1. INTRODUCTION

which is adjusted so that the droplets are propelled through the channel in a single file train with each droplet separated from adjacent droplets by distances of several droplet radii. The application of a high-strength, uniform electric field polarizes the conducting water droplets in the insulating mineral oil, and when the droplet train is aligned parallel to the direction of the applied field, adjacent droplets experience an attractive dielectrophoretic force. If the separation distances between all droplets in the train are equal, then the attractive forces cancel and the droplets experience no net motion relative to one another (neglecting consideration of the first and last droplets in the train). However, perturbations of the fluid flow and changes in orientation of the droplet train relative to the field as the droplets translate through different sections of the microchannel result in droplets pairing off and dielectrophoretically moving towards one another.

The relative motion of the two droplets as they approach and coalesce can be decoupled from the translational motion of the droplets through the microchannel due to the pressure-driven flow of the mineral oil, a consequence of the Stokesian limit near which the hydrodynamics occur. The trajectory of the droplets is therefore determined by a simple force balance between the attractive electrostatic force and the resistive hydrodynamic drag force. Both are functions of the droplet-droplet separation distance, which can be precisely measured as a function of time using a high-speed camera. The hydrodynamic drag force is also a function of the droplet velocity, which is the time derivative of the separation distance. Integration of this form of the force balance produces a model expression for the droplet-droplet separation distance as a function of time that can be fitted to the experimental data. If the hydrodynamic drag force on the droplet is only a function of the droplet-droplet separation distance, the model has no adjustable

parameters. This would be true for two spheres approaching in a liquid with no additional surfaces, provided the boundary condition at the sphere surface is known. The surfactant immobilization of the oil-water interface produces a no-slip boundary condition, so the droplets can be treated as hard spheres and the droplet-droplet hydrodynamics are fully defined. However, the droplets in the microchannel have diameters on the order of the channel height, and the larger density of water relative to the mineral oil creates a negative buoyancy resulting in droplet-wall separation distances of less than $1\ \mu\text{m}$. This introduces an additional component to the hydrodynamic drag force on the droplet, one that is a function of a separation distance that cannot be directly measured in this experiment. This force is therefore introduced as a fitting parameter in the integrated force balance.

In addition to being dependent on the boundary condition at the droplet surface, the droplet-wall hydrodynamic drag force is a function of the boundary condition at the microchannel surface. The standard no-slip assumption again results in a well-defined problem, with the fitted value of the force then used to directly calculate the droplet-wall separation distance. An independent estimation of the droplet-wall separation distance can be made by calculating the trajectory of the negatively buoyant droplets based on their known translational velocity and assumed initial position in the center of the channel upon formation. This distance can be compared to the data fitted value to validate the no-slip boundary condition at the microchannel surface. If the surface is glass, the no-slip assumption is valid. However, PDMS microchannels are shown to have droplet-wall drag force values that are significantly lower than expected for a no-slip wall. This is because PDMS is not an ideal solid, but rather a nanoporous matrix due to its

1. INTRODUCTION

air solubility. Nanopores on the microchannel surface that are open to the fluid flow enable finite fluid velocities at the surface. These velocities are defined as the product of the velocity gradient at the surface and a slip length determined by the chemical and physical properties of the surface in the classical definition of hydrodynamic slip. Slip lengths are usually neglected for fluid flows over smooth solid surfaces because their magnitude is on the order of nanometers and such distances are negligible relative to continuum flow dimensions. However, porous surfaces can have much larger slip lengths due to the ability of small pores to retain air and not be wetted by the mineral oil from the microchannel. The surface therefore maintains a Cassie-Baxter state that is only partially wetted and the slip length is a function of the ratio of the viscosities of the two phases. This work reports measurements of slip lengths of both hydrophobically functionalized glass and native PDMS surfaces. As expected, the glass surface has a slip length of zero to the precision of the measurement, while the PDMS surfaces demonstrate slip lengths of 1-2 μm consistent with a Cassie-Baxter state.

2

Mass Transfer Study of a Prototype Bioassay in a Spatially-Indexed Microbead Well Array

2.1 Background

The field of microfluidics has received more attention from research with biological applications than from perhaps any other area. The rapid, low-cost fabrication of biologically inert polymeric devices has enabled researchers to fabricate LoCs that perform reactions, separations and detection assays while conserving valuable analyte. The optical transparency of these devices has allowed for unprecedented observation of these processes in situ, in many cases permitting quantification of individual biological entities such as cells, DNA or proteins.

One of the most important areas of research involving biological species is the screening of the binding interactions of proteins. Proteins control biological activity by selectively binding to target species including other proteins, peptides,

2. MASS TRANSFER STUDY OF A PROTOTYPE BIOASSAY IN A SPATIALLY-INDEXED MICROBEAD WELL ARRAY

nucleic acids and small molecules. The high specificity of these binding interactions results in thousands of different proteins performing unique functions to form a complex network that can be mapped to give greater insight into biology at the cellular, tissue and organism levels. This mapping of protein functions, known as proteomics, allows researchers to build a library that can be used to rapidly detect abnormal or diseased states. Protein screening is also used in the development and validation of pharmaceuticals for targeted drug delivery. This field is responsible for testing candidate drug molecules against potential receptor proteins to analyze and quantify the specificity of the candidate drug in selectively binding to particular protein receptors to achieve a desired biological effect and reduce or eliminate harmful side effects. Protein receptors also play a vital role in the intake of toxins and disease vectors to tissues and cells, and therefore screening assays are crucial to clinical diagnostic identification of disease markers as well as pathogen detection in applications including environmental surveillance and food monitoring.

Due to the large number of potential receptors in any biological system, effective protein screening protocols require thousands of ligand-receptor pairings to be interrogated. Current high-throughput procedures for performing these tests typically employ one of two approaches: microarrays or bead arrays.

The most traditional methodology for bioassays is the 96-well plate enzyme-linked immunosorbent assay (ELISA) (3, 4, 5). This platform (also termed microtiter plates) was developed in the 1970s and is still commonly used. In this approach, a plate (typically polystyrene) is used as a substrate to attach capture antibodies to the surfaces of the wells arranged in a rectangular matrix. An analyte sample is dispensed into each of the wells, and the capture antibodies

then selectively bind with antigens present in the sample to tether them to the substrate. The amount of antigen present is quantified by a second detection antibody coupled to some type of detectable entity, such as a fluorophore, which can be quantified by optical microscopy. To enhance the capability of this platform, researchers have miniaturized the wells, resulting in 384, 1536 and even 9600 well plates using etched glass or silicon substrates (6). While this method can be used for the detection of one or several analytes in many bioassays, the limitation of a single antibody per well makes conventional well plates poorly suited for multiplexed assays. Recent research has focused on approaches to circumvent this limitation by using robotic spotting or lithographic patterning to produce microarrays of different antibodies on a single chip.

Microarrays offer significant improvements over well plate assays (6, 7, 8, 9, 10, 11, 12, 13, 14, 15, 16, 17, 18, 19). By presenting multiple antibodies to a single analyte sample, they effectively reduce the required sample volume and decrease throughput time. Early work demonstrated this concept by simply arraying multiple receptors in each well plate to create a high-throughput ELISA (20). More recently, high-density planar chips have been created using modified inkjet printer heads and pins. While inkjet heads and pins can locally deposit protein solutions to create arrays on the order of microns, the smallest dispensable liquid droplets limit printable array resolution. Lithographic techniques have been employed to increase array densities even further. Martin et. al. employed a microcontact printing approach, using an elastomer stamp patterned using soft lithography to introduce antibody proteins onto an aminosilane-functionalized glass surface (21). Other researchers have used dip-pen lithography to both pattern surfaces for subsequent deposition of proteins and deposit proteins directly on surfaces

2. MASS TRANSFER STUDY OF A PROTOTYPE BIOASSAY IN A SPATIALLY-INDEXED MICROBEAD WELL ARRAY

(22, 23).

In spite of the obvious advantages of microarrays, they suffer from the same drawbacks inherent to 2-D platforms such as well plates. These devices often produce low signal-to-noise ratios due to non-specific adsorption of both capture antibody and antigen on the surface, although passivation of the background with polyethylene glycol can remedy this issue. Microarrays have lower analyte sample volume requirements than well plates, but significant volume may still be required to immerse the substrate in the analyte solution. More importantly, the incubation times required for assays on planar substrates are long due to the heterogeneous reaction kinetics. Finally, although microarrays theoretically offer a platform for rapid screening of many antibodies, the large array densities make indexing the identities of hundreds or thousands of potentially unique antibodies extremely difficult. An alternative approach in which multiple antibodies can be efficiently indexed for a high-throughput, multiplexed assay is therefore desirable.

Bead-based assays have several advantages over 2-D planar assays. By using the surfaces of small particles in the micron size range as the platform for tethering of the target antigens, the high surface-to-volume ratios of the particles can be exploited, allowing for nearly solution phase kinetics to reduce incubation times and reducing the required sample volume. Sets of beads can be spectrally encoded to identify a particular receptor on the surface of each bead set, allowing for multiple bead sets to be incubated together with an analyte solution to produce a multiplexed assay. To identify the receptor on the surface of a particular bead and determine to which antigen it has conjugated, the bead suspension is flowed through a narrow channel wherein the spectral labels of individual beads are sequentially excited by a series of lasers and the emission spectra recorded

and deconvoluted. This technique is known as flow cytometry.

Flow cytometry is a commercially available technology that has been successfully employed to perform a number of bioassays. In many instances, it has demonstrated superior accuracy and sensitivity compared to conventional plate-based protocols. Early experiments utilized polystyrene microbeads labeled with a single fluorophore to perform assays. Stewart and Steinkamp demonstrated that such a system could be used as a standard to count cells in blood samples (24). Later work has interrogated the interactions between antibodies and immunoglobulin, hepatitis C and phospholipids (25, 26, 27).

The main advantage of flow cytometry is its multiplexing ability (28). While early research did not exploit this capability, the demand to simultaneously interrogate multiple analytes will become more critical as genomics and proteomics research identify more potential targets for study. Currently, commercially available platforms such as Luminex xMAP can provide up to 500 spectrally encoded bead sets for multiplexed assays (29). These systems have seen widespread use over the past decade, and recent research has demonstrated the potential to increase the number of unique labels, or barcodes, still further while improving upon the method of labeling (30).

However, the labeling of bead sets in flow cytometry experiments can be expensive and cumbersome. Although commercial platforms are available, they typically consist of polystyrene beads labeled with fluorescent molecules. Polystyrene beads may be poorly suited for specific applications, and fluorescent molecules undergo photobleaching over time. For all flow cytometry experiments, calibration of each individual bead set is required; this takes time and can introduce significant error into the experiment. Eliminating the requirement for spectral

2. MASS TRANSFER STUDY OF A PROTOTYPE BIOASSAY IN A SPATIALLY-INDEXED MICROBEAD WELL ARRAY

labeling of bead sets would therefore dramatically improve the efficiency of bead-based bioassays.

As an alternative to spectral labeling, bead sets can be deposited onto a surface to create a spatially-indexed array. This approach combines the miniaturization of microarrays with the enhanced efficiency of bead-based assays. format which incorporates advantages of both the flat microarray and the flow cytometric/microbead array for parallel, high-throughput screening. (31, 32, 33, 34). To accomplish this, the beads must be captured and sequestered on a surface. In general, several methods exist to pattern immobilized microbeads on a flat substrate surface. Microbeads can be deposited by gravity from a solution placed above the surface, and then affixed to the surface by using electrostatic interactions (35, 36, 37, 38, 39), covalent bonding (40, 41), protein-ligand binding (42), an adhesive layer (43), or by transferring a pre-formed array of beads onto an adherent surface (44, 45). However, capturing beads by gravity-settling in an array of wells inscribed on a surface (a well-plate) presents a simpler solution because it does not rely on bead/surface interactions, and, by properly sizing the wells to be only slightly larger than the microbead diameter, single microbeads can be captured at the array (well) location, which simplifies the tracking and correlation of screening events. Walt and collaborators (46) first pioneered the trapping of beads with surface probes in wells for screening applications by etching wells into the tips of individual fibers of a fiber optic bundle to form a well-plate, an approach which also allowed for individual readouts of fluorescently labeled binding events. Incorporating a well-plate filled with beads into a microfluidic cell can be undertaken in either of two ways. As studied by Bau et al (47, 48, 49), beads are first trapped in the wells of a well-plate, and the plate is then incorpo-

2.1 Background

rated as the bottom of a microfluidic flow cell. Bau et demonstrate that the flow through the cell does not lift the beads out of the wells as long as the flow rate is below a critical value. Bau et al also demonstrated that this ex-situ method of bead assembly, because it allows unhindered access to the array during the insertion of the beads in the wells, can be used to position the beads in the wells by micromanipulation, so that an array can be assembled with beads displaying different probes with the probe identity at each array position known. Bau et al also showed that the wells can be loaded by random deposition from solution, and in this case, to display beads with different probes in the array, they encoded the beads. Instead of ex-situ assembly, microbeads can also be assembled directly

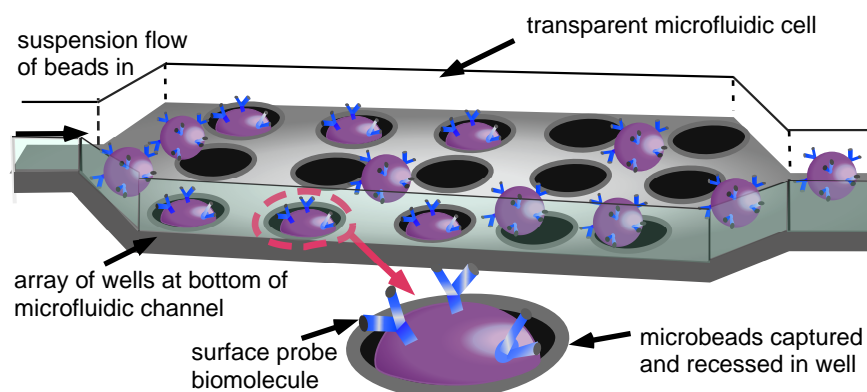


Figure 2.1: Idealized schematic of the assembly of a microbead array by the gravitational settling of microbeads into wells incorporated as the bottom of a broad channel of rectangular cross section in a microfluidic cell.

into an array in a microfluidic cell in one step by using an unfilled well-plate as the cell bottom and streaming a suspension of beads through the cell at a sufficiently low velocity to allow individual beads to be captured in the wells due to gravity or the application of an external field (see Fig. 2.1 and refs.(50, 51) who also demonstrated the use of the array for a binding assay). To maximize

2. MASS TRANSFER STUDY OF A PROTOTYPE BIOASSAY IN A SPATIALLY-INDEXED MICROBEAD WELL ARRAY

both the speed and the efficiency of the microbead capture in this format, electric and magnetic fields have been applied to charged or paramagnetic beads (respectively) to direct the beads into the wells (52, 53, 54). Fluid suction has also been used to assist in the bead capture; holes placed at the bottom of the wells provide a liquid path from the channel above the wells to drains (see McDevitt et al (55, 56, 57, 58, 59, 60, 61, 62, 63, 64) and Ketterson(65), and applying a pressure drop across these holes propels the beads into the wells. This capture approach also increases fluid flow around the beads and therefore improves mass transfer of analyte during the subsequent bioassay.

This study uses a microfluidic geometry in which the microbeads are introduced into the device in a fluid suspension and captured in recessed well array due to gravity (Fig. 2.1). Our objective is to study, both theoretically using numerical simulation and experimentally in a microfluidic flow cell with a prototype assay, the mass transfer in the binding of a protein from solution to ligand molecules displayed on the bead surface. The results of the analysis can be used to construct guidelines for incubation times or injection volumes and flow rates to ensure a particular level of binding for detection(66, 67, 68, 69), or to define kinetically controlled regimes in studies of the intrinsic binding kinetics of a receptor-ligand pairs.

In the standard biosensor geometry, a surface patch of capture probes (length ℓ and width t_s) is localized in a rectangular channel of width w and height h with $h \ll w$ and $t_s \approx w$. The convective flow of the target analyte, entering the flow cell with concentration c_o is driven by either a pressure gradient (which we will consider here) or electrokinetically by a electric potential gradient. For $h \ll w$ end effects are neglected and the flow can be considered unidirectional (in the y

2.1 Background

direction) and only a function of z , with average velocity U ; for pressure driven flow $v_y(z) = \frac{3U}{2} \left\{ 1 - 4 \left\{ \frac{z}{h} \right\}^2 \right\}$. The transport of the target molecule in solution to the channel wall consists of diffusion across the (parallel) convective flow streamlines, and kinetic binding of the target to the probe once the target has arrived to the sublayer of solution immediately adjoining the surface(68). With $h \ll t_s$, this mass transfer is principally two dimensional. The time scale for a target molecule to be convected along the patch is $t_c = \ell/U$, and the time scale for the target to diffuse across the channel is $t_D = h^2/\mathcal{D}$ where \mathcal{D} is the target diffusion coefficient. The ratio of these scales, $t_c/t_D = \frac{\ell/h}{Pe}$ defines a Peclet number ($Pe = Uh/\mathcal{D}$). Typically, $h \sim 10^2 \mu\text{m}$, $w \sim 10^3 \mu\text{m}$ and $U \sim 10^2 - 10^4 \mu\text{m}^2/\text{s}$ corresponding to flow rates $Q \sim 10^{-1} - 10^2 \mu\ell/\text{min}$. Target proteins or smaller biomolecular ligands have molecular weights of order $10^3 - 10^4$ and corresponding diffusion coefficients of $\sim 10^2 \mu\text{m}^2/\text{s}$ so that Pe is large, of order $10 - 10^4$. If, in addition to $Pe > 1$, the sensor patch ℓ is short enough such that $\ell/h < Pe$, then the time for diffusion across the channel is smaller than the time required for the target to move over the patch ($t_c < t_D$), and target can only reach the surface through a boundary layer with a thickness, which increases with distance down the channel but is always smaller than h with the target concentration outside of the boundary layer approximately equal to the inlet concentration c_o . For $Pe > 1$ and $\ell/h \ll Pe$, the boundary layer becomes asymptotically small in Pe everywhere along the patch, and the flow in the boundary layer is approximately linear in the direction normal to the surface ($v_y \approx 6(U/h)(z - h/2)$). The boundary layer thickness at the downstream end of the patch, δ , can be estimated as the thickness for which the time for diffusion across this thickness to the patch is equal to the time for a target molecule riding at a distance δ from the wall

2. MASS TRANSFER STUDY OF A PROTOTYPE BIOASSAY IN A SPATIALLY-INDEXED MICROBEAD WELL ARRAY

to reach the end of the patch, i.e. $\frac{\delta^2}{\mathcal{D}} \sim \frac{\ell}{\{U/h\}\delta}$ or $\frac{\delta}{h} \sim \left\{\frac{\ell/h}{Pe}\right\}^{1/3}$. When, for $Pe > 1$, the patch size is large enough such that $\ell/h \geq Pe$, then the diffusion times across the channel is of order or shorter than the average convective passage time along the patch at the far downstream end, and the boundary layer grows and reaches through the channel cross section, depleting the bulk concentration.

At the patch surface the diffusive flux is equal to the kinetic rate (per unit area) with which target binds to the surface probe. Kinetic binding is a bimolecular process of which the most elementary is the Langmuir kinetic scheme, $\frac{\partial \Gamma}{\partial t} = k_a c_s \{\Gamma_\infty - \Gamma\} - k_d \Gamma$ where Γ is the surface concentration of bound target and Γ_∞ is the maximum number of targets which can bind (per unit area), c_s is the sublayer concentration at the surface and k_a and k_d are the association and disassociation rate constants, respectively. The equilibrium surface density (Γ_{eq}) is $\frac{\Gamma_{eq}}{\Gamma_\infty} = \frac{k}{1+k}$ where $k = \frac{k_a c_o}{k_d}$. During the binding process, the sublayer concentration initially decreases due to kinetic binding, but at later times increases as the surface begins to saturate, causing the kinetic flux to decrease and the diffusive flux to repopulate the sublayer.

For $Pe > 1$ and $\ell/h \ll Pe$, the diffusive flux to the surface through the boundary layer scales as $\frac{D\{c_o - c_s\}}{\delta}$, where c_s is the sublayer concentration; equating this flux to the the maximum kinetic flux defines a scale for the sublayer concentration, $\frac{c_s}{c_o} \sim \frac{1}{1 + Da \left\{\frac{\ell/h}{Pe}\right\}^{1/3}}$, where the Damkohler number Da is defined as $Da = \frac{k_a \Gamma_\infty h}{\mathcal{D}}$. In the limit $Pe > 1$ and $\ell/h \ll Pe$, when $Da \left\{\frac{\ell/h}{Pe}\right\}^{1/3} \gg 1$ (fast binding kinetics relative to diffusion), the sublayer concentration tends to zero. This mass transfer controlled regime has been studied extensively as the entrance region problem (70, 71), with analytical expressions for Γ as a function

2.1 Background

of t and the distance along the sensor surface. As the target flux to the surface is controlled solely by the diffusive mass transfer, the characteristic time for the target to bind to an equilibrium surface density ($t_{eq,\mathcal{D}}$) is given by $t_{eq,\mathcal{D}} \frac{\mathcal{D}c_o}{\delta} \sim \Gamma_{eq}$ or $\tau_{eq,\mathcal{D}} = \frac{t_{eq,\mathcal{D}}}{h^2/\mathcal{D}} \sim \varepsilon \frac{k}{1+k} \left\{ \frac{\ell}{h} \right\} \{Pe\}^{-1/3}$ where $\varepsilon = \frac{c_o h}{\Gamma_\infty}$ and $\tau_{eq,\mathcal{D}}$ denotes a nondimensional completion time scaled by the diffusion time across the channel ($t_{\mathcal{D}}$). The parameter ε is the ratio of the channel height h to the adsorption depth Γ_∞/c_o , the distance above the surface which contains (per unit area) enough target to saturate the surface. For $\ell/h \geq Pe$, analytical solutions can also be obtained for $Da \rightarrow \infty$ for the fully-developed concentration profile(71). When, for $Pe > 1$ and $\ell/h \ll Pe$, $Da \left\{ \frac{\ell/h}{Pe} \right\}^{1/3} \ll 1$ the binding kinetics are slow relative to diffusion, and the sublayer concentration remains at the inlet concentration. (This is also true for arbitrary Pe and ℓ/h if $Da \rightarrow 0$.) The process is only controlled by the binding kinetics, and $\frac{\Gamma(\tau)}{\Gamma_{eq}} = 1 - e^{-\varepsilon Da(1+\frac{1}{k})\tau}$ where the characteristic kinetic time for equilibrium binding is $\tau_{eq,k} \sim \frac{1}{\varepsilon Da} \left\{ \frac{k}{1+k} \right\}$ and $\tau_{eq,k}$ is a nondimensional time scaled by the diffusion time $t_{\mathcal{D}}$ (see Goldstein et al who have extended this analytical solution for small Da (72, 73)). For intermediate values of Da and $Pe > 1$, analytical solutions can be obtained for $\Gamma/\Gamma_{eq} \ll 1$ (71, 74). When the surface concentration is not negligible, analytical solutions cannot be obtained because of the nonlinearity of the kinetic equation. For $Pe \gg 1$ and $\ell/h \ll Pe$ and Da of order one, boundary layer (two compartment) models in which the Langmuir kinetic equation and a relation equating the boundary layer flux to the net kinetic adsorption are integrated either numerically in time for the average surface concentration on the patch(75, 76, 77, 78, 79, 80, 81, 82, 83) or analytically(84). Over the past several years, numerical solutions by finite ele-

2. MASS TRANSFER STUDY OF A PROTOTYPE BIOASSAY IN A SPATIALLY-INDEXED MICROBEAD WELL ARRAY

ment or finite difference solution of the convective diffusion equation for the target coupled to the kinetic exchange at the patch boundary have been obtained for arbitrary values of Pe , Da and ℓ/h to obtain the surface concentration of target as a function of time and distance along the patch(66, 67, 68, 69, 71, 74, 84, 85, 86, 87), and these have been compared with the two compartment model solution and the results of binding experiments (see for example (88, 89)).

The mass transfer of target to receptors on the surface of a bead situated in a well at the flow channel bottom presents a more complex mass transfer than target transport to a patch of receptors on the channel surface, and has not been studied in the detail of the sensor patch. In this case, target streams over the top half of the bead surface; at large Pe a boundary layer does develop, but the flow is attenuated by the well walls and the target is not streamed as directly over the probe (bead) surface as in the case of the patch. Our object in this study is to compute the surface concentration of the target on the bed surface for arbitrary Da and (large) Pe by numerical simulation, and to assess the effects of the attenuated flow and compare to the transport of target to a surface patch of probes on the microchannel wall under identical conditions (same values of Da and Pe). The avidin-biotin binding experiments using the microfluidic flow cell microbead array will also be undertaken to validate the regimes drawn by the numerical simulations.

2.2 Transport Simulations

We consider first the mass transfer of target to probes on the surface of a microbead situated in an isolated, circular well located at the bottom of a mi-

2.2 Transport Simulations

crofluidic flow channel of rectangular cross section. The values for the geometric parameters are set to be equivalent to the experimental design, the channel height $h = 80 \mu\text{m}$, the well depth $d = 50 \mu\text{m}$ and diameter $2r = 70 \mu\text{m}$. The microbead with radius, $a = 42 \mu\text{m}$ is positioned along the axis of the well, and is recessed, as in the experiments, located equidistantly ($\pm 4 \mu\text{m}$) from the top and bottom of the well. The well is positioned centrally with respect to the side walls of the channel, with the well axis a distance w from the walls. A (nondimensionalized) cartesian coordinate system (lengths scaled by h) is located with an origin above the well axis at the center of the channel, with \tilde{y} along the flow direction, \tilde{z} perpendicular to the bottom wall and \tilde{x} perpendicular to the side walls. The computational domain is closed by entrance (upstream) and exit (downstream) cross sections of the channel located a distance L from the well center.

The flow of the analyte stream provides the convective flow setting for the mass transfer of the target, and is described first. The analyte is modeled as an incompressible, Newtonian fluid with the density ρ and viscosity μ of water ($\rho = 1 \text{ kg m}^{-3}$ and $\mu = 10^{-1} \text{ kg m}^{-1} \text{ sec}^{-1}$) independent of the analyte concentration. The flow through the channel is driven by a pressure gradient, and is implemented by assigning a uniform velocity U in the \tilde{y} direction across the inlet, and a zero pressure (relative to the inlet) across the exit. The flow is governed by the continuity (mass conservation) and Navier-Stokes equations(90),

$$\nabla \cdot \tilde{\mathbf{v}} = 0 \tag{2.1}$$

$$\Re \left[\frac{\partial \tilde{\mathbf{v}}}{\partial \tau'} + \tilde{\mathbf{v}} \cdot \nabla \tilde{\mathbf{v}} \right] = -\nabla \tilde{p} + \nabla^2 \tilde{\mathbf{v}} \tag{2.2}$$

where the nondimensional variables ∇ and ∇^2 are the gradient and Laplacian operators (scaled by h), $\tilde{\mathbf{v}}$ is the velocity vector (scaled by U), \tilde{p} is pressure

2. MASS TRANSFER STUDY OF A PROTOTYPE BIOASSAY IN A SPATIALLY-INDEXED MICROBEAD WELL ARRAY

(nondimensionalized by ρU^2), and τ' is time (scaled by convective time h/U) and $\Re = \frac{\rho U h}{\mu}$ is the Reynolds number. For the experimental flow conditions, typical for microfluidic screening, $U \approx 10^2 - 10^4 \mu\text{m sec}^{-1}$, the flow Reynolds number is of order $10^{-2} - 1$, and therefore the flow is primarily dominated by viscous forces retaining limited inertial effects. The continuity and Navier-Stokes equations are solved in cartesian coordinates with the inlet and outlet conditions, and boundary conditions of no slip on the interior walls of the channel and well and the bead surface. The solution is obtained numerically using finite elements, and time marching, implemented with the COMSOL Multiphysics simulation package (4.2), using both triangular and quadrilateral meshes. In the absence of the well, and when L is sufficiently large, the (steady) flow at the origin is a unidirectional Poiseuille flow through a rectangular cross section, independent of \tilde{y} and given by $\tilde{v}_y(x, z)$. The distance $L = 3 \times 10^3 \mu\text{m}$ is taken to be large enough so that this Poiseuille flow is obtained when the time step is small enough and the mesh density is fine enough, and this provides a first validation of the flow simulations. w is then taken large enough ($w = 3 \times 10^3 \mu\text{m}$) so that the Poiseuille flow becomes independent of x (at the origin), so that the side walls do not influence the flow at the well. These flow simulations (and the resulting mass transfer simulations) are therefore in the absence of hydrodynamic effects associated with the channel inlet, outlet or side walls. When the well is unoccupied, the hydrodynamics is an open cavity flow, as shown for $\Re = 1$, in Fig. 2.2(a) for the \tilde{y} component of the velocity profile (normalized by the average velocity U) as a function of \tilde{z} for $\tilde{x} = 0$ and $\tilde{y} = 0$ (the well centerline), and $\tilde{x} = 0$ and $\tilde{y} = 28/80$ corresponding to a location inside the well and between the bead and the well wall. Fig. 2.2(b) is a plot of the magnitude of the velocity field in the plane $\tilde{x} = 0$. In this plane, a

2.2 Transport Simulations

separatrix streamline dips into the well a distance \tilde{z} of $\approx .25$ on the well axis and separates recirculating flow in the cavity from the primarily unidirectional flow in the \tilde{y} direction in the channel (note the change in sign of the \tilde{y} component of velocity). The recirculation consists of one large eddy, as would be expected since the aspect ratio of the well $d/(2r) = 5/7$ is less than one, and consecutive, oppositely rotating eddies at the center develop for deep, rather than shallow wells. The \tilde{y} component of the velocity on the well axis, which is, for $\tilde{z} = -1/2$ approximately one half of the average velocity, decreases exponentially with distance $-\tilde{z}$ into the well. The flow pattern in the presence of the microbead, also for $\mathfrak{R}=1$, is also shown in Figs. 2.2(b). The separatrix streamline in the $\tilde{x} = 0$ plane is forced upwards by the bead, and a circulation develops between the microbead and the well wall, although, as evidenced by the magnitude of the y component of velocity at the off axis position ($\tilde{y} = 28/80$), is very small below the separatrix. These flow patterns make apparent that when the well is occupied by a bead, the direct streamline flow in the channel only contacts directly the microbead surface at the top of the microbead where the separatrix streamline dips along the microbead surface, and the remainder of the microbead surface is contacted by a very slow recirculating flow which separates from the mainstream.

Simulations of the rate at which targets bind to the probes on the surface of the microbeads in the wells from the analyte solution streaming over the beads is obtained by solving the convective-diffusion equation (eq. 2.3) for the mass conservation of the analyte in solution (in Cartesian coordinates). This is done using a finite element numerical simulation with forward marching in time that

2. MASS TRANSFER STUDY OF A PROTOTYPE BIOASSAY IN A SPATIALLY-INDEXED MICROBEAD WELL ARRAY

was implemented with the commercial software package COMSOL.

$$\frac{\partial \tilde{c}}{\partial \tau} + Pe \tilde{\mathbf{v}} \cdot \nabla \tilde{c} = \nabla^2 \tilde{c} \quad (2.3)$$

In the above, \tilde{c} is the concentration of target (non-dimensionalized by the inlet concentration c_o), \mathbf{v} is the steady velocity obtained above, and, as in the Introduction, $Pe = Uh/\mathcal{D}$ and time is scaled by the diffusion time $t_D = h^2/\mathcal{D}$. We assume at the inlet cross section that the concentration of target is uniform (c_o), and the distribution has relaxed completely at the exit so that the derivative with respect to the flow direction y is equal to zero. Eq. 2.3 is solved with these conditions, and assuming zero flux of solute on the interior channel and well surfaces, and equating the diffusive flux to the kinetic adsorption at the microbead surface.

$$\{\mathbf{n} \cdot \nabla \tilde{c}\}_{\text{bead}} = Da \left[\tilde{c}_s \left\{ 1 - \left[\frac{k}{1+k} \right] \tilde{\Gamma} \right\} - \frac{\tilde{\Gamma}}{1+k} \right] \quad (2.4)$$

$$\frac{\partial \tilde{\Gamma}}{\partial \tau} = \varepsilon \left[\frac{k}{1+k} \right] \{\mathbf{n} \cdot \nabla \tilde{c}\}_{\text{bead}} \quad (2.5)$$

where \mathbf{n} is the outward normal to the microbead surface, \tilde{c}_s is the nondimensional sublayer concentration and, as before, $\varepsilon = \frac{c_o h}{\Gamma_\infty}$ (Γ_∞ is the maximum surface concentration of target), $Da = \frac{k_a \Gamma_\infty h}{\mathcal{D}}$ and $\tilde{\Gamma}$ is the surface concentration scaled by the equilibrium concentration, Γ_{eq} , where $\frac{\Gamma_{eq}}{\Gamma_\infty} = \frac{k}{1+k}$ and $k = \frac{k_a c_o}{k_d}$ (k_a and k_d are the adsorption and desorption rate constants). The surface concentration is a function of the position on the bead surface, and we denote by $\bar{\Gamma}$ the average value on the bead surface. The mesh and time step are refined until $\bar{\Gamma}(\tau)$ is independent of the mesh density and the time step.

In nondimensional form, the target binding $\bar{\Gamma}(\tau)/\Gamma_\infty$ is a function of the Damkohler and Peclet numbers, k and ε . In the prototype assay experiments to

2.2 Transport Simulations

be described later, the binding equilibria is nearly irreversible ($k \gg 1$), a common characteristic of receptor-ligand binding interactions. Therefore, the simulations are performed using the approximation that k is infinite. The parameter ε scales the overall time for equilibration. In most screening applications the concentration of the target is low enough or the binding capacity large enough so that the adsorption depth, Γ_∞/c_o - the distance above the surface containing enough material to saturate the surface per unit area - is large relative to the channel height h so that $\varepsilon \ll 1$. This is also true in the experiments, and we set $\varepsilon = 0.016$ in the simulations which is the experimental value. We first examine the case of $Pe = 10$, a value at the low end of the range of values of the Peclet number in microfluidic screening. In Fig. 2.3(a) the surface concentration of targets as a function of time ($\bar{\Gamma}(\tau)$) for $Da = 1, 10$ and 10^2 for binding to the surface of a microbead in a well is shown. This binding rate on the microbead surface is compared to the binding of target from a Poiseuille flow onto a circular patch of probes situated centrally at the bottom of the microchannel wall ($\tilde{z} = -1/2$), and with a radius equal to the well radius r and with the binding capacity Γ_∞ and kinetic rate k_a identical to that on the microbead surface. In the nondimensional form presented in Fig. 2.3(a) with τ nondimensionalized by the diffusion time scale, increasing Da corresponds to a binding experiment in which the kinetic binding rate k_a is increased, with the average velocity U , concentration c_o , binding capacity Γ_∞ and diffusion coefficient \mathcal{D} held fixed. For both the circular patch and the microbead surface, the concentration of bound target increases monotonically with τ , and as Da increases, the binding rate is observed to increase. The binding of target to the surface probes is a transport process of bulk diffusion to the surface followed by the kinetic step of target-probe conjugation. The process begins as

2. MASS TRANSFER STUDY OF A PROTOTYPE BIOASSAY IN A SPATIALLY-INDEXED MICROBEAD WELL ARRAY

target in the sublayer of analyte immediately adjacent to the probe surface binds to the surface, depleting the sublayer concentration \tilde{c}_s . Depletion continues until the surface kinetic rate becomes reduced by the partial saturation of the surface, in which case bulk diffusion repopulates the sublayer until the sublayer returns to c_o (nondimensionally to one). For the smallest values of Da , kinetic exchange is much slower than bulk diffusion, and the sublayer concentration remains relatively uniform around the microbead or above the patch, eliminating diffusion barriers. In this limit, the average surface concentration is given by the exponential expression $\bar{\Gamma}(\tau)/\Gamma_\infty = 1 - e^{-\varepsilon Da \tau}$. This ideal kinetic limit represents the fastest rate at which target can bind to the surface, and this limiting envelope is shown in Fig. 2.3(a). For $Pe = 10$, this kinetic limit is only coincident with the numerical simulations for the patch and the microbeads for $Da \leq .1$ (data not shown). As Da increases to values of one and larger, the kinetic rate increases relative to diffusion and this reduces the concentration of target in the sublayer of analyte immediately adjacent to the surface, c_s , to values less than c_o , creating a diffusive barrier to binding. Since the sublayer concentration is no longer equal to the farfield bulk concentration, but is smaller, the numerically simulated mixed diffusive-kinetic binding rate falls below the ideal kinetic limit, as is evident for $Da = 1, 10$ and 10^2 in Fig. 2.3(b). For increasing Da , the sublayer concentration decreases and this has two consequences: First the numerically simulated mixed binding rate increases as the diffusive flux to the surface is greater the lower the sublayer concentration. Second, relative to the ideal kinetic limit, the mixed simulated binding becomes increasingly slower (Fig. 2.3(a)) since the kinetic limit assumes the sublayer concentration is equal to the farfield concentration. Fig. 2.3(a) also makes clear that, because target binds more quickly to the patch in-

terface than to the microbead surface, the diffusive barrier which develops around the microbead is much larger than the diffusive barrier which develops over the patch.

The diffusive flux to the surface of the microbead is smaller than to the surface of the patch because the diffusive transport in the case of a patch is entirely through a convective boundary layer, while diffusion to the microbead surface is through a convective boundary layer over the top of the bead exposed to the flow, but through a trapped, slowly recirculating flow which surrounds the bottom part of the bead. The bulk concentration fields and the surface concentrations provide more detail and insight into this difference in mass transfer between the two geometries. Consider first binding to the circular patch of probes; the concentration above the patch in the plane $\tilde{x} = 0$ (perpendicular to the microchannel wall, along the flow and at the center of the patch), and the surface concentration in the plane $\tilde{z} = -1/2$ (the channel wall) for $Da = 10$ and for three nondimensional times, is shown in Figure 2.3(b). For this relatively small value of Pe (10), the characteristic patch size in the flow direction ($\ell \sim 2r$), relative to the channel cross section h ($2r/h = 7/8$), is still less than Pe , and as discussed in the Introduction for binding to a patch, for $\ell/h < Pe$, a boundary layer forms over the patch and extends into the streaming flow but does not extend to the opposite end of the channel, as is clear in Figure 2.3(b). The concentration in the boundary layer above the patch shows the initial depletion in the concentration next to the surface due to the large value of Da , followed by an increase in the sublayer concentration as the surface begins to saturate. As the boundary layer is thinner at the upstream part of the patch, the diffusive flux is greater at the front end of the patch, and the surface concentration increases and saturates from

2. MASS TRANSFER STUDY OF A PROTOTYPE BIOASSAY IN A SPATIALLY-INDEXED MICROBEAD WELL ARRAY

the upstream to the downstream end of the patch, Figure 2.3(b).

For the binding of the target to the microbead surface, the concentration field in the plane $\tilde{x} = 0$ and the surface concentration along the hemisphere $\tilde{x} > 0$ (projected onto a circle) for $Da = 10$ and for same three times as depicted for the patch, are shown in Fig. 2.3(c). Again, the characteristic length of the probe area in the streamwise direction $\ell \sim 2a$ divided by h ($\ell/h = 1/2$) is smaller than Pe , and a boundary layer forms above the separatrix. In the region in which the separatrix is directly attached to the microbead surface, target diffuses directly through the convective boundary layer to the surface, and the diffusive flux is the largest and the binding rate to the surface the greatest. This resembles the transport to the surface of the patch. At the upstream and downstream parts of the well where the separatrix dips into the well, target diffuses through the convective boundary layer and then through the slowly recirculating liquid surrounding the lower half of the microbead in the well to reach the bead surface. The diffusion through the essentially stagnant liquid reduces the diffusive flux, and the liquid in the well quickly becomes depleted of target for this relatively large value of Da . As a result, while the binding rate at the top part of the microbead surface increases rapidly, the surface concentration along the lower part increases much more slowly (cf. the projection of the surface concentration), providing an overall reduction in the average rate of binding ($\bar{\Gamma}(\tau)$) compared to the rate of binding for a patch. The depletion of target in the stagnant liquid in the well is slowly replenished, and the equilibration takes a much longer time relative to either the patch equilibration or the ideal kinetic limit. As with the patch geometry, the binding to the surface is asymmetric with respect to the flow direction. The top part of the microbead, in contact with the thinner part of the boundary layer and

having the larger diffusive flux, has a greater rate of binding relative to the downstream part of the microbead, in contact with the thicker part of the boundary layer and a reduced diffusive flux. As Da decreases and the ideal kinetic limit is approached, the effect of the stagnant layer around the microbead in the well in decreasing the diffusive flux is reduced, and the microbead and patch geometries show similar binding rates. For $Da \leq .1$ (data not shown), the concentration of target in the stagnant layer is approximately the farfield target concentration due to the large kinetic barrier (relative to diffusion), and the binding rate becomes identical to the kinetic limit.

When the Pe number is increased to a value of 10^4 (Fig. 2.4), the transport picture changes significantly for both the patch and microbead geometries. As discussed in the Introduction, when, for large Pe , the characteristic streamwise length of the probe area, ℓ , divided by the channel height h is much smaller than Pe , convective boundary layers of target over the probe surface develop and become very thin. The corresponding diffusive flux of target through the layer becomes much larger relative to order one Pe , and this increases the binding rate of the target to the probe surface. In addition, because of the enhanced diffusion rate, for any value of Da (and particularly large values), the sublayer concentration of target adjoining the probe surface is not depleted by kinetic adsorption to the extent that it is when $Pe = O(1)$, and the mixed diffusive-kinetic binding becomes closer to the ideal kinetic limit. These results are evident in Fig. 2.4(a) for $\bar{\Gamma}(\tau)$ which shows clearly that, for $Pe = 10^4$, the binding rates for both the patch and the microbead geometries ($\ell/h \ll Pe$) are much faster than for $Pe = 10$ (compare Figure 2.3(a)) at the same values of Da , and are closer to the ideal kinetic limit, and Figure 2.4(b) where the boundary layers are much

2. MASS TRANSFER STUDY OF A PROTOTYPE BIOASSAY IN A SPATIALLY-INDEXED MICROBEAD WELL ARRAY

thinner and depletion less evident when compared with $Pe = 10$ and $Da = 10$ (compare Figure 2.3(b)). Consider in particular first the patch geometry. For $Da = 1$, the mixed diffusive-kinetic binding rate is on the kinetic envelope. This is in agreement with the criteria established in the Introduction, for which kinetically limited transport is valid for streamwise patch lengths ℓ satisfying $\ell/h \ll Pe$ when $Da \left\{ \frac{\ell/h}{Pe} \right\}^{1/3} \ll 1$ (for $Da = 1$, $Da \left\{ \frac{\ell/h}{Pe} \right\}^{1/3} \approx 0.1$). For the larger values of Da in Fig. 2.4(a), $Da \left\{ \frac{\ell/h}{Pe} \right\}^{1/3} \geq 1$, the kinetically limited criteria is not satisfied, and as is evident in the figure, the mixed diffusive-kinetic patch simulations are below the ideal kinetic limit. In the case of binding to the microbead surface, some depletion of target still occurs in the stagnant liquid surrounding the lower part of the microbead, due to the slower diffusive transport in this liquid. The liquid inside the well at the upstream side appears to be more depleted of target compared to the liquid at the opposite side, and correspondingly the binding rate is slower on the lower part of the upstream end of the microbead surface relative to the bottom part of the downstream end. This contrasts with the case of $Pe = 10$ (Figs. 2.3(c)) in which depletion and binding were more symmetrical. One reason for this asymmetry may be due to the fact that the boundary layer along the separatrix at the upstream side of the well is very thin due to the high Pe and follows the contour of the separatrix streamline which dips into and out of the well just upstream of the microbead. As a result, a strong (lateral, y directed) diffusive flux is directed to the microbead surface along the ascending part of the streamline (i.e. the part that moves out of the well and just next to the target-binding bead surface) reducing the z directed flux through the separatrix required to bring target to the lower part of the microbead on the upstream side. When

the Peclet number is small and equal to 10, the boundary layer is much thicker and extends well above the separatrix at the upstream side (Figure 2.3(c)) and lateral diffusion is not as significant and transport is principally in the downward z direction. In any case, the reduced diffusive flux through the stagnant layer surrounding the microbead in the well accounts for a large barrier, and kinetically limited transport is only observed for Da of approximately 0.5.

The important conclusion which can be drawn from these simulations is that the diffusive barriers to mass transfer of target to the surface of a microbead in a well at the bottom of a microfluidic channel due to the stagnant layer of analyte in the well can significantly inhibit the binding rate relative to the transport to a patch on the bottom surface of the channel. As such, only very slow binding rates (low Da) or large throughputs (high Pe) can ensure for the microbead geometry kinetically limited binding conditions. All the simulations presented here are for a single well.

2.3 Experimental Setup

2.3.1 Device design

The microfluidic geometry consists of an open duct channel with lateral dimensions of 15 x 5 mm and a height of 100 μm . The bottom wall of the channel is a flat surface populated by a uniform array of circular wells 70 μm in diameter and 50 μm deep. The lateral pitch of the array is 250 μm and sequential rows are offset by 125 μm . The channel is connected to four ports. Entrance and exit ports are located at opposite ends of the channel to control microbead deposition rates, remove excess microbeads from the surface, and introduce analyte solution using

2. MASS TRANSFER STUDY OF A PROTOTYPE BIOASSAY IN A SPATIALLY-INDEXED MICROBEAD WELL ARRAY

syringe pumps. Ports located on the sides of the channel are used to introduce the different sets of microbeads, with each set of beads connected to a dedicated port to avoid reintroduction of beads after indexing.

2.3.2 Device fabrication

The microfluidic devices used in the experiments were constructed from two layers of polydimethylsiloxane (PDMS) via soft lithography. SU8 2050 negative tone photoresist (Microchem) was spin-coated (Laurell) on 3" silicon wafers at the spin speed specified by the manufacturer to produce uniform films of 100 μm thickness. After a subsequent soft-bake step to uniformly evaporate solvent from the film using hot plates, the unpolymerized photoresist was lithographically patterned using contact exposure of transparency masks (Pageworks) with a collimated xenon mercury light source (OAI) passed through a 360 nm long pass filter (Omega Optical). The use of the filter eliminates UV light below 350 nm that would otherwise overexpose the photoresist due to its higher absorbance at lower wavelengths. It also facilitates accurate calculation of the the exposure time required to polymerize the photoresist. Negative tone photoresists utilize UV light to initiate a free radical polymerization reaction in the exposed regions of the film. After exposure, the film is heated to accelerate and finish the reaction. The photoresist is then developed to remove the unexposed regions of the photoresist film by immersing the wafer in solvent. The developed photoresist is rinsed and dried before being returned to the hot plate at an elevated temperature to ensure permanent adhesion between the crosslinked SU8 epoxy and the silicon substrate. The resulting pattern contains the negative relief of the microfluidic geometry and is robust enough to serve as a reusable mold for the

casting, polymerization and removal of the PDMS layers.

The PDMS layers (Sylgard 184) are fabricated from a 10:1 by mass ratio of dimethylsiloxane base and curing agent. The two components are mixed and degassed (Thinky), then poured over the SU8 molds and further degassed using a vacuum pump. The molds were incubated at 65 °C for two hours to polymerize the PDMS before the patterned layers were cut and peeled from the molds using a scalpel. To enable the microfluidic channel to be connected to external fluid flows, access ports were added to the upper layer containing the channel using a 1.5 mm biopsy punch (Harris Uni-Core). The channel was then sealed by bonding the two PDMS layers together. This was accomplished by exposing the surfaces to be bonded to an oxygen plasma for 30 s (Harrick) and then bringing them into conformal contact to form the microchannel. The oxygen plasma reacts with the PDMS to form silanol groups on the surfaces, which react with silanol groups on the opposite surface to form covalent siloxane bonds that permanently seal the microchannel. To facilitate observation using a microscope stage, each device was mounted on a standard glass microscope slide using an additional plasma exposure step to again produce siloxane bonds between the (glass and PDMS) surfaces.

2.3.3 Microbead functionalization

Glass microbeads with a mean diameter of 42.5 μm (Duke Scientific) were used in this experiment. They were selected for ease of functionalization and sized so that only a single bead could occupy each well. Glass beads have the additional advantage of a large density difference with water to facilitate gravity-based capture in the wells of the array. The beads were first cleaned in an aqueous solution of 4

2. MASS TRANSFER STUDY OF A PROTOTYPE BIOASSAY IN A SPATIALLY-INDEXED MICROBEAD WELL ARRAY

% NH_4OH and 4 % H_2O_2 (w/w) heated to 70 °C for 30 minutes. The beads were then washed twice with deionized water, twice with ethanol, centrifuged, washed twice with chloroform and centrifuged. They were then suspended in a 5 mM solution of aminopropyltrimethoxysilane (APS) in chloroform for one hour to graft amine groups to the surface. To remove unbound APS, the beads were washed and sonicated with chloroform. They were then centrifuged, washed twice with ethanol, twice with water and twice with dimethylformamide (DMF). Depending on the desired functionalization, the beads were then suspended in a 1 mg/mL solution of NHS-PEG, NHS-PEG-Biotin, or NHS-Fluorescein for one hour. To ensure no photobleaching of the fluorescein occurred, the vial was covered with aluminum foil. The beads were then washed three times with deionized water and stored in a refrigerator at 4 °C until used.

2.3.4 Microbead capture and Spatial Indexing Without Encoding

To introduce the functionalized beads into the microfluidic channel, the device is submerged in deionized water under a vacuum to remove air bubbles. Polyethylene tubing is inserted into the access ports, and the tubing connecting to the entrance port is attached to a plastic syringe controlled by a syringe pump (Harvard Apparatus). The bead sets are suspended in water by magnetic stirring and drawn into 250 and 500 μL glass syringes (Hamilton). The glass syringe is then connected to the loading port on the side of the microchannel, elevated above the device and positioned with the needle facing down so that the beads fall out of the needle, into the tubing and down towards the microchannel under gravity.

2.3 Experimental Setup

Fluid flow in the channel is initiated at $10 \mu\text{L}/\text{min}$ so that the beads entering the channel are immediately propelled along the surface of the well array and begin depositing into the wells. Beads that are not captured by the wells accumulate in the exit port and are not carried into the exit tubing because of the moderate flow rate. They are returned to the channel by reversing the flow direction using the syringe pump so that the beads are directed towards the entrance port. The flow direction is switched repeatedly until the desired well occupancy is achieved. The flow rate is then increased to $100 \mu\text{L}/\text{min}$ (in the forward direction), resulting in the propulsion of the beads out of the exit port and into the exit tubing. After these excess beads have been removed, the partially occupied well array is imaged to index the locations of the beads from that bead set using a 10x inverted microscope objective (Nikon) connected to a CCD camera (Scion) controlled by ImageJ software (NIH). This setup produces images with a field of view encompassing 20 wells (5×4). The second bead set is then deposited into the microchannel and the loading process is repeated until all of the empty wells are occupied. Residual beads are washed off, and the well array is again imaged to verify the locations of beads from each set. The imaging is done in epifluorescent mode using a 100 watt mercury source and a B-2A filter block (Nikon) to selectively excite and detect the fluorescein-labeled and Texas Red-conjugated beads.

The ability of the well geometry to capture and retain multiple bead sets to create a spatially-indexed array of bead functionality without microbead encoding is demonstrated in Figure 2.5. The first bead set introduced into the device is functionalized with fluorescein as discussed earlier. Multiple beads are captured by the well array, but vacant wells remain to allow subsequent capture of the second bead set. Uncaptured fluorescein beads remaining in the device are

2. MASS TRANSFER STUDY OF A PROTOTYPE BIOASSAY IN A SPATIALLY-INDEXED MICROBEAD WELL ARRAY

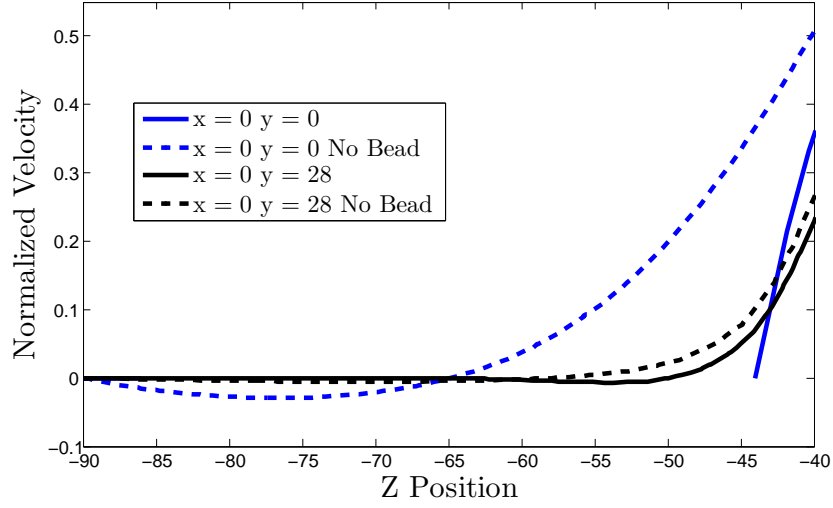
successfully removed without displacing the captured beads. The locations of the captured beads are then recorded as shown in Figures 2.5 for two different locations within the well array. The second bead set, functionalized with PEG, is then introduced into the array. These beads are captured in the remaining wells to complete the index of bead functionality according to well location.

2.3.5 Prototype assay

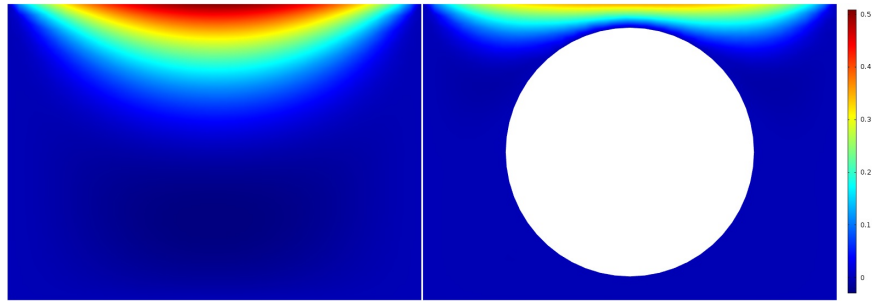
The prototype assay conjugating NeutrAvidin protein labeled with Texas Red fluorophore to biotin-functionalized beads was performed under different Pe values to corroborate the results of the finite element simulations. The binding curves shown in Figure 2.6 represents the mean normalized intensity values of the individual beads in well arrays for experiments performed at $Pe = 5600$ and $Pe = 56$. These data points were compared to binding curves obtained by COMSOL for the specified Pe value and different values of Da to determine the value of Da at which both experimentally measured binding curves match their predicted curves. The adsorption rate constant k_a corresponding to the matching value of Da is $k_a = 7 \times 10^4 M^{-1} s^{-1}$.

2.4 Conclusions

We have demonstrated a spatially-indexed microbead array via sequential deposition of microbeads into a recessed well geometry. Finite element simulations used to identify the flow conditions and microbead receptor density required for the observed ligand-receptor conjugation to approach the kinetically-limited reaction rate are identified and validated using a prototype assay of NeutrAvidin binding to biotin on the microbead surfaces.



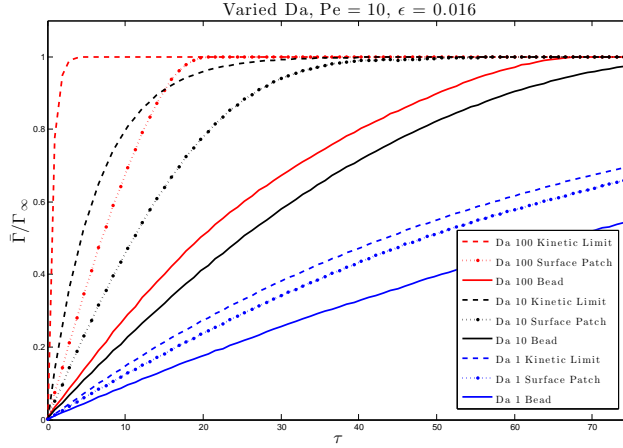
(a)



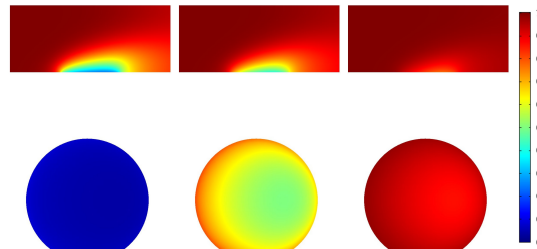
(b)

Figure 2.2: (a) Velocity in the \tilde{y} direction (normalized by the average velocity U) as a function of \tilde{z} , in the plane $\tilde{x} = 0$, at the center of the well ($\tilde{y} = 0$) and at an upstream location inside the well and between the bead and the well wall ($\tilde{y}=28/80$) in the presence and absence of a microbead. (b) Magnitude of the velocity in the plane $\tilde{x} = 0$ inside the well in the absence and presence of a microbead. All simulations are for $\mathfrak{Re}=1$.

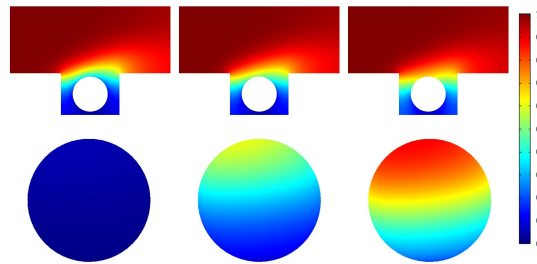
2. MASS TRANSFER STUDY OF A PROTOTYPE BIOASSAY IN A SPATIALLY-INDEXED MICROBEAD WELL ARRAY



(a)

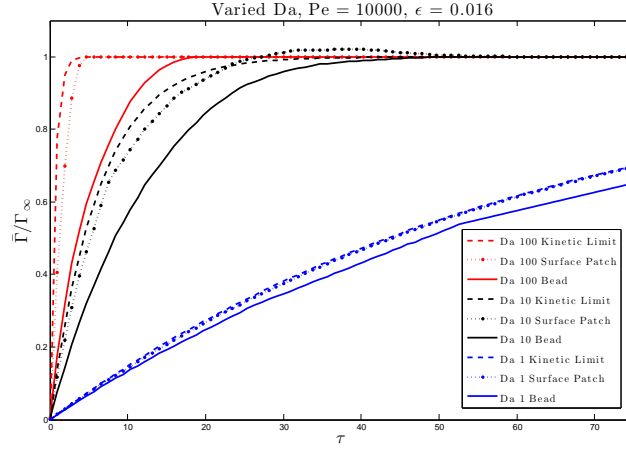


(b)

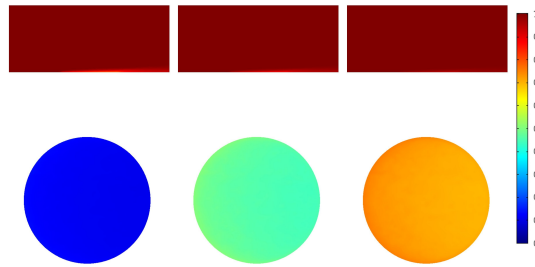


(c)

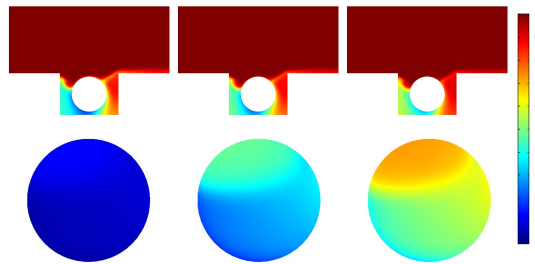
Figure 2.3: Target binding to probes on a circular patch on a microchannel wall and on the surface of a microbead in the well for $Pe = 10$: (a) The average nondimensional surface concentration on a surface patch and the surface of the microbead, $\bar{\Gamma}$, as a function of τ for $Da = 10, 10^2$ and 10^3 . (b)-(c) Target concentration boundary layers around, and the spatial distribution along either a surface patch (b), or the microbead in the well (c) for $\tau = 1, 15$ and 30 and $Da = 10$. For the microbead, the concentration boundary layer is in the plane $\tilde{x}=0$, and the surface concentration is the projection of the concentration on the hemisphere $\tilde{x} > 0$. $\varepsilon = .016$ and $k \rightarrow \infty$. Simulations at additional Pe and Da values are presented in Appendix A.



(a)



(b)



(c)

Figure 2.4: Target binding to probes on a circular patch on a microchannel wall and on the surface of a microbead in the well for $Pe = 10^4$: (a) The average nondimensional surface concentration on a surface patch and the surface of the microbead, $\bar{\Gamma}$, as a function of τ for $Da = 10, 10^2$ and 10^3 . (b) Target concentration boundary layers around, and the spatial distribution along, either a surface patch (b) or the microbead in the well (c) for $\tau = 1, 5$ and 10 and $Da = 10$. For the microbead, the concentration boundary layer is in the plane $\tilde{x}=0$, and the surface concentration is the projection of the concentration on the hemisphere $\tilde{x} > 0$. $\epsilon = .016$ and $k \rightarrow \infty$.

2. MASS TRANSFER STUDY OF A PROTOTYPE BIOASSAY IN A SPATIALLY-INDEXED MICROBEAD WELL ARRAY

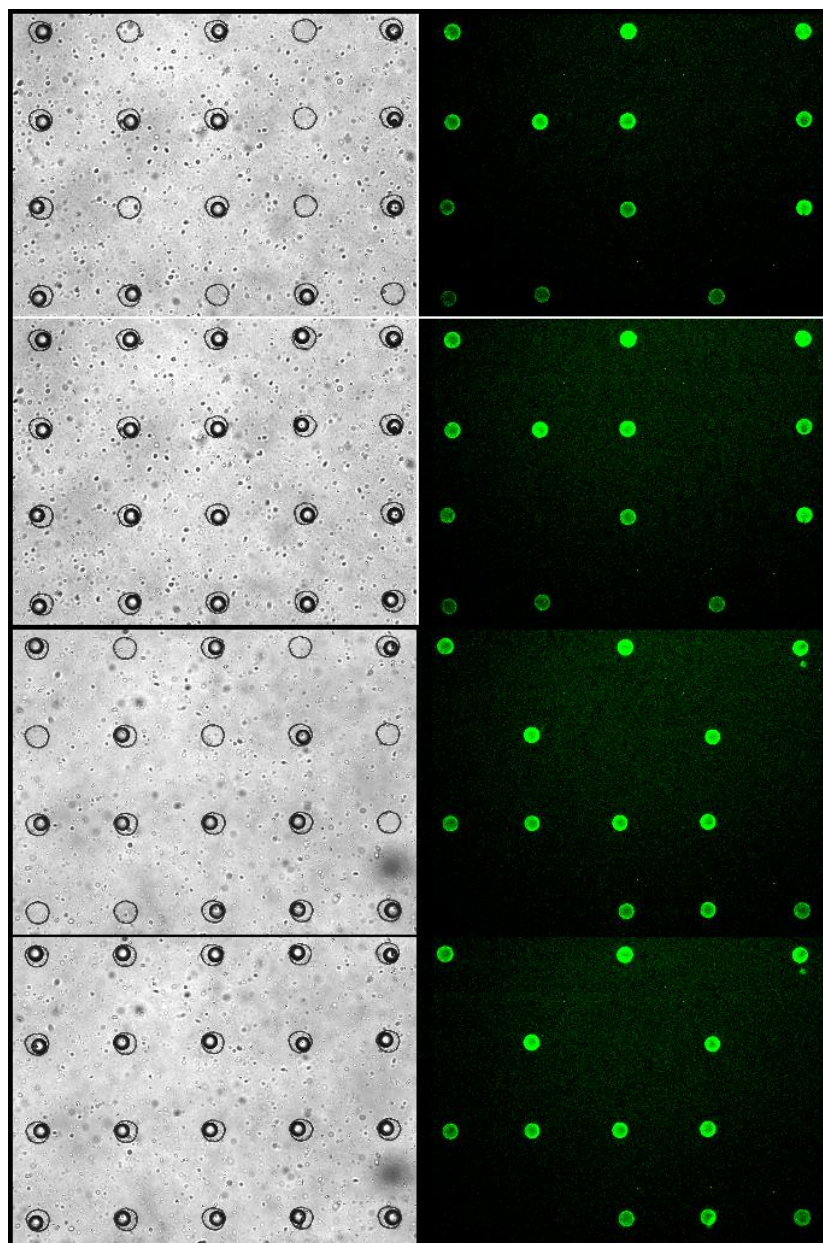


Figure 2.5: Bright field and fluorescence images of sequential bead array in two fields of view.

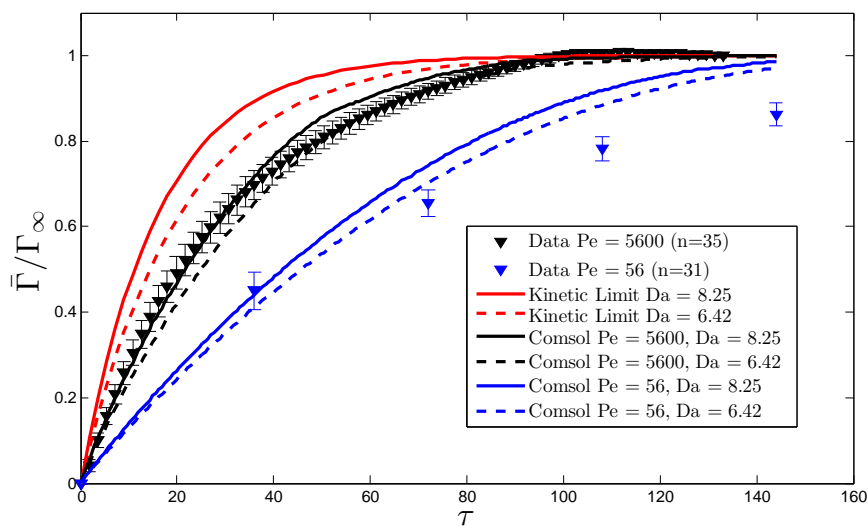


Figure 2.6: Normalized binding curves for prototype NeutrAvidin-biotin assay compared to finite element simulation results at equal Pe . $C_\infty = 4.2 \times 10^{-9}M$.

2. MASS TRANSFER STUDY OF A PROTOTYPE BIOASSAY IN A SPATIALLY-INDEXED MICROBEAD WELL ARRAY

3

Hydrodynamic Slip at an Oil/Polydimethylsiloxane Surface From Measurements of the Dielectrophoretic Motion of Water Droplets

3.1 Background

Recently, new attention (91, 92) has been paid to the possibility of hydrodynamic slip at an interface between a stationary solid surface and a “simple” (non-polymeric) liquid moving over the surface. The consideration of boundary slip began with the continuum level formulation of the Navier slip condition for a Newtonian fluid, which equated the fluid velocity tangent to the surface, v_s , to the boundary tangential stress, τ_s , by the slip coefficient λ , i.e. $v_s = \frac{\lambda}{\mu}\tau_s$ where μ is the fluid viscosity and λ has units of length. Since this formulation, experimental studies have made clear that the “no-slip” condition of $\lambda = 0$ is sufficient to accurately model most macroscopic flows with length scales in the range of mil-

3. HYDRODYNAMIC SLIP AT AN OIL/POLYDIMETHYLSILOXANE SURFACE FROM MEASUREMENTS OF THE DIELECTROPHORETIC MOTION OF WATER DROPLETS

limeters to meters, with the exception of contact line motion (93) and the flow of polymeric (non-Newtonian) fluids (94). However, recent molecular dynamics simulations on atomically smooth surfaces have demonstrated slip on the molecular scale, and calculated λ as a function of the strength of the liquid-solid interaction (95, 96, 97). For strong liquid-solid interactions which characterize complete or strong wetting of the liquid on the solid surface, slip lengths are of the order of only a few molecular diameters ($\mathcal{O}(1 \text{ nm})$), while relatively weaker interactions of partially wetting fluids have slip lengths extending tens of diameters ($\mathcal{O}(10 \text{ nm})$). Current tools for measuring λ include particle image velocimetry (PIV), image velocimetry enhanced with evanescent near-field illumination at the surface, and atomic force microscope (AFM) and surface force apparatus (SF) measurements (98, 99, 100, 101, 102, 103, 104, 105, 106, 107, 108, 109). Several experiments are consistent with the MD calculations. For smooth surfaces of a wetting liquid, e.g. water flowing along a hydrophilic surface, either zero slip or coefficients less than a few nanometers are recorded, while water over a partially wetting hydrophobic surface (e.g. self-assembled octadecyl silane (OTS) monolayers) obtain slip lengths of tens of nanometers, e.g. (108, 110, 111, 112). For nonpolar liquids wetting smooth hydrophobic surfaces (the weakest liquid/surface interactions), slip lengths are of the order of a few tens of nanometers (113, 114, 115).

“Giant” slip ($\lambda \sim \mathcal{O}(1 \mu\text{m})$ or larger) is the subject of great interest for its application to reducing surface friction in micro and nanofluidic channel flows. Large slip can be achieved when low friction air layers are situated between the liquid and the surface a circumstance which arises when a population of nanoscopic gaseous domains adhere to a surface, or air becomes trapped in a micro or nano-textured surface that is not wet by the liquid (superhydrophobicity) (116). AFM

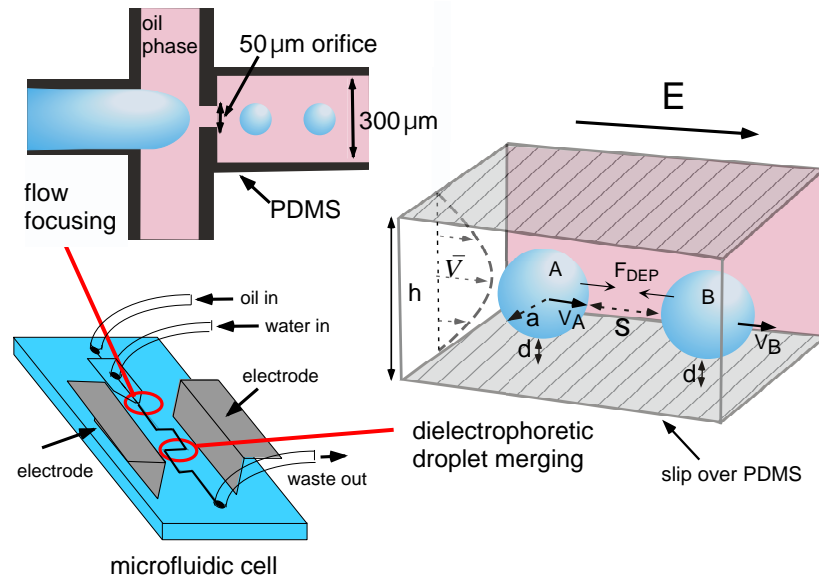


Figure 3.1: Measurement of microchannel slip at an oil/PDMS surface by observing the dielectrophoretic merging of water droplets in oil moving in close proximity to the PDMS channel wall.

studies have provided direct evidence of nanoscopic gaseous domains, primarily at the interface between water and a hydrophobic surface (117). AFM measurements have also verified the reduction in surface friction (118), and nanoscopic gas domains have been suggested (119) as one reason why some measurements of slip at the water/hydrophobic solid surface (120, 121) obtain one micron or larger slip lengths. Hydrophobic, textured surfaces filled with air provide a more reproducible method for generating large slip, (122, 123, 124, 125), and theoretical MD and continuum studies of model textures (see for example (126, 127)) demonstrate that large slip requires the solid fraction of the surface to be a few percent.

Little attention has been paid to obtaining giant slip when nonpolar liquids

3. HYDRODYNAMIC SLIP AT AN OIL/POLYDIMETHYLSILOXANE SURFACE FROM MEASUREMENTS OF THE DIELECTROPHORETIC MOTION OF WATER DROPLETS

slip over a surface (“oil slippery surfaces”), although significant interest is developing due to the emergence of dropwise microfluidic platforms which are based on water droplets moving in a continuous oil stream (128). Generating gaseous domains at the surface is the key to large slip, and one method for generating a significant coverage of nanobubbles on surfaces submerged in oil is to nucleate them spontaneously on oil contact. Spontaneous nonequilibrium formation of nanobubbles at a surface occurs, for example, when an air saturated liquid (e.g. ethanol) is displaced by a second, miscible, liquid (e.g. water), also saturated with air, but with a lower solubility (117) and nanobubbles nucleate to accommodate the reduced solubility of the displacing phase. In this chapter we demonstrate that a nanoporous, hydrophobic polymer, polydimethylsiloxane (PDMS), which has a significant permeability to air because of the hydrophobicity of the polymer and a relatively large free volume (129), permits oil to slip over its surface with an order one micron slip length. When oil contacts the surface of an air-equilibrated PDMS substrate, air is released as nanobubbles to the oil/PDMS surface. The driving force for this release derives from the fact that the PDMS is also permeable to oil because of its hydrophobic nanoporosity, and diffusion of oil into the nanopores on the contact of oil to the surface displaces the air to the interface.

We demonstrate in particular oil slip at the inside surface of a microchannel formed in a PDMS monolith fabricated by soft lithography. We use a viscous mineral oil ($\mu_{Oil} \approx 100\mu_{H_2O}$), a mix of high and low molecular weight olefins, which does not macroscopically swell the PDMS (130) and distort the surface from the atomically smooth topology normally evident in AFM measurements but can still displace air in PDMS by the solubilization of small linear alkanes in the oil. The microfluidic arrangement is shown in Fig. 3.1. (Additional de-

tails are given in B.) Using optical microscopy, we measure, in a PDMS channel of rectangular cross section with height h ($100\ \mu\text{m}$) and wide width w ($300\ \mu\text{m}$), the edge-to-edge separation distance $s(t)$ of pairs of nearly occluding water droplets (“A” and “B”) which are entrained in a mineral oil stream and are driven together by a dielectrophoretic (DEP) force of attraction, F_{DEP} . This force is due to an electric field \mathcal{E} applied parallel to the bottom wall of the channel and along the flow direction. The merging droplet pair is part of a single file droplet train, formed upstream by flow focusing (131) of oil and water streams (flow rates equal to $0.4\text{-}1\ \mu\ell/\text{min}$ and $0.04\text{-}0.1\ \mu\ell/\text{min}$, respectively), through an orifice $50\ \mu\text{m}$ in width. The focusing forms droplets with radius a equal to approximately $40\ \mu\text{m}$, which are separated by a few radii, and flow at the average stream velocity \bar{V} of approximately $250\text{ - }500\ \mu\text{m}/\text{sec}$. The electric field is applied to switchback flow lanes at the downstream end of the chip by a voltage \mathcal{V} set across parallel copper strip electrodes inserted through the PDMS (a dielectric) to insure a uniform field across the flow channels. Relative to the aqueous phase which is de-ionized water, the oil is nonconducting and the field polarizes each of the droplets of the pair into dipoles. In the flow lanes parallel to \mathcal{E} , the polarized drops are aligned with \mathcal{E} and attract each other, creating the dielectrophoretic force. Prior to the application of the field, the train flow is observed, and when a pair are observed to pair-off to a relatively close separation (less than one radius) due to flow disturbances, the field is applied to merge the pair, and a video recording is made with a high speed camera. At the time of application of the field, the droplets, heavier than the oil ($\rho_{H_2O} = 10^3\ \text{kg}/\text{m}^3$ and $\rho_{oil} = 8.75 \times 10^2\ \text{kg}/\text{m}^3$) have settled to a separation distance d from the bottom wall of the microchannel which is determined by their settling velocity and the transit time, τ , from their

3. HYDRODYNAMIC SLIP AT AN OIL/POLYDIMETHYLSILOXANE SURFACE FROM MEASUREMENTS OF THE DIELECTROPHORETIC MOTION OF WATER DROPLETS

formation at the orifice until application of the field and is of the order of a few hundred nanometers. At these distances from the wall, the approach velocity $V_A - V_B = \frac{ds}{dt}$ due to the DEP force is affected (as we show by numerical solution of the hydrodynamic equations) by the drag, against the bottom wall, of the intervening oil between the droplet and the wall, and the slip on this wall. From comparison of $s(t)$ with numerical solutions, λ is obtained with a precision which can distinguish a micron size slip length. We also measure the slip when the bottom surface is a glass slide, functionalized with octadecyltrichlorosilane (OTS), which we do not expect to nucleate nanobubbles at the surface because of low air permeability, and we find zero slip to the precision of the measurement.

One illustrative data set is given in Fig. 3.2 (The video is in the supplemental material). An edge detection routine is used to determine the droplet perimeters from which the size of the merging droplets a and the pair separation distance $s(t)$ are computed. The separation distance is shown in Fig. 3.2, and the relative approach velocity is approximately $40 \mu\text{m}/\text{sec}$. To obtain different data sets of $s(t)$ corresponding to different droplet radii or droplet-wall separations d (transit times τ), the oil and water flow rates at the flow focusing orifice are changed, or the merging at different switchback lanes is observed.

A nonionic surfactant (Span 80, sorbitan monooleate) is dissolved in the mineral oil at a concentration $C = 2.3 \times 10^{-2}$ M, well above its critical micelle concentration (CMC) ($CMC = 2.3 \times 10^{-4}$ M). At and above the CMC the equilibrium tension γ is 3 mN/m and the equilibrium surface concentration $\Gamma_{CMC} = 3.6 \times 10^{-6}$ mole/m²; dynamic tension measurements indicate the desorption rate constant, k_d , is $\mathcal{O}(10^{-3} \text{ sec}^{-1})$ (132). The time scale for convection of surfactant along the droplet a/\bar{V} , $\mathcal{O}(10^{-1} \text{ sec})$, is much shorter than the desorption time, $1/k_d$, there-

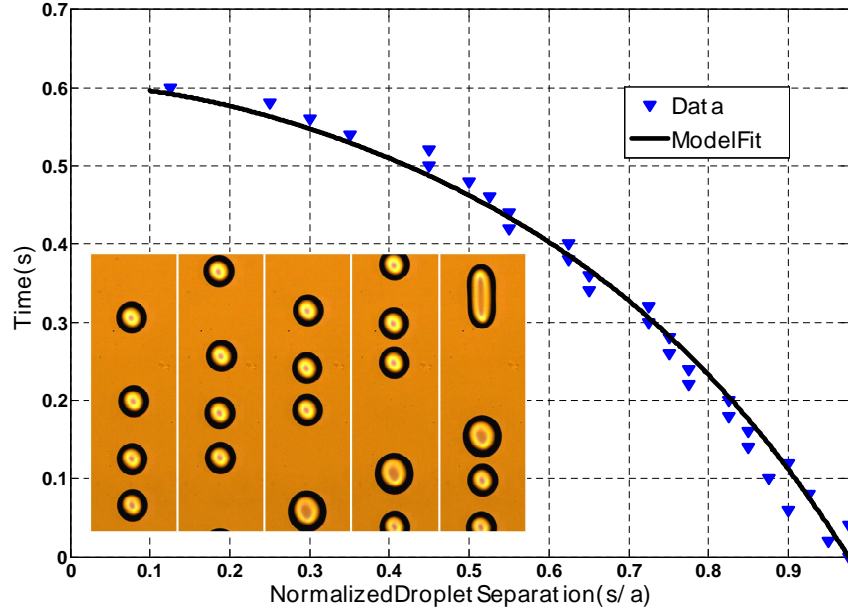


Figure 3.2: Dielectrophoretic merging of $40 \mu\text{m}$ radius droplets at the oil/PDMS surface: Frame captures of the pairwise merging at time intervals of .12 sec, flow direction from bottom to top and time (t) as function of the measured edge-to-edge scaled separation s/a from the images. The continuous line is a fit for a value for the droplet-wall drag coefficient, α .

fore surfactant collects at the trailing edge of the droplet, causing the tension to be larger at the front than the back. This Marangoni gradient opposes the surface flow and immobilizes the interface because the ratio of the characteristic scale for the retarding tension gradient, $RT\Gamma_{CMC}/a$, to the oil viscous stress on the droplet surface, $\mu_{oil}\bar{V}/a$, the Marangoni number ($Ma = \frac{RT\Gamma_{CMC}}{\mu_{oil}\bar{V}}$) is $\mathcal{O}(10^2)$. Hence the pairwise hydrodynamic interaction is one of interfacially rigid droplets.

To compare the data sets of $s(t)$ to a hydrodynamic model of the merging process, the applied field and droplet-wall separation distance d have to be de-

3. HYDRODYNAMIC SLIP AT AN OIL/POLYDIMETHYLSILOXANE SURFACE FROM MEASUREMENTS OF THE DIELECTROPHORETIC MOTION OF WATER DROPLETS

terminated. Since the PDMS and oil are dielectric phases, they act as capacitors in series, and therefore $\mathcal{E} = \mathcal{V}\{2L_{PDMS}(\varepsilon_{Oil}/\varepsilon_{PDMS}) + L_C\}^{-1}$ with ε_{PDMS} and ε_{Oil} the dielectric constants for the PDMS and oil (2.65 and 2.18, respectively), and L_c and L_{PDMS} are, respectively, the length of the channel and the distance between the electrode and the channel (6 mm and 4.5 mm, respectively). An AC electric potential \mathcal{V} (500 Hz, 5 kV sine) is applied across the electrodes, resulting in an average field strength $\mathcal{E} = 365$ V/mm. While an alternating potential is used to prevent any residual charge accumulation in the PDMS and oil, the oscillation does not affect the merging process since F_{DEP} is proportional to the square of the field, and the oscillation period is much faster than the time scale for the merging. To obtain d , we assume that at the flow-focusing orifice the droplets detach symmetrically from the top and bottom walls of the channel and are therefore initially centered at the midplane, hence the initial separation d_i is $h/2 - a$. Clearly, each drop is not precisely released at the center of the channel, but statistically above and below the midplane. However, our data analysis will average over several data sets at a nominal value of d which should account for this statistical variation. The distance d , accounting for only the resistance of the lower wall, is, for $d/a \ll 1$, given by (133) $\ln \left\{ \frac{d}{d_i} \right\} = -\frac{2ga(\rho_{H_2O} - \rho_{Oil})}{9\mu_{Oil}}\tau$ where g is the acceleration of gravity. (Values for d/a are less than 0.25, for which this expression is accurate. The equation for d can be corrected to include wall-slip and the effect of the resistance due to the opposite channel wall, but these corrections, if included, can be shown to be negligible in the determination of d (134).

The droplet hydrodynamics is in the Stokes regime of negligible inertia ($Re = \frac{\rho_{Oil}\bar{V}h}{\mu_{Oil}} = \mathcal{O}(10^{-4})$), and the droplets remain spherical until the onset of coalescence (cf. Fig. 3.2) as the viscous forces are smaller than the tension force

3.1 Background

(capillary number, $Ca = \frac{\mu_{oil}\bar{V}}{\gamma} = \mathcal{O}(10^{-2})$) and the Maxwell electrical stresses are smaller than the tension force (electric Bond number, $Bo = \frac{\varepsilon_o\varepsilon_{oil}\mathcal{E}^2a}{\gamma} = \mathcal{O}(10^{-2})$), where ε_o is the permittivity of free space. The total fluid drag exerted on each of the droplets as they merge can be calculated from the sum of the fluid drags (formulated as a drag coefficient f multiplied by $6\pi\mu_{oil}a$ and a velocity) in three flow configurations (Fig. 3.3): the Poiseuille flow over fixed droplets (f_p), and the motions, stationary in the farfield, of A with B fixed or B with A fixed, with the later two configurations each divided into a mutual approach (f_m) and an in-tandem motion (f_u). The total fluid drag balances F_{DEP} , $V_A - V_B = \frac{2F_{DEP}}{6\pi\mu_oaf_m}$. The slip is obtained by comparison of a theoretical calculation of f_m (a function of h/a , s/a , d/a and λ/a) to an experimental value calculated through the measurement of $V_A - V_B$ (or equivalently $s(t)$) and F_{DEP} .

To obtain F_{DEP} , the electric field in the mineral oil around the merging (uncharged) water droplets in the microchannel is approximated by the bispherical harmonic solution (135) for the electrostatic field in an unbounded insulating dielectric surrounding a pair of perfectly conducting spheres (zero net charge) due to a farfield electric field applied in the direction of the line of centers between the spheres, from which $F_{DEP} = \varepsilon_o\varepsilon_{oil}a^2\mathcal{E}^2\mathfrak{S}(s/a)$. $\mathfrak{S}(s/a)$ is an infinite series function of s/a evaluated here with polynomial interpolation (see Appendix B).

The coefficient f_m is calculated numerically from a COMSOL (4.2a) finite element simulation using the experimental parameters. The simulation is first verified by computing the drag coefficient for a single sphere in a plane-parallel channel moving parallel to the wall, denoted as $\alpha(d/a, \lambda/a, h/a)$, and comparing for $\lambda/a = 0$, to an interpolating formulae for α for no slip obtained from a

3. HYDRODYNAMIC SLIP AT AN OIL/POLYDIMETHYLSILOXANE SURFACE FROM MEASUREMENTS OF THE DIELECTROPHORETIC MOTION OF WATER DROPLETS

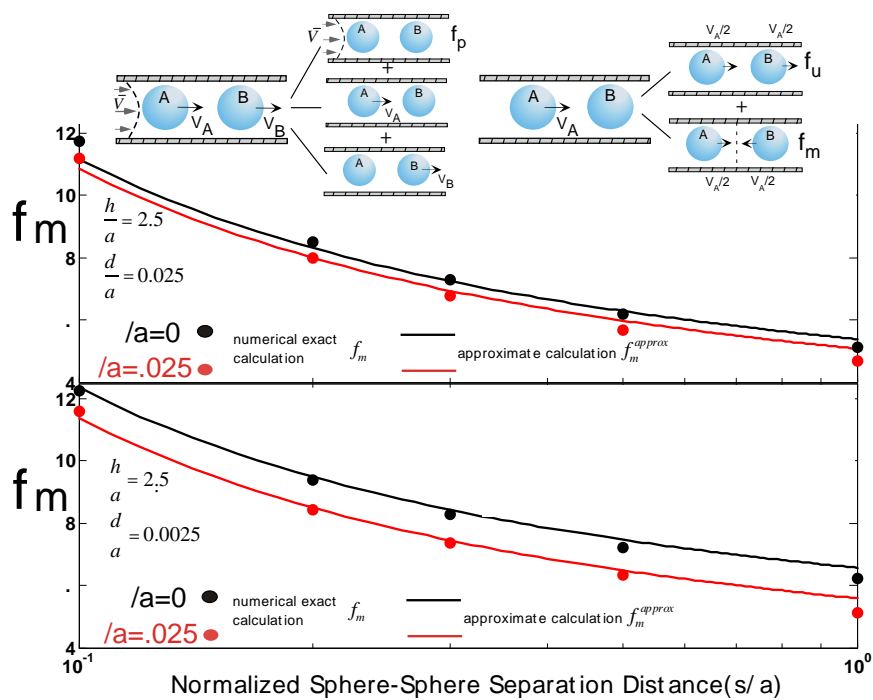


Figure 3.3: The drag coefficient f_m as a function of s/a for no-slip ($\lambda = 0$) and $\lambda = 1 \mu\text{m}$ for $d = 1 \mu\text{m}$ (top) and $d = 100 \text{ nm}$ (bottom) for $h = 100 \mu\text{m}$ and $a = 40 \mu\text{m}$.

3.1 Background

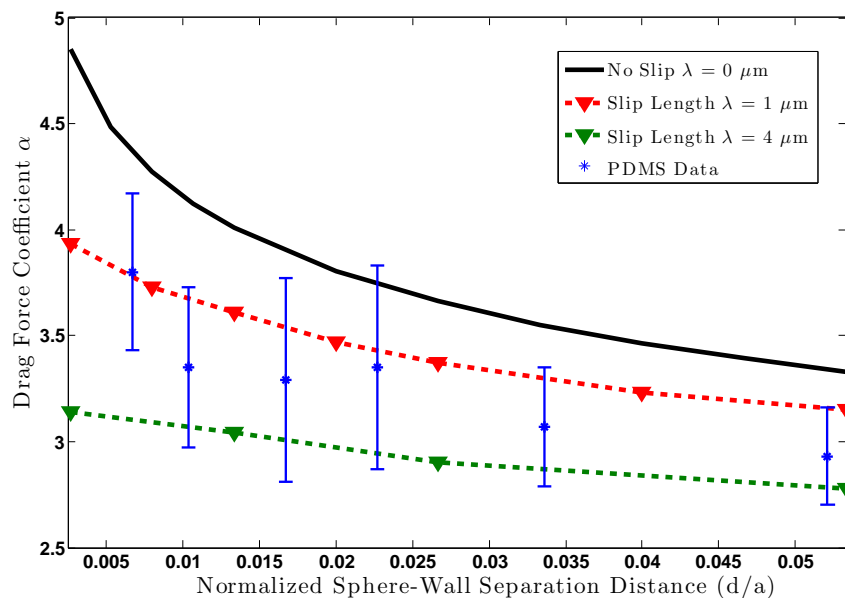
multipole solution by Feuillebois et al (1) (see Appendix B). Fig. 3.3 shows f_m (symbols) as a function of s/a for no slip and $\lambda = 1 \mu\text{m}$, for $a = 40 \mu\text{m}$ and for a separation distance $d = 1 \mu\text{m}$ (top) and 100 nm (bottom). As expected, the closer the droplet pair to the wall, the greater is the influence of the slip, and it is clear that when d of the order of a few hundred nanometers a order ten percent reduction in f_m is achieved from the no-slip case for $\lambda = 1 \mu\text{m}$, and this change is the basis of our measurement of a order one micron slip length. A slip coefficient can be obtained from the experimental profiles $s(t)$ by comparison to the integration of $\frac{ds}{dt} = V_A - V_B = \frac{2F_{DEP}}{6\pi\mu_o a f_m}$ using the numerical calculations of f_m as a function of s . We avoid this extended calculation by an approximation for f_m as the sum of the drag on a single (rigid) droplet moving at a distance d in a channel of height h with slip λ , $\alpha(d/a, \lambda/a, h/a)$ (obtained by COMSOL calculation and independent of s), the drag on a (rigid) droplet pair mutually approaching at a distance s from each other in an infinite medium, \mathcal{R} (Jeffreys solution for which there is a correlation, $\mathcal{R}(\frac{s}{a}) = \{1 + \frac{a}{2s}\} \{1 + .38e^{-\{\ln\frac{s}{a} + .68\}^2/6.3}\}$, see Appendix B) and a correction $\mathcal{D}(s/a)$:

$$f_m^{approx} = \alpha \left\{ \frac{d}{a}, \frac{\lambda}{a}, \frac{h}{a} \right\} + \mathcal{R} \left\{ \frac{s}{a} \right\} + D \left\{ \frac{s}{a} \right\} \quad (3.1)$$

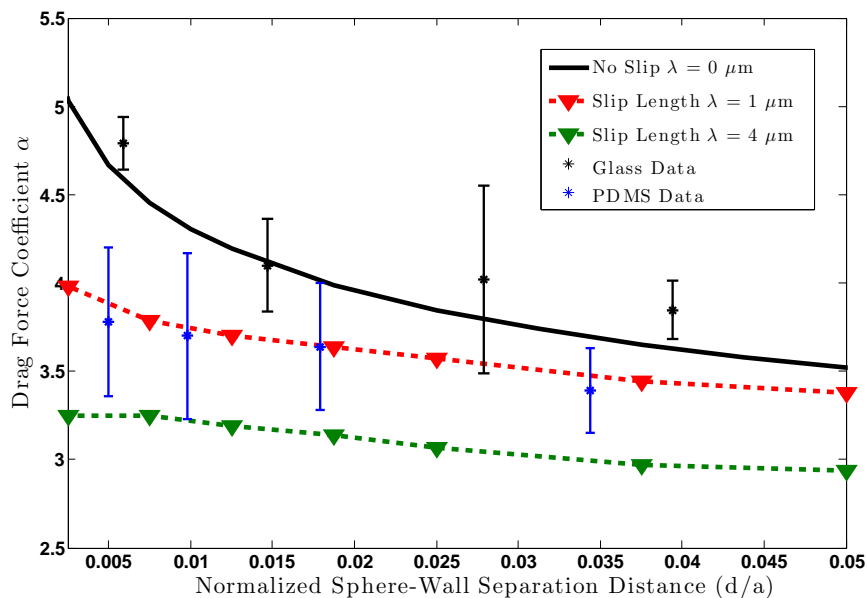
The correction factor $\mathcal{D}(s/a)$ accounts for the double counting evident in f_m^{approx} when s/a tends to infinity and should tend to -1; we use $\mathcal{D}(s/a) = -\frac{s/a}{1+s/a}$ which allows congruence of the approximate formulation over the entire range of s/a , cf. Fig. 3.3. A theoretical prediction for $s(t)$ can be constructed by integrating the force balance, using f_m^{approx} :

$$t = \int_{s_i/a}^{s/a} \frac{\alpha \left\{ \frac{d}{a}, \frac{\lambda}{a}, \frac{h}{a} \right\} + \mathcal{R} \left\{ \frac{s}{a} \right\} + D \left\{ \frac{s}{a} \right\}}{\varepsilon_o \varepsilon_{oil} \mathcal{E}^2 \mathfrak{F} \left\{ \frac{s}{a} \right\} / 3\pi\mu_{oil}} d \left\{ \frac{s}{a} \right\} \quad (3.2)$$

3. HYDRODYNAMIC SLIP AT AN OIL/POLYDIMETHYLSILOXANE SURFACE FROM MEASUREMENTS OF THE DIELECTROPHORETIC MOTION OF WATER DROPLETS



(a)



(b)

Figure 3.4: Hydrodynamic drag coefficient α as a function of separation d/a for droplets of radius $37.5 \mu\text{m}$ (a) and $40 \mu\text{m}$ (b) for fixed height $h=100 \mu\text{m}$. Symbols with error bars are the experimentally fitted coefficients, the remaining symbols are from numerical simulation (the accompanying dotted lines are a guide), and the no-slip line is from the Feuillebois et al (1) correlation.

3.1 Background

where s_i is the initial separation of the droplet pair. This prediction is easily fit to a data set by adjusting α (which is independent of s), and the fit is shown for the illustrative data in Fig. 3.2. (In practice, to include the forces on the droplets due to immediate neighbors of the train at an assumed distance s_t from the pair, we have added their dielectrophoretic dipole contribution ($\frac{24\pi}{(s_t/a+2)^4}$) to \mathfrak{S} and the leading order droplet-droplet interaction $1 + a/(2s_t)$ to \mathfrak{R} .) All data sets corresponding to different d and a are fit in this way. To correlate the fitted values of α to λ , we first bin all the data sets into groups in which in each group the radii differ by at most 3 percent. Each binned group in diameter is then further binned into wall separation distances d which differ by no more than 3 percent. The results are plotted as the symbols with error bars (from the standard deviation from the average) in Fig. 3.4 for a droplet radii bin $a=37.5\pm 1.25 \mu\text{m}$ and a bin $a=40\pm 1.25 \mu\text{m}$ as a function of the (binned) values of d/a . As each droplet radius bin corresponds to a fixed value of h/a , the theoretical value of α in these bins is only a function of d/a and λ/a . Plotted in Fig. 3.4 as symbols (for the two radii bins) are the theoretical values as a function of d/a for values of λ equal to zero (the Feuillebois correlation (1)), 1 and 4 μm (from COMSOL calculation). For the PDMS bottom channel wall, the comparison of the theoretical and experimental values of α show clearly a micron-sized slip, while for a bottom microchannel wall made of glass, no-slip is obtained as expected.

Our demonstration of $\mathcal{O}(1 \mu\text{m})$ slip at the interface of an oil and a polymeric surface (PDMS) which releases to the surface air retained in the material to form a lubricating layer, may serve as method for enabling giant slip without having to modify the surface with an air-sequestering texture. These results are particularly relevant to microfluidics where PDMS is the standard material, and the use of

3. HYDRODYNAMIC SLIP AT AN OIL/POLYDIMETHYLSILOXANE SURFACE FROM MEASUREMENTS OF THE DIELECTROPHORETIC MOTION OF WATER DROPLETS

oil streams with reagent water droplets have become a dominant lab on a chip platform.

4

Electrocoalescence of Water-in-Crude Oil Emulsions in Two Dimensions

4.1 Background

Emulsion stability is relevant to a wide range of applications, including foods, cosmetics, petroleum and other industrial processes (136, 137, 138). The fundamental issue in the understanding of emulsion stability is the interaction between droplets (or bubbles) of the dispersed phase, specifically the time required for them to approach and coalesce. This can be understood in terms of the time required to drain the continuous fluid phase from between adjacent droplets. To predict this time, knowledge of the forces between the droplets is required to make the coalescence time a well-defined hydrodynamics problem. Validation of such a prediction is most accurately realized by direct observation of individual droplet pair interactions, but this can be difficult to achieve from experiments performed on bulk emulsions.

Microfluidics offers the ability to generate emulsions of monodisperse droplets

4. ELECTROCOALESCENCE OF WATER-IN-CRUDE OIL EMULSIONS IN TWO DIMENSIONS

and observe interactions between droplets on a pairwise basis (131). Droplet separation distances can be precisely measured, enabling calculation of droplet interaction forces on a pairwise basis. The origin of these interaction forces depends on the emulsion system being studied and its application. In some instances, emulsion stability is desired, while other applications are predicated on efficient separation of the emulsified phases. In these applications, an external field is often applied to facilitate droplet coalescence and separation.

A primary example of this field-assisted separation is electrocoalescence. The importance of electrocoalescence is primarily due to its utilization in the oil industry, where it is used to separate water from crude oil in a process colloquially known as 'desalting'. Water droplets intentionally introduced into the crude oil to extract salt are subsequently removed via application of an electric field, which polarizes the conducting droplets, producing attractive (and repulsive) forces between droplets that result in coalescence of droplet pairs. Successive coalescence events between droplets produce progressively larger droplets that settle under gravity into a bulk water phase that can be easily removed. The simplest model of electrocoalescence assumes that the water droplets behave as infinitely conducting spheres in a perfectly insulating oil, and that the interfacial rheology of the water-crude oil interface plays no role in droplet coalescence. In practice, many crude oils have significant conductivity, reducing droplet polarization when the electric field is applied at 0 Hz. More importantly, crude oils contain numerous polar compounds known as asphaltenes, which adsorb at the oil-water interface and act to stabilize the droplets, inhibiting coalescence. Due to the unique nature of the asphaltene constituents in a specific crude oil, the effect of these surface-active compounds cannot be ascertained independently. A valid experimental

investigation should therefore be conducted using the crude oil under study to accurately predict electrocoalescence.

Numerous studies of various aspects of electrocoalescence have been published. Several examine the physics of the coalescence event itself (139, 140, 141). Others examine the behavior of droplet pairs initially separated by some distance. Bibette et al. measured the effect of field strength and droplet separation distance on the coalescence of microfluidically generated surfactant-stabilized water droplet pairs in hexadecane, mapping out a phase diagram which includes three regimes: coalescing, non-coalescing and partial coalescing (142). Chiesa et al. modeled the trajectory of a small droplet coalescing into a larger one as a force balance between the attractive electrostatic and resistive hydrodynamic forces, showing good agreement between experiment and theory (143). However, no current study examines electrocoalescence in two dimensions, with interactions between multiple droplets taken into account. Furthermore, all of the existing studies are performed in model systems, which are of limited applicability to water in crude oil emulsions where the heterogeneous nature of the crude oil may have a dramatic impact on electrocoalescence.

This study reports results of electrocoalescence experiments performed on two dimensional configurations of monodisperse water droplets in a crude oil. The objective was to accurately predict electrocoalescence between droplet pairs based on a calculation of the pairwise electrostatic force as determined by finite element simulations.

4. ELECTROCOALESCENCE OF WATER-IN-CRUDE OIL EMULSIONS IN TWO DIMENSIONS

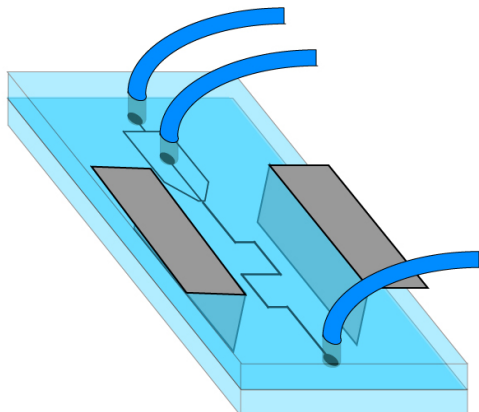


Figure 4.1: Schematic of PDMS microchannel geometry used in experiments.

4.2 Experimental Setup

To enable direct observation of water in crude oil emulsions, experiments were performed in microfluidic channels composed of PDMS. The microchannels were fabricated using standard soft lithography techniques to produce two layers of PDMS, one containing the fluidic channel and a second, flat layer to seal the channel. The two layers were bonded together following exposure to an oxygen plasma and mounted on a standard glass microscope slide. Access ports cored into the top layer using a biopsy punch allowed introduction fluids of interest via polyethylene tubing connected to syringe pumps. To generate electric fields in the microchannel, planar electrodes of aluminum were inserted into the PDMS perpendicular to the lateral plane of the microchannel and sited externally from the fluid (Figure 4.1). The electrodes were connected to an amplifier (Trek) controlled by a frequency generator (Agilent).

The first experiment demonstrated the ability to directly observe electrocoalescence of a water in crude oil emulsion in a microfluidic channel. The emulsion

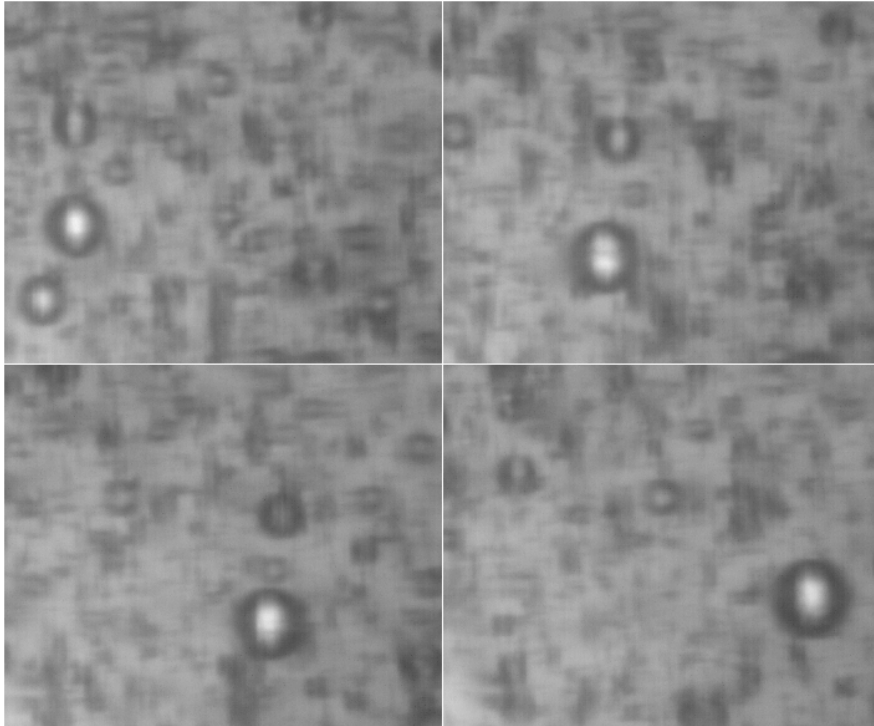


Figure 4.2: Time sequence of electrocoalescence in water-in-crude oil emulsion.

was generated by mixing water and crude oil in a prescribed volumetric ratio in a blender. The emulsion was then loaded into a glass syringe and connected to the microfluidic device, which was mounted on an inverted brightfield microscope. The emulsion was flowed through the microchannel and a uniform electric field \mathbf{E} was applied across the channel. Images of the emulsion were captured using a high-speed camera. Individual coalescence events between water droplets in crude oil were observed (Figure 4.2), as was the change in droplet size distribution of the emulsion over time, demonstrating successful observation of the electrocoalescence in crude oil.

Due to the polydisperse nature of a conventional emulsion, direct observation of the individual electrocoalescence events between droplets is of limited utility.

4. ELECTROCOALESCENCE OF WATER-IN-CRUDE OIL EMULSIONS IN TWO DIMENSIONS

Ideally, emulsion droplets should be monodisperse and have a known orientation to one another, enabling quantification of the forces between them. This is achieved by utilizing a microfluidic technique known as flow focusing. By introducing the water and crude oil phases separately and flowing them through an orifice, monodisperse droplets of water in crude can be formed. This allows the subsequent manipulation of the droplets by the electric field to be accurately modeled because both the droplet size and the separation distances between droplets are known. To generate two-dimensional configurations of droplets, the one dimensional droplet train formed immediately downstream from the flow-focusing orifice is directed into a large channel where the droplet velocities decrease and the droplets are arranged in an arbitrary configuration (Figure 4.1). The electric field is applied across the channel and the droplet coalescence events are recorded using a high-speed camera. To prevent the electrical conductivity of the crude oil from reducing the electric field over time, the electric field is applied at a frequency of 500 Hz.

4.3 Droplet Force Calculation

To predict electrocoalescence between the water droplets in the two-dimensional configuration upon application of the electric field, the electrostatic forces between the droplet pairs must be calculated. The magnitude of the applied electric field is less than that required to distort the shapes of the droplets (the electric Bond number, $Bo = \frac{\epsilon_0 \epsilon_{Oil} E^2 a}{\gamma}$, is less than one), therefore the droplets are modeled as monodisperse spheres with known diameter and position. The period of the

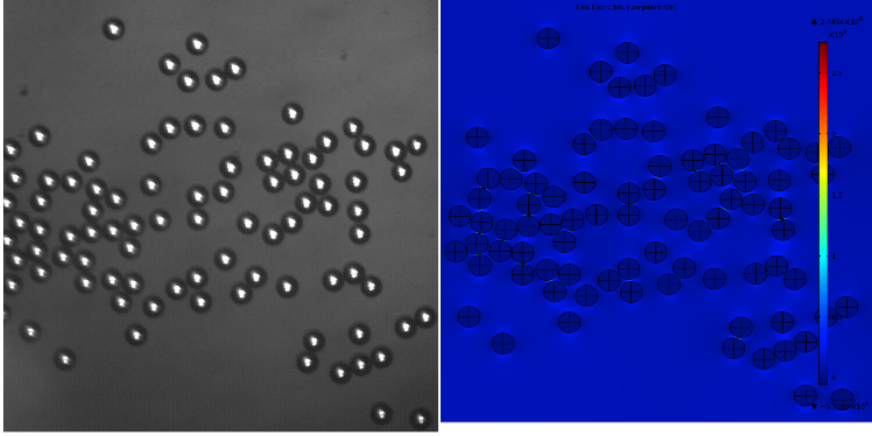


Figure 4.3: Two dimensional configuration of water droplets in crude oil with COMSOL model.

applied field is much greater than the polarization time of the droplets, $\tau = \epsilon_{H_2O}/\sigma_{H_2O}$. This produces an electric field distribution around the droplets that is quasi-static and can be calculated from the solution to the Laplace equation subject to the boundary conditions at the droplet surfaces:

$$\nabla^2 V = 0 \quad (4.1)$$

$$V_{Oil} = V_{H_2O} \quad (4.2)$$

$$\mathbf{n} \cdot (\sigma_{Oil} \mathbf{E}_{Oil} - \sigma_{H_2O} \mathbf{E}_{H_2O}) = 0 \quad (4.3)$$

Although the external field is uniform, the field around the droplets is non-uniform due to their polarization, with larger field strengths at the two poles aligned with the external field and lower field strengths at the two poles aligned perpendicular to the external field. In the case of a single droplet, the magnitudes of the field strengths at these poles will be equal, resulting in no net force on the droplet and

4. ELECTROCOALESCENCE OF WATER-IN-CRUDE OIL EMULSIONS IN TWO DIMENSIONS

therefore no motion. However, droplets in proximity to one another will experience non-symmetric local fields and will consequently experience net attractive or repulsive forces depending on their orientation relative to the external field. In the simple case of a single droplet pair, this net force has been theoretically calculated using bispherical coordinates (135). In the case of a configuration of multiple droplets, finite element simulations are used. These simulations solve the Laplace equation for each configuration of droplets to calculate the electric field \mathbf{E} around each droplet surface. This field is used to calculate the net force on each droplet.

$$\mathbf{F}_{Droplet} = \oint \mathbf{n} \cdot \mathbf{T} dA - \oint p \cdot \mathbf{n} dA \quad (4.4)$$

where \mathbf{n} is the surface normal and \mathbf{T} is the Maxwell stress tensor:

$$\mathbf{T} = \epsilon \mathbf{E} \mathbf{E} - \frac{\epsilon_0}{2} \mathbf{E}^2 \boldsymbol{\delta} \quad (4.5)$$

Applying the Maxwell equations $\nabla \cdot \epsilon \mathbf{E} = 0$ and $\nabla \times \mathbf{E} = 0$ and a vector identity simplifies the divergence of \mathbf{T} , which is equal to the pressure gradient:

$$\nabla \cdot \mathbf{T} = \frac{\epsilon - \epsilon_0}{2} \nabla |\mathbf{E}|^2 = \nabla p \quad (4.6)$$

\mathbf{E} has no tangential component, therefore $|\mathbf{E}|^2 = E_n^2$ and the net force on the droplet can be calculated:

$$\mathbf{F}_{Droplet} = \oint \frac{\epsilon}{2} E_n^2 dA \quad (4.7)$$

This net force is expected to predict the droplet motion upon application of the electric field. However, the close proximity of the droplets prior to the application of the field means that no significant motion between droplets is possible prior to coalescence. Therefore, the net force on each droplet must be deconstructed to

4.3 Droplet Force Calculation

identify the component of the force due to each adjacent droplet. In other words, the forces on the droplet must be calculated on a pairwise basis to identify which droplet pairs experience net attractive forces and are therefore likely to coalesce. This is done by simple vector projection using the net force of each droplet and the center to center vector between each droplet pair:

$$F_{pair} = \frac{|\mathbf{F}_2 - \mathbf{F}_1| \cdot |\mathbf{r}_2 - \mathbf{r}_1|}{|\mathbf{r}_2 - \mathbf{r}_1|} \quad (4.8)$$

Because each droplet only has a certain number of nearest neighbors which block its potential coalescence with other droplets, an algorithm is employed to identify which droplet pairs are not obstructed by third droplets and are therefore potentially able to coalesce. Using these calculations, the resulting pairwise droplet forces are plotted as a function of the separation distance between the droplets in the pair.

The coalescence of individual droplet pairs proceeds upon application of the external electric field. Due to the fact that the droplet configuration changes subsequent to initial coalescence events, only droplets pairs coalescing within the first 0.1 seconds, which are therefore assumed to be coalescing due to the forces calculated from the initial droplet configuration, are considered. These coalescing pairs are identified on the plot of pairwise droplet forces versus separation distance to determine if the calculated forces accurately predict coalescence. The results are shown in Figure 4.3 for a representative data set. As expected, droplet pairs with large negative (attractive) forces between them coalesce, while droplet pairs with positive (repulsive) forces between them do not coalesce. At larger separation distances, droplet pairs do not experience large forces and therefore do not coalesce due to the initial droplet configuration. As shown in Figure 4.4,

4. ELECTROCOALESCENCE OF WATER-IN-CRUDE OIL EMULSIONS IN TWO DIMENSIONS

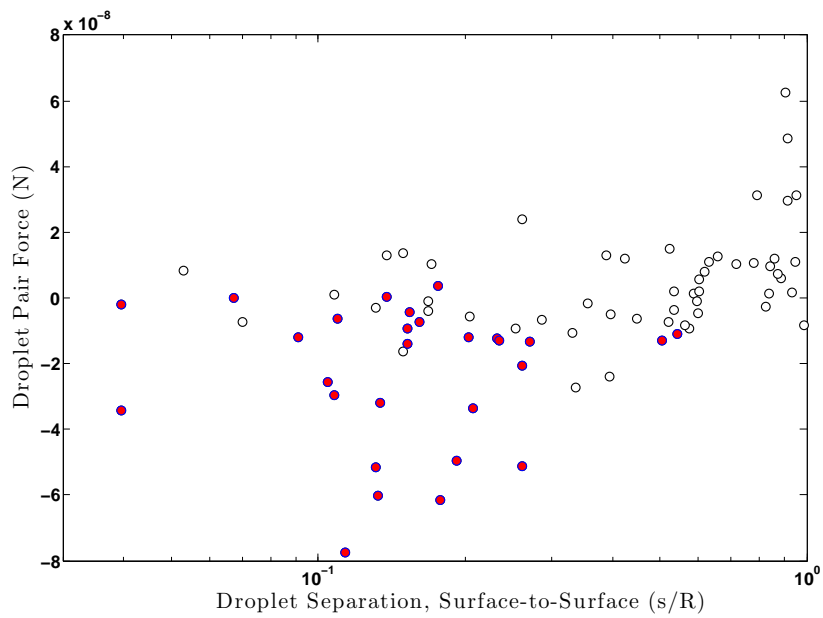


Figure 4.4: Plot of electrostatic forces between droplet pairs versus normalized separation distance.

4.3 Droplet Force Calculation

several droplet pairs with negative forces do not coalesce. This can be explained by the fact that one droplet in the pair is also half of a pair with a larger negative force, and therefore coalesces with the droplet with which it has the larger attractive force, as expected.

In conclusion, we have demonstrated accurate prediction of pairwise electro-coalescence of water droplets emulsified in a crude oil. The unique ability of microfluidic geometries to generate monodisperse emulsion droplets and observe them in a macroscopically opaque continuous phase such as crude oil should encourage further work using microfluidics to study emulsion stability.

4. ELECTROCOALESCENCE OF WATER-IN-CRUDE OIL EMULSIONS IN TWO DIMENSIONS

5

Future Work

This proposal outlines a new method of measuring the rheological properties of liquid-liquid interfaces (e.g. oil/water interfaces) with adsorbed surfactant monolayers using a microfluidic geometry via application of an electric field. Monodisperse water droplets formed in oil in a microchannel with an adsorbed monolayer at their interface are subjected to uniform, oscillating electric fields that distort their shape according to the balance between surface stresses and electrical stresses. By evaluating the change in the shape of the droplets with time, the surface tension and the surface rheological dilatational viscosity due to the surface monolayer can be measured. This technique can be used to study the surface rheology of surface active species at liquid-liquid interfaces in many applications, including protein therapeutics to understand the relationship between adsorption and aggregation. It offers significant advantages over existing measurement techniques due to its versatility in measuring interfaces between two phases of comparable densities, interfaces with an opaque continuous phase and interfaces with extremely low surface tension values. The high-throughput characteristics of microfluidic systems allow the rapid generation of high number statistics and

5. FUTURE WORK

eliminate the potential of contamination, while the small length scales provide the opportunity to study sensitive measures of the surface rheology.

5.1 Background

Our interest in the surface rheology of surfactant-laden oil-water interfaces derives from the importance of this rheology in emulsions, and also in evaluating protein interactions (as will be discussed in Proposed Research). Emulsions are dispersions of two immiscible liquids, typically water and oil, in which droplets of one liquid phase are dispersed in a continuous phase of the second liquid. Emulsions are present in many applications where they are either introduced intentionally (pharmaceuticals, foods, cosmetics) or where they occur naturally (petroleum) (136, 137, 138). The stability of the emulsion to coalescence of the droplets, and separation of the phases, is the central issue in all applications.

While a stable emulsion is desirable in some applications (drug delivery, food processing), other applications focus on breaking the emulsion to achieve a phase separation. The stability of an emulsion can be controlled by surface active components, surfactants, which are amphiphilic molecules with polar and non-polar groups. Surfactants adsorb at the liquid-liquid (e.g. oil/water) interface to form a monolayer, straddling the surface with the polar group in the water phase and the non-polar group in the oil phase (see for example the monographs (144, 145, 146, 147, 148)). Surfactant adsorption and monolayer formation change the properties of the fluid interface and thereby affect the stability of the emulsion, particularly its lifetime (i.e. how long the droplets of the emulsion remain dispersed), with dramatic impact on processing applications (149, 150, 151).

The static interface between the two fluids is characterized by the equilibrium interfacial tension, σ . When surfactants are present and adsorb at the interface, adsorption lowers the equilibrium tension from the value of the clean interface, σ_c , to a value that is a function of the surface concentration Γ of the amphiphiles at the interface, i.e. $\sigma(\Gamma)$, the surface equation of state. When the phases bounding the interface are in motion, the interface can stretch (dilate), or a shear flow can be set up in the plane of the interface. At surfactant-laden liquid-liquid interfaces in motion, the interfacial shear and dilation create stresses in the plane of the surface apart from either the interfacial tension (152, 153) or gradients in the interfacial tension due to gradients in the surface concentration of surfactant set up by the surface flow (Marangoni stresses). In the simplest description (a Newtonian surface fluid), these stresses can be related to the surface flow by surface shear (μ_s) and dilatational (κ_s) viscosity coefficients, which are functions of the surface concentration. The interfacial stress at a moving interface is therefore characterized by the equation of state, which dictates the Marangoni gradients, and the viscosity coefficients, which govern the surface rheology.

Many techniques exist to measure the equilibrium interfacial tension as a function of the bulk concentration of surfactant, and thereby the surfactant equation of state (e.g. capillary rise, Wilhelmy plate, static drop/bubble shape analysis, see for example, (154, 155, 156)). Measurement of the interfacial viscosities is more difficult, particularly the dilatational viscosity, which involves setting a dilating flow along a surface and measuring the interfacial stress (157). The standard technique for measuring the dilatational viscosity is the oscillating pendant drop technique (158, 159). This technique uses a syringe to produce a droplet (or bubble) of one phase in another and analyzes a 2D silhouette of the axisym-

5. FUTURE WORK

metric shape as a force balance between buoyancy and surface tension to obtain the surface tension. The volume of the pendant drop can be perturbed by small amounts at low frequencies to set up a dilating flow. By simultaneously measuring the tension and the area expansion rate, the surface dilatational viscosity can be obtained.

While the pendant drop technique is extremely useful, it has inherent disadvantages. The precision of the measurement is susceptible to contamination, particularly when dynamic measurements are being made over long periods of time. As the method relies on a buoyancy force between the droplet and bulk phase, it cannot be used when the two phases have comparable densities, a serious limitation in some systems. Additionally, extremely low surface tension values (< 5 mN/m) affect the stability of the droplet, making accurate measurements difficult. Perhaps most importantly, however, the pendant drop technique cannot be used when both phases are opaque to visible light.

5.2 Proposed Research

We propose to develop a microfluidic tensiometer to measure the dilatational viscosity of a liquid-liquid interface. Microfluidic systems can be used to generate and study emulsion droplets. The flow focusing technique allows the creation of highly monodisperse, surfactant-stabilized droplets and has been demonstrated in a number of applications (131, 160). These include several techniques for measuring surface rheology (161, 162). We propose to use a microfluidic flow-focusing geometry to develop an interfacial rheometer for measuring the surface dilatational viscosity by expanding and contracting water droplets in a dielectric oil

using an electric field (Figure 5.1). Trains of highly monodisperse water droplets ($d \approx 50\text{-}100 \mu\text{m}$) are dispersed in a continuous oil phase as the two phases flow through an orifice under pressure-driven flow. The droplet train enters a channel located between two externally sited, parallel electrodes. The electrodes are connected to a frequency generator and amplifier, and generate high strength ($\approx 5 \text{ kV/mm}$) electric fields to elongate the shape of the droplets, which are imaged using a high-speed camera. To eliminate the effect of the shear flow on the droplet shape, the flow can be stopped via pressure equilibration of the microchannel inlet and exit or via the incorporation of a microfluidic valve within the channel itself.

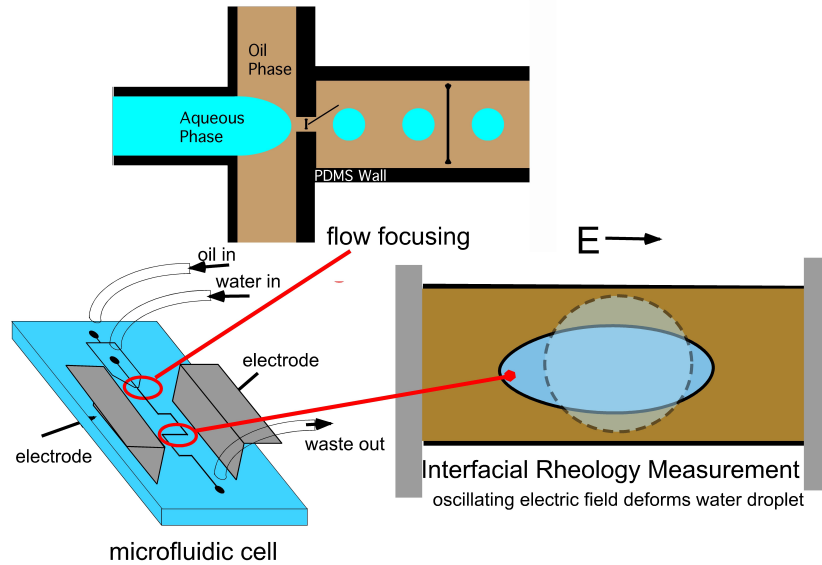


Figure 5.1: Schematic of interfacial rheometer using oscillating electric field.

The static shape of a water droplet in an oil (assumed to be a dielectric) elongated by a uniform electric field is determined by the balance between the capillary pressure $P_c = \sigma/a$ and the electric Maxwell stress $\Sigma_M = \epsilon_0 \epsilon_{oil} E^2$ ex-

5. FUTURE WORK

erted at the interface where ϵ_0 is the electrical vacuum permittivity, ϵ_{oil} is the relative permittivity of the oil, E is the magnitude of the applied field and a is the spherical radius of the droplet before deformation. The steady elongation of conducting and dielectric drops in a dielectric liquid has been studied extensively in the literature, beginning with the analysis of Taylor (163, 164, 165, 166, 167, 168, 169, 170, 171, 172). This elongation is analogous to a water droplet at a needle tip in oil which is hanging and elongated by gravity and whose shape is determined by a balance of capillary pressure and gravity as given by the Young-Laplace equation. For the case of the electric distortion, this balance is scaled by the electric Bond number, $Bo = \frac{\epsilon_0 \epsilon_{oil} E^2 a}{\sigma}$. When the surface tension is high, the droplet will maintain its spherical shape. When the surface tension is low, the electric field will distort its shape in the direction of the field.

By applying a prescribed DC electric field, the equilibrium shape of the droplet can be used to calculate the surface tension. The equation for the axisymmetric shape of the surface, which is a modified Young-Laplace equation with gravity replaced by the electrical stress, can be solved to obtain the shape as a function of Bo . This calculation is more difficult than the shape calculation in the case of gravity because the electric field on the surface must be determined in order to calculate the Maxwell stresses. This field is computed numerically by solving the Laplace equation for the electric field in the dielectric space around the drop subject to the electric field conditions on the drop surface and the imposition of a uniform field at infinity as discussed in Chapter 4. As this space is defined by the contour of the drop boundary, the calculations of the shape and the field are coupled and must be solved numerically.

We propose to use COMSOL finite element simulations to undertake these

5.2 Proposed Research

calculations, and preliminary results have been obtained (see below). By measurement of the shape through optical microscopy of the transparent microfluidic cell, and by comparison to the numerical solution, the electric Bond number Bo can be obtained. Since the magnitude of the applied electric field E is known, as is the radius a , the surface tension σ of the interface can be calculated.

To interrogate the interfacial rheology of the droplet, the electric field can be oscillated at low frequencies in a manner directly analogous to the pressure-driven oscillations of the pendant drop technique. The elongation of the droplet stretches the interface, and is resisted by the dilatational viscosity, which adds to the tension of the drop. The amplitude of oscillation must be sufficiently large to produce an observable change in droplet shape, but small enough so that the convective effects induced by the change in shape, which are proportional to the droplet size and the oscillation frequency, can be neglected. To determine the optimum electric field amplitude and frequency for a given droplet size, measurements can be performed on a clean droplet interface with a known surface tension to confirm that convective effects are not biasing the measurement (this same procedure is employed with the pendant drop apparatus).

An additional consideration is the possibility of producing of Marangoni forces due to surface concentration gradients induced by the change in droplet shape or the migration of charged surfactant due to the electric field. As in the oscillating pendant drop, the surface concentration is assumed to be sufficiently large to minimize the Marangoni effects, and the fact that the continuous oil phase is assumed to be a perfect dielectric means that charged surfactants can only be present in the droplet water phase, where the electric field is zero and therefore charge migration is not possible.

5. FUTURE WORK

Under these conditions, the static drop shape equations are valid and the net isotropic tension (γ) of the droplet can be computed from each of the oscillating shapes to obtain the oscillating tension as a function of time. From the Newtonian surface equation of state, the dilatational viscosity κ_s can be recomputed from the net tension γ and the measured area expansion $\frac{dA}{dt}$, by neglecting shear contributions for the net isotropic tension γ :

$$\gamma = \sigma(\Gamma) + \kappa_s \nabla_s \cdot \mathbf{v} = \sigma(\Gamma) + \kappa_s \frac{1}{A} \frac{dA}{dt} \quad (5.1)$$

where \mathbf{v} is the velocity of the surface.

A microfluidic system has several advantages over the pendant drop technique. The droplet interfaces are continuously generated via flow-focusing, and are therefore not subject to contamination. The force balance does not require a significant buoyancy force, allowing for investigation of liquids with comparable densities. The laminar flow regime in which the droplets are formed allows generation of droplet interfaces with extremely low surface tensions. By controlling the thickness of the microfluidic channels in which the experiment is performed, liquids that would appear opaque in larger path lengths are semi-translucent (even crude oils). Finally, the advantages inherent to all microfluidic systems, conserved analyte and high-throughput, allow for the enhanced precision of high- n statistics without increases in cost or time.

To test the model, we will study the surface rheology of emulsions of protein solutions. Proteins adsorbing at oil-water interfaces have been shown to demonstrate dilatational properties, which may correlate to aggregation behavior (173, 174, 175). For this model, we will use alpha-Chymotrypsinogen (aCgn), a commercially available and inexpensive alpha-beta protein that is known to dena-

ture and aggregate upon exposure to a hydrophobic surface. Understanding such aggregation behavior is important for the growing field of protein therapeutics, and may also enhance understanding of aggregation-mediated diseases (176, 177).

5.3 Preliminary Results

A key step in the calculation of the surface viscosity from the shapes of the water droplets in oil driven by the oscillating electric field is the computation of the shape from a modified Young-Laplace equation (with gravity replaced by the electric field stresses). This calculation is coupled to the solution of the Laplace equation for the field in the oil outside the drop subject to the field conditions on the drop surface. Figure 5.2 shows a simple example of the steady and unsteady shapes of droplets subject to a uniform electric field from a COMSOL calculation in which the interface is described through a level set formulation, and the Laplace equation for the electric field is solved by a finite element algorithm coupled to the level set formulation. The electric Bond number Bo is larger than one, causing the droplet to deform from its spherical shape to a new equilibrium shape. As the surface tension decreases from 30 mN/m to 15 mN/m, Bo increases and the deformation becomes larger.

5. FUTURE WORK

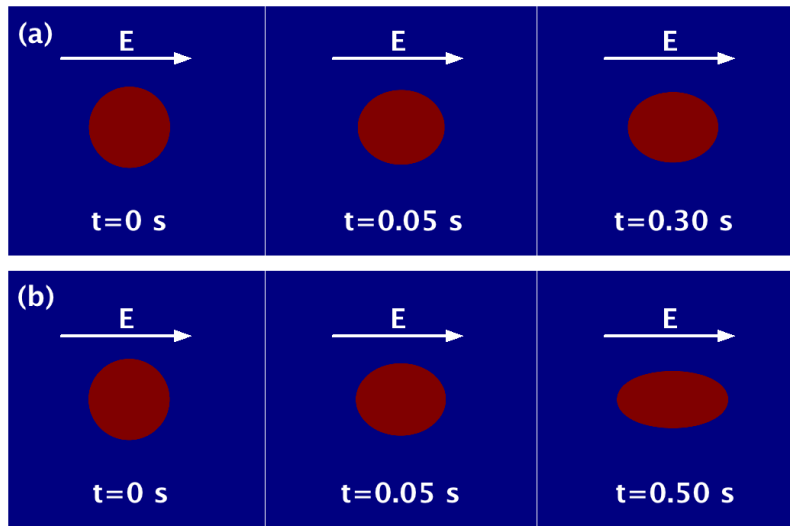


Figure 5.2: COMSOL calculation of droplet in oil subject to uniform electric field ($\epsilon_{Oil} = 2.5$, $E = 500$ V/mm, $a = 1.5$ mm). (a) $\sigma = 30$ mN/m. (b) $\sigma = 15$ mN/m. Spherical droplets deform due to the applied field to reach a non-spherical equilibrium shape. Note the longer time required for the lower tension interface to reach equilibrium.

Appendix A

The following data represent the complete set of normalized surface concentration binding curves for all parameter values used in the finite element simulations performed in Chapter 2. Kinetically limited binding curves are shown for comparison.

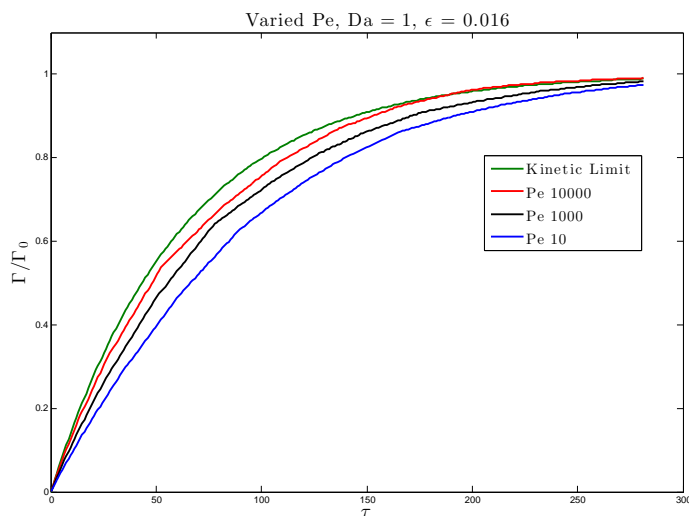


Figure A.1: Normalized binding curves showing effect of Pe at $Da = 1$

The following data represent the complete set of normalized concentration profiles for all parameter values used in the finite element simulations performed in Chapter 2.

A.

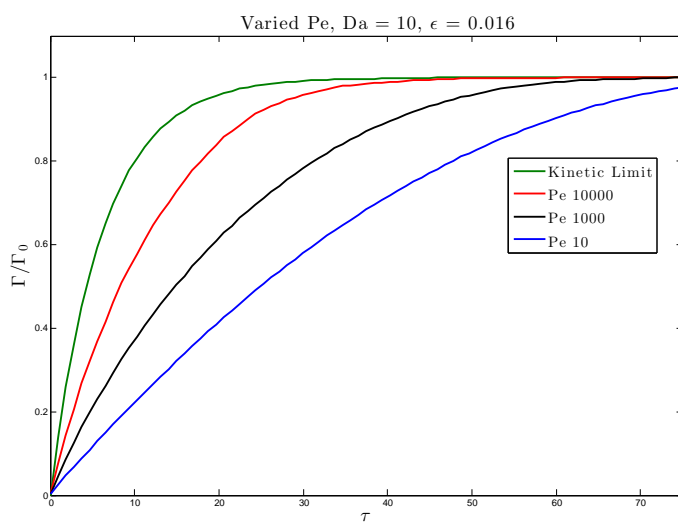


Figure A.2: Normalized binding curves showing effect of Pe at $Da = 10$

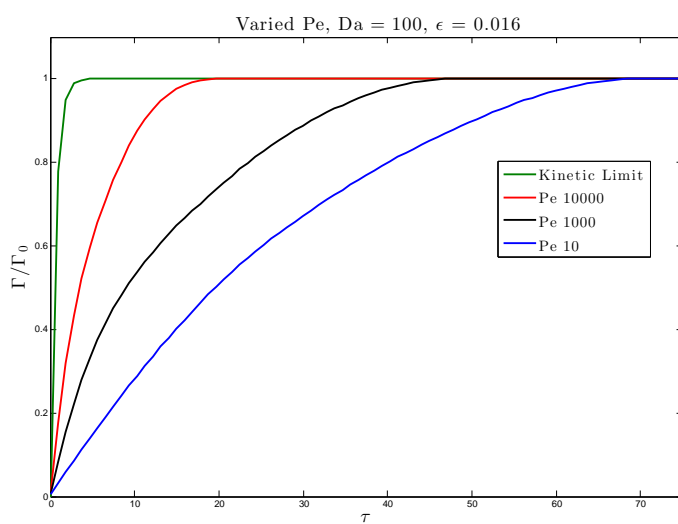


Figure A.3: Normalized binding curves showing effect of Pe at $Da = 100$

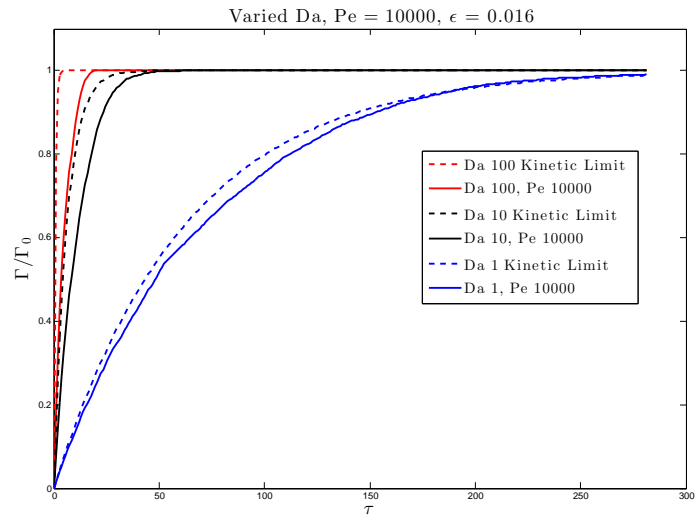


Figure A.4: Normalized binding curves showing effect of Da at $Pe = 10000$

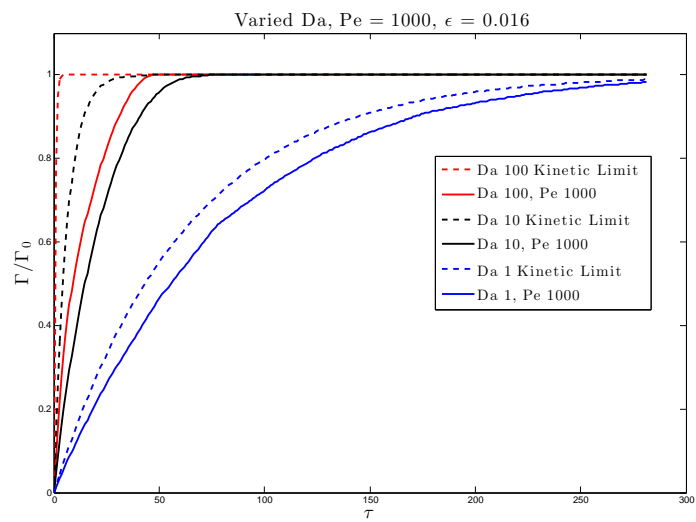


Figure A.5: Normalized binding curves showing effect of Da at $Pe = 1000$

A.

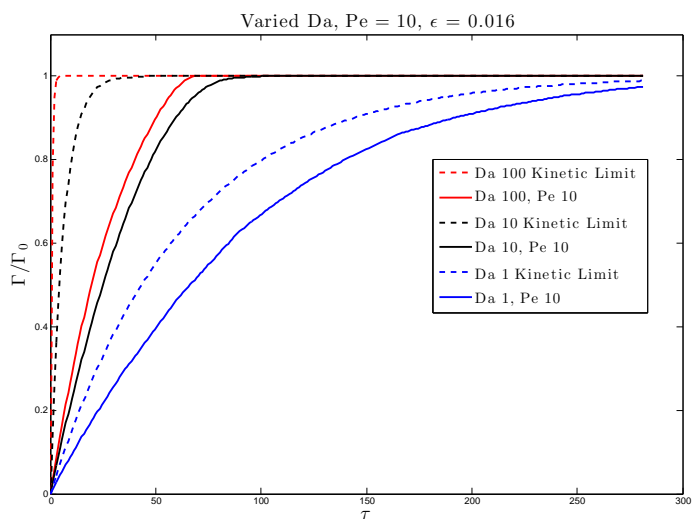


Figure A.6: Normalized binding curves showing effect of Da at $Pe = 10$



Figure A.7: Cross-section of concentration profile in microchannel for patch surface at $x = 0$, $Pe = 100$, $Da = 1$

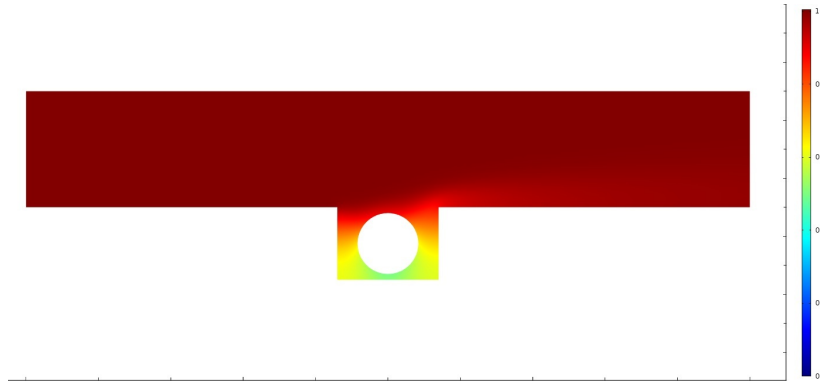


Figure A.8: Cross-section of concentration profile in microchannel for bead surface at $x = 0$, $Pe = 100$, $Da = 1$

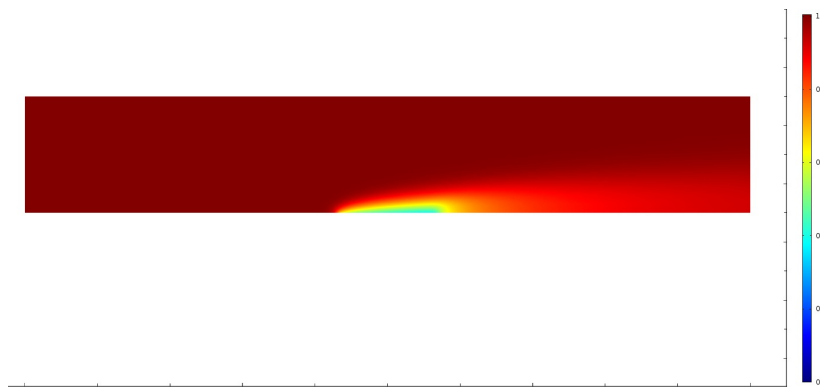


Figure A.9: Cross-section of concentration profile in microchannel for patch surface at $x = 0$, $Pe = 100$, $Da = 10$

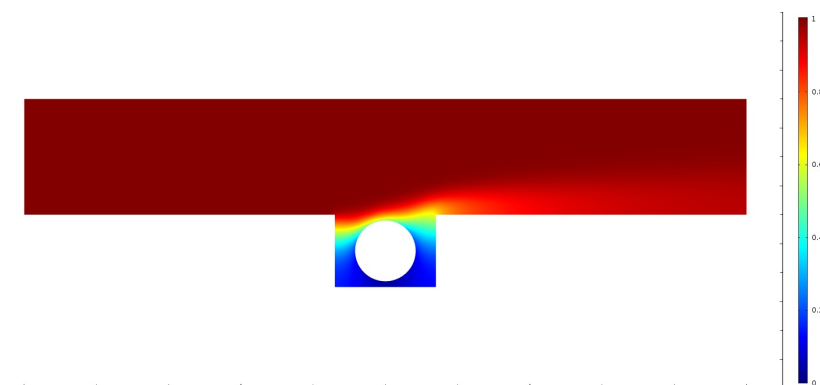


Figure A.10: Cross-section of concentration profile in microchannel for bead surface at $x = 0$, $Pe = 100$, $Da = 10$

A.

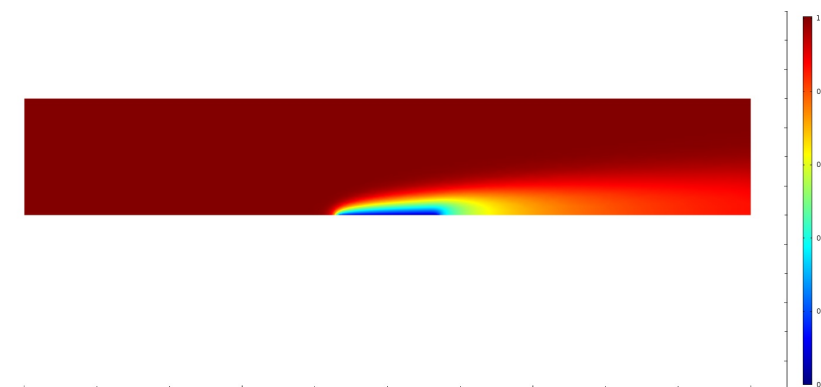


Figure A.11: Cross-section of concentration profile in microchannel for patch surface at $x = 0$, $Pe = 100$, $Da = 100$

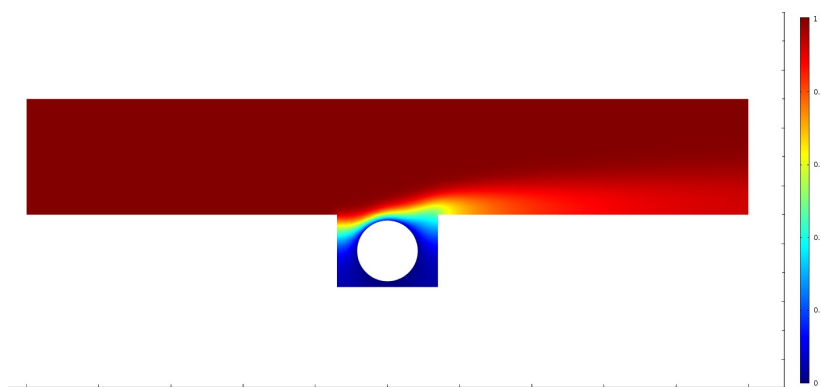


Figure A.12: Cross-section of concentration profile in microchannel for bead surface at $x = 0$, $Pe = 100$, $Da = 100$



Figure A.13: Cross-section of concentration profile in microchannel for patch surface at $x = 0$, $Pe = 1000$, $Da = 1$

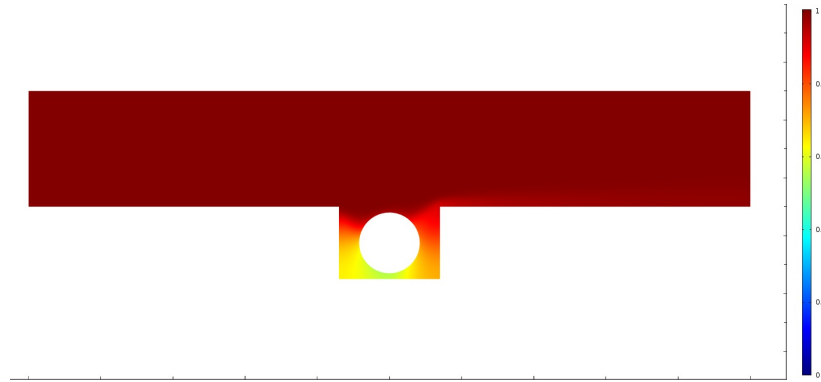


Figure A.14: Cross-section of concentration profile in microchannel for bead surface at $x = 0$, $Pe = 1000$, $Da = 1$



Figure A.15: Cross-section of concentration profile in microchannel for patch surface at $x = 0$, $Pe = 1000$, $Da = 10$

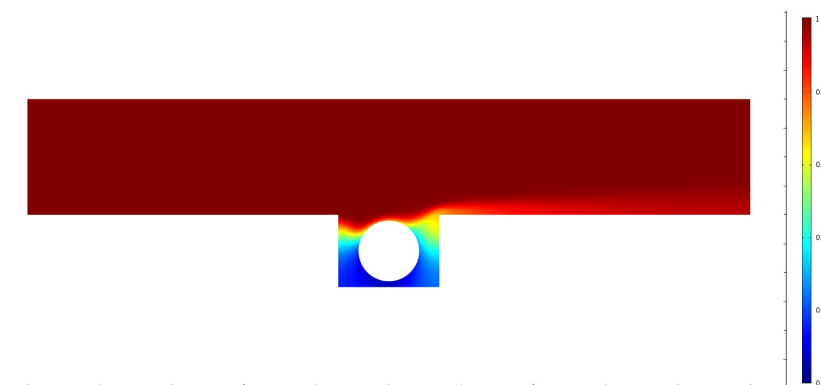


Figure A.16: Cross-section of concentration profile in microchannel for patch surface at $x = 0$, $Pe = 1000$, $Da = 10$

A.

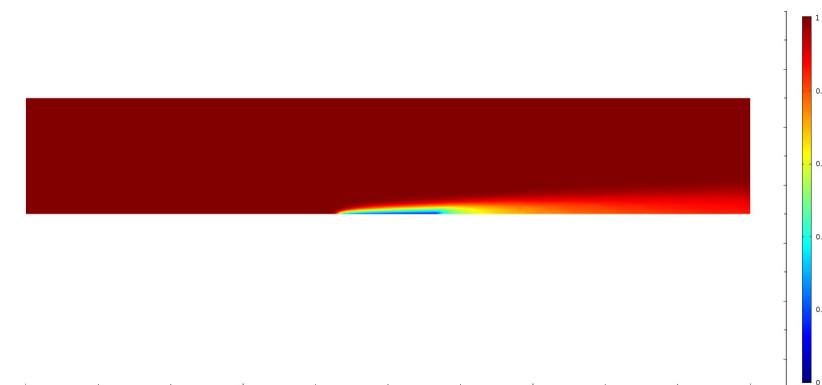


Figure A.17: Cross-section of concentration profile in microchannel for bead surface at $x = 0$, $Pe = 1000$, $Da = 10$

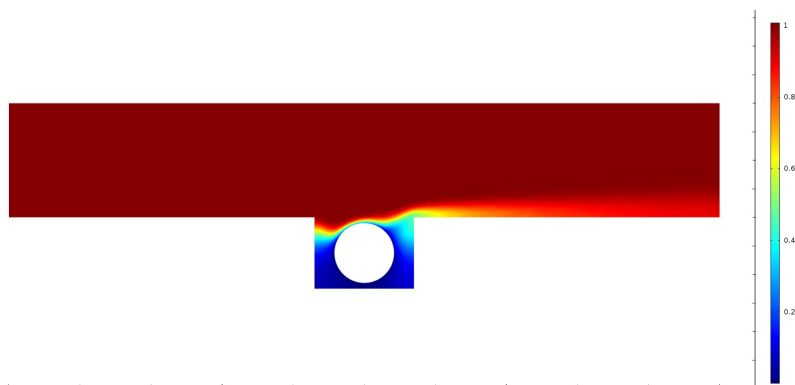


Figure A.18: Cross-section of concentration profile in microchannel for patch surface at $x = 0$, $Pe = 1000$, $Da = 100$

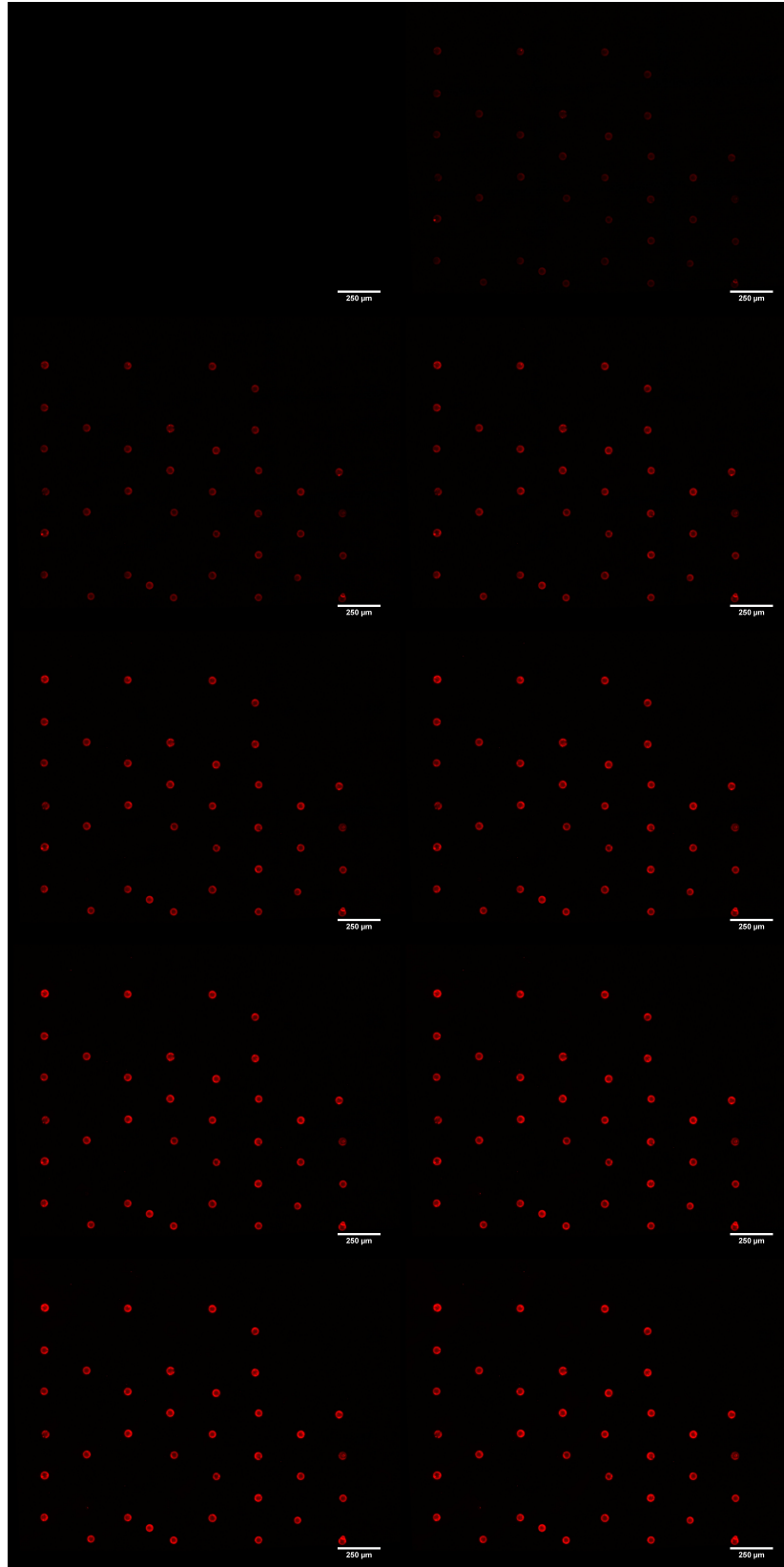


Figure A.19: Time sequence of fluorescent micrographs measuring binding of NeutrAvidin-Texas Red ($C = 4.16 \text{ E } 9 \text{ M}$) to biotin-functionalized glass microbeads ($\Gamma = 5.5 \text{ E } -9 \text{ M}$) at $Pe = 5600$.

A.

Appendix B

B.1 Materials

B.1.1 Aqueous Phase

DI Water: From Millipore ultrafiltration unit, conductivity, $18 \text{ M}\Omega \text{ cm}^{-1}$, and from handbook values $\rho_w = 10^3 \text{ kg m}^{-3}$, and $\mu_w = 10^{-3} \text{ kg m}^{-1}\text{s}^{-1}$ at $20 \text{ }^\circ\text{C}$.

Mineral Oil: Sigma-Aldrich, $\varepsilon_{oil} = 2.18$ (parallel plate capacitor measurement), $\rho_{oil} = 8.75 \times 10^2 \text{ kg m}^{-3}$ (manufacturer's data sheet) at $20 \text{ }^\circ\text{C}$. The oil viscosity μ_{oil} is temperature sensitive in the range in which the experiments were undertaken ($20\text{-}23^\circ\text{C}$), and was measured (with the surfactant, Span 80, $C=2.3 \times 10^{-2} \text{ M}$) by a temperature-controlled rheometer (see data below, Figure B.1) and fit to a correlation $\mu(T) = 2.20 \times 10^{-5}T^3 - 1.63 \times 10^{-3}T^2 + 3.58 \times 10^{-2}T - 0.139$. A thermocouple in the PDMS measured the temperature for each experiment, and in the fitting for the drag coefficient α the viscosity at the temperature measured for the experiment was used by calculation from the correlation.

B.

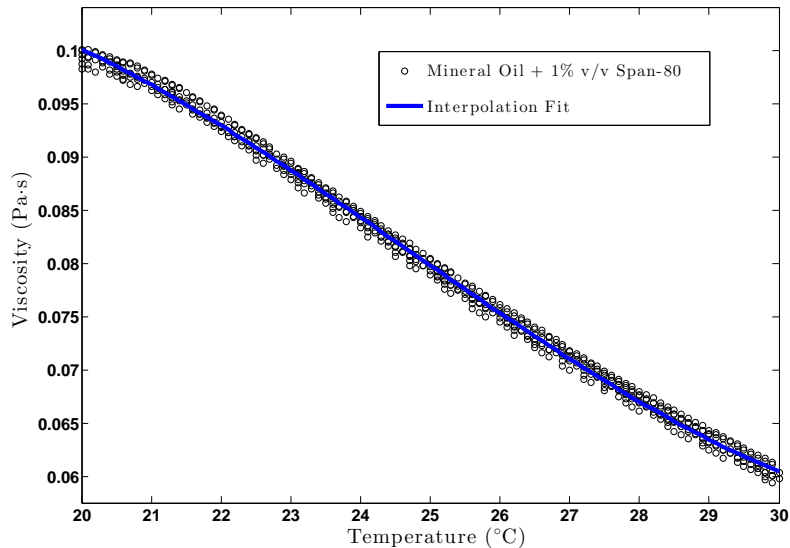


Figure B.1: Viscosity of mineral oil as a function of temperature.

B.1.2 Microfluidic Cell Fabrication

The microfluidic cell is fabricated via the methods of soft lithography (178) from two slabs of polymerized and cured PDMS, one slab containing the inscribed channels and a second, flat slab bonded to the first to enclose the channels. The PDMS prepolymer and curing agent are obtained as a kit, Sylgard 184 (Dow Corning). The top half of the cell containing the inscribed fluidic circuitry is molded from a master fabricated by photolithography using a transparency mask and a negative tone SU-8 photoresist and developer (Microchem), and the lower half is a cast layer of PDMS which is bonded to the top half by plasma treating the surfaces and then conformally contacting the halves. Dielectric constant of cured elastomer is 2.65 (manufacturer's material data sheet). Fluids are delivered to the cell from syringe pumps (Harvard PHD) via polyethylene tubing (1.5 mm

ID) through punch-hole entry ports.

B.2 Force Expressions

B.2.1 Interpolation Formula for the Electrostatic Force Between Conducting Spheres as a Function of Sphere-Sphere Separation Distance

The calculation of Davis (135) for the dielectric force on a pair of zero charge perfectly conducting spheres in an unbounded insulating dielectric subject to a uniform electric field \mathcal{E} at infinity applied along the line of centers of the spheres is given as an infinite series solution of the edge-to-edge separation distance s divided by a , from which the dielectrophoretic force between the spheres is obtained as $F_{DEP} = \varepsilon_o \varepsilon_{oil} \mathcal{E}^2 a^2 \mathfrak{S}(s/a)$ where $\mathfrak{S}(s/a)$ is an infinite series. We approximate the series by the polynomial $\mathfrak{S}(s/a) = -2.02 \times 10^{-7} (s/a)^3 + 7.33 \times 10^{-7} (s/a)^2 - 9.99 \times 10^{-7} (s/a)$ and a comparison of this interpolation formulae and the Davis expression is given in Figure B.2.

B.2.2 Analytical Solution for the Hydrodynamic Drag Force Due to Approaching Spheres as a Function of Sphere-Sphere Separation Distance in an Infinite Medium, $\mathcal{R}(s/a)$

The solution for the hydrodynamic drag exerted on a pair of two mutually approaching (interfacially rigid or solid) spheres in an infinite medium is the Stimson and Jeffrey solution in bispherical coordinates and is expressed as an infinite series and the drag coefficient $\mathcal{R}(s/a)$ is expressed as an infinite series (see eq. B.1);

B.

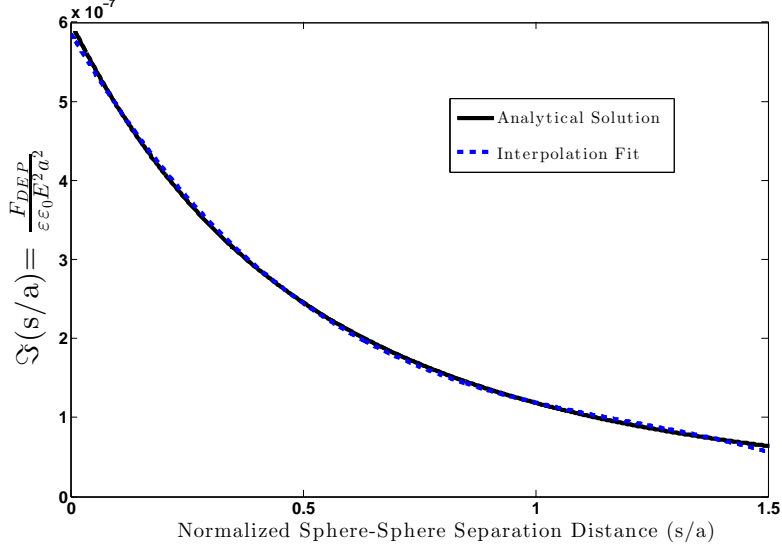


Figure B.2: Normalized electrostatic force as a function of normalized separation distance as given by the exact bispherical calculation and the interpolating equation.

for numerical calculation we use the interpolation as given by Ivanov et al (179)

and written in the manuscript.

$$\mathcal{R}(s/a) = \sinh \epsilon \sum_{n=1}^{\infty} \frac{n(n+1)}{\Delta_n} \left\{ \frac{\lambda_n \exp(2\epsilon)}{2\lambda_{n-1}} + \frac{\lambda_n \exp(-2\epsilon)}{2\lambda_{n+1}} + \frac{\exp(-2\epsilon\lambda_n)}{\lambda_{n-1}\lambda_{n+1}} - 1 \right\}$$

$$\cosh \epsilon = 1 + \frac{s}{2a}, \lambda_n = n + \frac{1}{2}, \Delta_n = \sinh(2\lambda_n\epsilon) - \lambda_n \sin(2\epsilon)$$
(B.1)

B.2.3 Hydrodynamic Drag Force on a Single Sphere Translating Between and Parallel to Two Parallel Walls

Detailed multipole solutions for the drag coefficient for a single solid sphere translating parallel and between two parallel walls was given by Feuillebois et al, as cited in the manuscript. They construct an interpolating formulae (eq. 29) for this drag coefficient, and in Figure B.3 we compare the results of this correlation with our COMSOL results as a means of validating our numerical simulations.

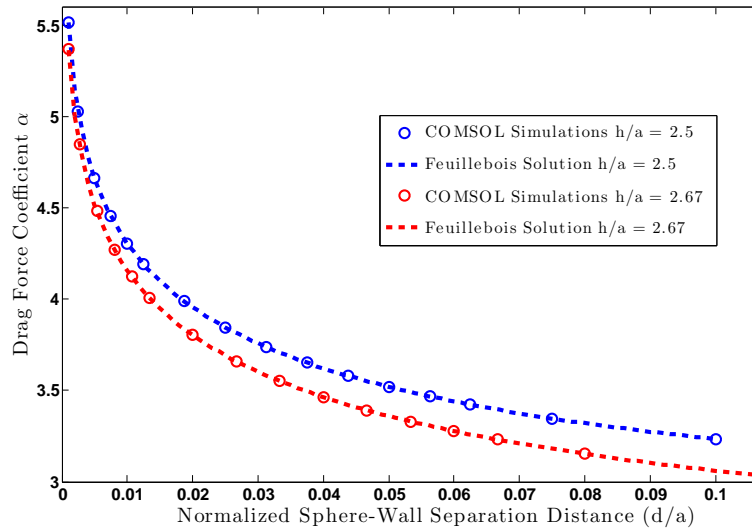


Figure B.3: Hydrodynamic drag force on a single sphere translating between two parallel walls for no slip, $\lambda = 0 \mu\text{m}$ as a function of the sphere/wall separation distance d (edge-to-edge), comparing the Feuillebois correlation and our COMSOL calculation for two values of the channel height h relative to the sphere radius a .

B.

References

- [1] L. PASOL, M. MARTIN, M. L. EKIEL-JEZEWSKA, E. WAJNRYB, J. BLAWDZIEWICZ, AND F. FEUILLEBOIS. **Motion of a sphere parallel to plane walls in a Poiseuille flow. Application to field-flow fractionation and hydrodynamic chromatography.** *Chemical Engineering Science*, **66**(18):4078–4089, 2011. vii, 57, 58, 59
- [2] D. DUFFY, J. McDONALD, O. SCHUELLER, AND G. WHITESIDES. **Rapid Prototyping of Microfluidic System in Poly(dimethylsiloxane).** *Anal. Chem.*, **70**:4974–4984, 1998. 3
- [3] E. ENGVALL AND P. PERLMANN. **Enzyme-linked immunosorbent assay (ELISA). Quantitative assay of immunoglobulin-g.** *Immunochemistry*, **8**(9):871–874, 1971. 14
- [4] J.R. CROWTHER. *The ELISA Guidebook*. Humana Press, Totowa, NJ, 2001. 14
- [5] S. SACHETELLI, C. BEAULAC, AND J. LAGACE. **Aminoglycoside detection using a universal ELISA binding procedure onto polystyrene microtiter plates in comparison with HPLC analysis and microbiological agar-diffusion assay.** *Biochimica Et Biophysica Acta-General Subjects*, **1379**(1):35–41, 1998. 14
- [6] GERALD WALTER, KONRAD BASSOW, DOLORES CAHILL, ANGELIKA LUEKING, AND HANS LEHRACH. **Protein arrays for gene expression and molecular interaction screening.** *Current Opinion in Microbiology*, (3):298–302, 2000. 15
- [7] D. CAHILL. **Protein and antibody arrays and their medical applications.** *Journal of Immunological Methods*, **250**:81–91, 2001. 15
- [8] HENG ZHU AND MICHAEL SNYDER. **Protein arrays and microarrays.** *Current Opinion in Chemical Biology*, **5**(1):40 – 45, 2001. 15
- [9] T. KODADEK. **Protein microarrays: prospects and problems.** *Chem Biology*, **8**(2):105–115, 2001. 15
- [10] DAVID S WILSON AND STEFFEN NOCK. **Functional protein microarrays.** *Current Opinion in Chemical Biology*, **6**(1):81 – 85, 2002. 15
- [11] S. LAL, R. CHRISTOPHERSON, AND C. DOS REMEDIOS. **Antibody Arrays: An Embryonic But Rapidly Growing Technology.** *DDT*, **7**:S143–S149, 2002. 15
- [12] HENG ZHU AND MICHAEL SNYDER. **Protein chip technology.** *Current Opinion in Chemical Biology*, **7**(1):55 – 63, 2003. 15
- [13] M. SCHENA. *Microarray Analysis*. John Wiley and Sons, Inc., 2003. 15
- [14] D. YEO, R. PANICKER, L. TAN, AND S. YAO. **Strategies for Immobilization of Biomolecules in a Microarray.** *Combinatorial Chemistry and High Throughput Screening*, **7**:213–221, 2004. 15
- [15] P. PREDKI. **Functional Protein Microarrays: Ripe for Discovery.** *Current Opinion in Chemical Biology*, **8**:8–13, 2004. 15
- [16] JOSHUA LABAER AND NIROSHAN RAMACHANDRAN. **Protein microarrays as tools for functional proteomics.** *Current Opinion in Chemical Biology*, **9**(1):14 – 19, 2005. [jce:title;Proteomics and genomics;ce:title](#). 15
- [17] CLAUS HULTSCHIG, JÜRGEN KREUTZBERGER, HARALD SEITZ, ZOLTÁN KONTHUR, KONRAD BÜSSOW, AND HANS LEHRACH. **Recent advances of protein microarrays.** *Current Opinion in Chemical Biology*, **10**(1):4 – 10, 2006. [jce:title;Proteomics and genomics;ce:title](#). 15
- [18] C. LAFRATTA AND D.R. WALT. **Very High Density Sensing Arrays.** *Chemical Reviews*, **108**:614–637, 2008. 15
- [19] R. WELLHAUSEN AND H. SEITZ. **Facing Current Quantification Challenges in Protein Microarrays.** *Journal of Biomedicine and Biotechnology*, **2012**:831347, 2012. 15
- [20] L. MENDOZA, P. MCQUARY, A. MONGAN, R. GANGADHARAN, S. BRIGNAC, AND M. EGGERS. **High Throughput Microarray Based Enzyme Linked Immunoassorbant Assay (ELISA).** *Biotechniques*, **27**:778–788, 1999. 15
- [21] B. D. MARTIN, B. P. GABER, C. H. PATTERSON, AND D. C. TURNER. **Direct protein microarray fabrication using a hydrogel "stamper".** *Langmuir*, **14**(15):3971–3975, 1998. 15
- [22] K. LEE, S. PARK, C. MIRKIN, J. SMITH, AND M. MRKSICH. **Protein Nanoarrays Generated by Dip Pen Nanolithography.** *Science*, **295**(1702-1705), 2002. 16
- [23] KB LEE, JH LIM, AND CA MIRKIN. **Protein nanostructures formed via direct-write dip-pen nanolithography.** *Journal of the American Chemical Society*, **125**(19):5588–5589, 2003. 16
- [24] JA STEINKAMP, JS WILSON, GC SAUNDERS, AND CC STEWART. **Phagocytosis - flow cytometric quantitation with fluorescent microspheres.** *Science*, **215**(4528):64–66, 1982. 17
- [25] JM LABUS AND BH PETERSEN. **Quantitation of human anti-mouse antibody in serum by flow-cytometry.** *Cytometry*, **13**(3):275–281, 1992. 17
- [26] TM MCHUGH, MK VIELE, AND ES CHASE. **The sensitive detection and quantitation of antibody to HCV by using a microsphere-based immunoassay and flow cytometry.** *Cytometry*, **29**(2):106–112, 1997. 17

REFERENCES

- [27] KA DROUVALAKIS, P.J. NEESON, AND R.R. BUCHANAN. **Detection of anti-phosphatidylethanolamine antibodies using flow cytometry.** *Cytometry*, **36**(1):46–51, 1999. 17
- [28] DARIO VIGNALI. **Multiplexed particle-based flow cytometric assays.** *Journal of Immunological Methods*, **243**(1-2):243–255, 2000. 17
- [29] **Luminex xMAP Technology**, 2013. 17
- [30] B.J. BATTERSBY, G. LAWRIE, A. JOHNSTON, AND M. TRAU. **Optical barcoding of Colloidal Suspensions: Applications in Genomics, Proteomics and Drug Discovery.** *Chem. Communication*, **14**:1435–1441, 2002. 17
- [31] E. VERPOORTE. **Beads and Chips: New Recipes for Analysis.** *Lab on a Chip*, **3**:60N–68N, 2003. 18
- [32] C.T. LIM AND Y. ZHANG. **Bead-Based Microfluidic Immunoassays: The Next Generation.** *Biosensors and Bioelectronics*, **22**:1197–1204, 2007. 18
- [33] S. DERVEAUX, B. STUBBE, K. BRAECKMANS, C. ROELANT, K. SATO, J. DEMEESTER, AND S.C. DE SMEDT. **Synergism Between Particle-Based Multiplexing and Microfluidics Technologies May Bring Diagnostics Closer to the Patient.** *Analytical and Bioanalytical Chemistry*, **391**:2453–2467, 2008. 18
- [34] D. MARK, S. HAEBERLE, G. ROTH, F. VON SETTEN, AND R. ZENGERLE. **Microfluidic lab-on-a-chip platforms: requirements, characteristics and applications.** *Chemical Society Reviews*, **39**:1153–1182, 2010. 18
- [35] HELENE ANDERSSON, CHRISTINA JÖNSSON, CHRISTINA MOBERG, AND GÖRAN STEMME. **Patterned self-assembled beads in silicon channels.** *ELECTROPHORESIS*, **22**(18):3876–3882, 2001. 18
- [36] H. ANDERSSON, J. JONSSON, C. MOBERG, AND G. STEMMEN. **Self-assembled and self-sorted array of chemically active beads for analytical and biochemical screening.** *Talanta*, **59**:301–308, 2002. 18
- [37] M. NOLTE AND A. FERY. **Coupling of Individual Polyelectrolyte Capsules Onto Patterned Substrates.** *Langmuir*, **20**:2995–2998, 2004. 18
- [38] V. SIVAGNANAM, A. SAYAH, C. VANDEVYVER, AND M. A. M. GLIS. **Micropatterning of protein-functionalized magnetic beads on glass using electrostatic self-assembly.** *Sensors and Actuators B: Chemical*, **132**(2):361–367, 2008. 18
- [39] Y. MOSER, T. LEHNERT, AND M. A. M. GLIS. **On-chip immuno-agglutination assay with analyte capture by dynamic manipulation of superparamagnetic beads.** *Lab on a Chip*, **9**(22):3261–3267, 2009. 18
- [40] P. STEVENS AND D. KELSO. **Imaging and Analysis of Immobilized Particle Arrays.** *Analytical Chem.*, **75**:1147–1154, 2003. 18
- [41] P. STEVENS, C. WANG, AND D. KELSO. **Immobilized Particle Arrays: Coalescence of Planar- and Suspension Array Technologies.** *Analytical Chem.*, **75**:1141–1146, 2003. 18
- [42] N.D. KALYANKAR, M.K. SHARMA, S.V. VAIDYA, D. CALHOUN, C. MALDARELLI, A. COUZIS, AND L. GILCHRIST. **Arraying of Intact Liposomes into Chemically Functionalized Microwells.** *Langmuir*, **22**(12):5403–5411, 2006. 18
- [43] J. LEE, O. KIM, J. JUNG, K. NA, P. HO, AND J. HYUN. **Simple Fabrication of a Smart Microarray of Polystyrene Microbeads for Immunoassay.** *Colloids and Surfaces B: Biointerfaces*, **72**:173–180, 2009. 18
- [44] A. WINKLEMAN, B. D. GATES, L. S. MCCARTY, AND G. M. WHITESIDES. **Directed Self-Assembly of Spherical Particles on Patterned Electrodes by an Applied Electric Field.** *Advanced Materials*, **17**(12):1507–1511, 2005. 18
- [45] LUISA FILIPPONI, PRASHANT D. SAWANT, FLORIN FULGA, AND DAN V. NICOLAU. **Microbeads on microposts: An inverted architecture for bead microarrays.** *Biosensors and Bioelectronics*, **24**:1850–1857, 2009. 18
- [46] D. WALT. **Fibre Optic Microarrays.** *Chemical Society Reviews*, **39**:38–50, 2010. 18
- [47] X. QIU, J. THOMPSON, Z. CHEN, C. LIU, D. CHEN, S. RAMPRASAD, M. MAUK, S. ONGAGNA, C. BARBER, A. ABRAMS, D. MALAMUD, P. CORSTJENS, AND H.H. BAU. **Finger Actuated, Self-contained Immunoassay Cassettes.** *Biomedical Microdevices*, **11**:1175–1186, 2009. 18
- [48] J. THOMPSON, X. DU, J. GROGAN, M. SCHRLAU, AND H. BAU. **Polymeric Microbead Arrays For Microfluidic Applications.** *Journal of Micromechanics and Microengineering*, **29**:115017, 2010. 18
- [49] JASON A. THOMPSON AND HAIM H. BAU. **Microfluidic, bead-based assay: Theory and experiments.** *Journal of Chromatography B*, **878**(2):228 – 236, 2010. 18
- [50] CHEUK W. KAN, ANDREW J. RIVNAK, TODD G. CAMPBELL, TOMASZ PIECH, DAVID M. RISSIN, MATTHIAS MOSL, ANDREJ PETERCA, HANS-PETER NIEDERBERGER, KAITLIN A. MINNEHAN, PURVISH P. PATEL, EVAN P. FERRELL, RAYMOND E. MEYER, LEI CHANG, DAVID H. WILSON, DAVID R. FOURNIER, AND DAVID C. DUFFY. **Isolation and detection of single molecules on paramagnetic beads using sequential fluid flows in microfabricated polymer array assemblies.** *Lab on a Chip*, **12**(5):977–985, 2012. 19
- [51] W. HAMPTON HENLEY, P. DENNIS, AND J. MICHAEL RAMSEY. **Fabrication of Microfluidic Devices Containing Patterned Microwell Arrays.** *Analytical Chemistry*, **84**:1776–1780, 2012. 19
- [52] K. BARBEE AND X. HUANG. **Magnetic Assembly of High-Density DNA Arrays for Genomic Analysis.** *Analytical Chemistry*, **80**:2149–2154, 2008. 20
- [53] KRISTOPHER D. BARBEE, ALEXANDER P. HSIAO, MICHAEL J. HELLER, AND XIAOHUA HUANG. **Electric field directed assembly of high-density microbead arrays.** *Lab on a Chip*, **9**(22):3268–3274, 2009. 20

REFERENCES

- [54] KRISTOPHER D. BARBEE, ALEXANDER P. HSIAO, ERIC E. ROLLER, AND XIAOHUA HUANG. **Multiplexed protein detection using antibody-conjugated microbead arrays in a microfabricated electrophoretic device.** *Lab on a Chip*, **10**(22):3084–3093, 2010. 20
- [55] ADRIAN GOODEY, JOHN J. LAVIGNE, STEVE M. SAVOY, MARC D. RODRIGUEZ, THEODORE CUREY, ANDREW TSAO, GLEN SIMMONS, JOHN WRIGHT, SEUNG-JIN YOO, YOUNGSOO SOHN, ERIC V. ANSLYN, JASON B. SHEAR, DEAN P. NEIKIRK, AND JOHN T. MCDEVITT. **Development of Multianalyte Sensor Arrays Composed of Chemically Derivatized Polymeric Microspheres Localized in Micromachined Cavities.** *Journal of the American Chemical Society*, **123**(11):2559–2570, 2001. 20
- [56] NICK CHRISTODOULIDES, MAIYEN TRAN, PIERRE N. FLORIANO, MARC RODRIGUEZ, ADRIAN GOODEY, MEHNAAZ ALI, DEAN NEIKIRK, AND JOHN T. MCDEVITT. **A Microchip-Based Multianalyte Assay System for the Assessment of Cardiac Risk.** *Analytical Chemistry*, **74**(13):3030–3036, 2002. 20
- [57] MEHNAAZ F. ALI, ROMY KIRBY, ADRIAN P. GOODEY, MARC D. RODRIGUEZ, ANDREW D. ELLINGTON, DEAN P. NEIKIRK, AND JOHN T. MCDEVITT. **DNA Hybridization and Discrimination of Single-Nucleotide Mismatches Using Chip-Based Microbead Arrays.** *Analytical Chemistry*, **75**(18):4732–4739, 2003. 20
- [58] ROMY KIRBY, EUN JEONG CHO, BRIAN GEHRKE, TRAVIS BAYER, YOON SOK PARK, DEAN P. NEIKIRK, JOHN T. MCDEVITT, AND ANDREW D. ELLINGTON. **Aptamer-Based Sensor Arrays for the Detection and Quantitation of Proteins.** *Analytical Chemistry*, **76**(14):4066–4075, 2004. 20
- [59] NICOLAOS CHRISTODOULIDES, SANGHAMITRA MOHANTY, CRAIG S. MILLER, M. CHRIS LANGUB, PIERRE N. FLORIANO, PRIYA DHARSHAN, MEHNAAZ F. ALI, BRUCE BERNARD, DWIGHT ROMANOVICZ, ERIC ANSLYN, PHILIP C. FOX, AND JOHN T. MCDEVITT. **Application of microchip assay system for the measurement of C-reactive protein in human saliva.** *Lab on a Chip*, **5**(3):261–269, 2005. 20
- [60] SHIFENG LI, PIERRE N. FLORIANO, NICOLAOS CHRISTODOULIDES, DAVID Y. FOZDAR, DONGBING SHAO, MEHNAAZ F. ALI, PRIYA DHARSHAN, SANGHAMITRA MOHANTY, DEAN NEIKIRK, JOHN T. MCDEVITT, AND SHAOCHEN CHEN. **Disposable polydimethylsiloxane/silicon hybrid chips for protein detection.** *Biosensors and Bioelectronics*, **21**(4):574–580, 2005. 20
- [61] YOUNG-SOO SOHN, ADRIAN GOODEY, ERIC V. ANSLYN, JOHN T. MCDEVITT, JASON B. SHEAR, AND DEAN P. NEIKIRK. **A microbead array chemical sensor using capillary-based sample introduction: toward the development of an electronic tongue.** *Biosensors and Bioelectronics*, **21**(2):303–312, 2005. 20
- [62] JESSE V. JOKERST, ARCHANA RAAMANATHAN, NICOLAOS CHRISTODOULIDES, PIERRE N. FLORIANO, AMANDA A. POLLARD, GLENNON W. SIMMONS, JORGE WONG, CAROLE GAGE, WIESLAW B. FURMAGA, SPENCER W. REDDING, AND JOHN T. MCDEVITT. **Nano-bio-chips for high performance multiplexed protein detection: Determinations of cancer biomarkers in serum and saliva using quantum dot bioconjugate labels.** *Biosensors and Bioelectronics*, **24**(12):3622–3629, 2009. 20
- [63] JESSE V. JOKERST, JAMES W. JACOBSON, BRYON D. BHAGWANDIN, PIERRE N. FLORIANO, NICOLAOS CHRISTODOULIDES, AND JOHN T. MCDEVITT. **Programmable Nano-Bio-Chip Sensors: Analytical Meets Clinical.** *Analytical Chemistry*, **82**(5):1571–1579, 2010. 20
- [64] NAN DU, JIE CHOU, ELIONA KULLA, PIERRE N. FLORIANO, NICOLAOS CHRISTODOULIDES, AND JOHN T. MCDEVITT. **A disposable bio-nano-chip using agarose beads for high performance immunoassays.** *Biosensors and Bioelectronics*, **28**(1):251–256, 2011. 20
- [65] W. XU, K. SUR, H. ZENG, A. FEINERMAN, D. KELSO, AND J. KETTERSON. **A Microfluidic Approach to Assembling Ordered Microsphere Arrays.** *Journal of Micromechanics and Microengineering*, **18**:075027, 2008. 20
- [66] ANDREA LIONELLO, JACQUES JOSSERAND, HENRIK JENSEN, AND HUBERT H. GIRAULT. **Dynamic Protein Adsorption in Microchannels By Stop-Flow and Continuous Flow.** *Lab on a Chip*, **5**:1096–1103, 2005. 20, 24
- [67] MARTIN ZIMMERMANN, EMMANUEL DELAMARCHE, MARC WOLF, AND PATRICK HUNZIKER. **Modeling and Optimization of High-Sensitivity, Low-Volume Microfluidic-Based Surface Immunoassays.** *Biomedical Microdevices*, **7**(2):99–110, 2005. 20, 24
- [68] T. SQUIRES, R. MESSINGER, AND S. MANNALIS. **Making It Stick: Convection, Reaction and Diffusion in Surface-Based Biosensors.** *Nature Biotechnology*, **26**:417–426, 2008. 20, 21, 24
- [69] H. PARSA, C. CHIN, P. MONGKOLWISETWARA, B. LEE, J. WANG, AND S. SIA. **Effect of Volume- and Time-Based Constraints on Capture of Analytes in Microfluidic Heterogeneous Immunoassays.** *Lab on a Chip*, **8**:2062–2070, 2008. 20, 24
- [70] B.K. LOK, Y.L. CHENG, AND C.R. ROBERTSON. **Protein Adsorption on Cross-Linked Polydimethylsiloxane Using Total Internal-Reflection Fluorescence.** *Journal of Colloid and Interface Science*, **9**:104–116, 1983. 22
- [71] T. GERVAIS AND K. JENSEN. **Mass Transport and Surface Reactions in Microfluidic Systems.** *Chemical Engineering Science*, **61**:1102–1121, 2006. 22, 23, 24
- [72] D.A. EDWARDS, B. GOLSTEIN, AND D.S. COHEN. **Transport Effects on Surface-Volume Biological Reactions.** *J. Math. Biol.*, **39**:533–561, 1999. 23
- [73] D.A. EDWARDS. **Estimating Rate Constants in a Convection-diffusion system With a Boundary Reaction.** *IMA J. Appl. Math.*, **63**:89–112, 1999. 23
- [74] KAPIL SUBRAMANIAM AND SUMAN CHAKRABORTY. **A semi-analytical model for species transport in combined electroosmotic and pressure driven microflows with surface adsorption-desorption reactions.** *Microfluidics and Nanofluidics*, **10**(4):821–829, 2011. 23, 24
- [75] R. W. GLASER. **Antigen-Antibody Binding and Mass Transport by Convection and Diffusion to a Surface: A Two-Dimensional Computer Model of Binding and Dissociation Kinetics.** *Analytical Biochemistry*, **213**(1):152–161, 1993. 23

REFERENCES

- [76] PETER SCHUCK AND ALLEN P. MINTON. **Analysis of Mass Transport-Limited Binding Kinetics in Evanescent Wave Biosensors.** *Analytical Biochemistry*, **240**(2):262–272, 1996. 23
- [77] M.L. YARMUSH, D.B. PATANKAR, AND D.M. YARMUSH. **An Analysis of Transport Resistances in the Operation of BIAcore(TM): Implications for Kinetic Studies of Biospecific Interactions.** *Molecular Immunology*, **33**:1203–1214, 1996. 23
- [78] LARS L. H. CHRISTENSEN. **Theoretical Analysis of Protein Concentration Determination Using Biosensor Technology under Conditions of Partial Mass Transport Limitation.** *Analytical Biochemistry*, **249**(2):153–164, 1997. 23
- [79] D. MYSZKA, T. MORTON, M. DOYLE, AND I. CHAIKEN. **Kinetic Analysis of a Protein Antigen-Antibody Interaction Limited by Mass Transport on an Optical biosensor.** *Biophys Chem*, **64**:127–137, 1997. 23
- [80] D. MYSZKA, X. HE, M. DEMBO, T. MORTON, AND B. GOLDSTEIN. **Extending the Range of Rate Constants Available From BIACORE: Interpreting Mass Transport-Influenced Binding Data.** *Biophysical Journal*, **75**:583–594, 1998. 23
- [81] T. MASON, A. PINEDA, C. WOFYSY, AND B. GOLDSTEIN. **Effective Rate Models for the Analysis of Transport-Dependent Biosensor Data.** *Mathematical Biosciences*, **159**:123–144, 1999. 23
- [82] BYRON GOLDSTEIN, DANIEL COOMBS, XIAOYI HE, ANGEL R. PINEDA, AND CARLA WOFYSY. **The influence of transport on the kinetics of binding to surface receptors: application to cells and BIAcore.** *Journal of Molecular Recognition*, **12**(5):293–299, 1999. 23
- [83] C. WOFYSY AND B. GOLDSTEIN. **Effective Rate Models For Receptors Distributed in a Layer Above a Surface: Applications to Cells and Biacore.** *Biophysical Journal*, **82**:1743–1755, 2002. 23
- [84] RASMUS HANSEN, HENRIK BRUUS, THOMAS H. CALLISEN, AND OLE HASSAGER. **Transient Convection, Diffusion, and Adsorption in Surface-Based Biosensors.** *Langmuir*, **28**(19):7557–7563, 2012. 23, 24
- [85] KONSTANTIN LEBEDEV, SALVADOR MAFE, AND PIETER STROEVE. **Convection, diffusion and reaction in a surface-based biosensor: Modeling of cooperativity and binding site competition on the surface and in the hydrogel.** *Journal of Colloid and Interface Science*, **296**(2):527–537, 2006. 24
- [86] GUOQING HU, YALI GAO, AND DONGQING LI. **Modeling micropatterned antigen-antibody binding kinetics in a microfluidic chip.** *Biosensors and Bioelectronics*, **22**(7):1403–1409, 2007. 24
- [87] HANA SIPOVA, DAVID VRBA, AND JIRI HOMOLA. **Analytical Value of Detecting an Individual Molecular Binding Event: The Case of the Surface Plasmon Resonance Biosensor.** *Analytical Chemistry*, **84**(1):30–33, 2011. 24
- [88] YALI GAO, GUOQING HU, FRANK Y. H. LIN, PHILIP SHERMAN, AND DONGQING LI. **An Electrokinetically-Controlled Immunoassay for Simultaneous Detection of Multiple Microbial Antigens.** *Biomedical Microdevices*, **7**:301–312, 2005. 24
- [89] BIBHAS ROY, TAMAL DAS, TAPAS K. MAITI, AND SUMAN CHAKRABORTY. **Effect of fluidic transport on the reaction kinetics in lectin microarrays.** *Analytica Chimica Acta*, **701**(1):6 – 14, 2011. 24
- [90] W.M. DEEN. *Analysis of Transport Phenomena.* Oxford University Press, New York, 2nd edition, 2012. 25
- [91] E. LAUGA, M. BRENNER, AND H. STONE. *Microfluidics: The No-slip Boundary Condition*, chapter 19, pages 1219–1240. Springer, 2007. 47
- [92] L. BOCQUET AND J. BARRAT. **Flow Boundary Conditions from nano to micro scales.** *Soft Matter*, **3**:685–693, 2007. 47
- [93] D. BONN, J. EGGERS, J. INDEKEU, J. MEUNIER, AND E. ROLLEY. **Wetting and Spreading.** *Reviews of Modern Physics*, **81**:739–805, 2009. 48
- [94] M. DENN. **Extrusion Instabilities and Wall Slip.** *Annual Review of Fluid Mechanics*, **33**:265–287, 2001. 48
- [95] ROMAN S. VORONOV, DIMITRIOS V. PAPAVALASSILOU, AND LLOYD L. LEE. **Slip length and contact angle over hydrophobic surfaces.** *Chemical Physics Letters*, **441**(4A):273 – 276, 2007. 48
- [96] CHRISTIAN SENDNER, DOMINIK HORINEK, LYDERIC BOCQUET, AND ROLAND R. NETZ. **Interfacial Water at Hydrophobic and Hydrophilic Surfaces: Slip, Viscosity, and Diffusion.** *Langmuir*, **25**(18):10768–10781, 2009. 48
- [97] P. THOMPSON AND S. TROIAN. **A General Boundary Condition for Liquid Flow at Solid Surfaces.** *Nature*, **389**:360–362, 1997. 48
- [98] CHIARA NETO, DREW R EVANS, ELMAR BONACCURSO, HANS-JÜRGEN BUTT, AND VINCENT S J CRAIG. **Boundary slip in Newtonian liquids: a review of experimental studies.** *Reports on Progress in Physics*, **68**(12):2859–2897, 2005. 48
- [99] DEREK C. TRETHERWAY AND CARL D. MEINHART. **Apparent fluid slip at hydrophobic microchannel walls.** *Physics of Fluids*, **14**(3):L9–L12, 2002. 48
- [100] P. JOSEPH AND P. TABLING. **Direct Measurement of the Apparent Slip Length.** *Physical Review E*, **71**:035303, 2005. 48
- [101] P. HUANG, J. GUASTO, AND K. BRUER. **Direct Measurement of Slip Velocities Using Three Dimensional Total Internal Reflection Velocimetry.** *Journal of Fluid Mechanics*, **566**:447–464, 2006. 48
- [102] LILIANE LEGER. **Friction Mechanisms and Interfacial Slip at Fluid-Solid Interfaces.** *Journal of Physics: Condensed Matter*, **15**:S19–S29, 2003. 48

REFERENCES

- [103] C. COTTIN-BIZONNE, S. JURINE, J. BAUDRY, J. CRASSOUS, F. RESTAGNO, AND E. CHARLAIX. **Nanorheology: An Investigation of the Boundary Condition at Hydrophobic and Hydrophilic Interfaces.** *Eur. Phys. J. E*, **9**:47–53, 2002. 48
- [104] C. BOUZIGUES, L. BOCQUET, COTTIN-BIZONNE C. CHARLAIX, E., B. CROSS, L. JOLY, A. STEINBERGER, C. YBERT, AND J. TABELING. **Using Surface Force Apparatus, Diffusion and Velocimetry to Measure Slip Lengths.** *Phil. Trans. R. Soc. A*, **366**:1455–1468, 2008. 48
- [105] C.D. HONIG AND W.A. DUCKER. **No Slip Hydrodynamic Boundary Condition for Hydrophilic Particles.** *Phys Rev Lett*, **98**:028305, 2007. 48
- [106] YINGXI ZHU AND STEVE GRANICK. **Limits of the Hydrodynamic No-Slip Boundary Condition.** *Phys. Rev. Lett.*, **88**:106102, Feb 2002. 48
- [107] ELMAR BONACCURSO, MICHAEL KAPPL, AND HANS-JÜRGEN BUTT. **Hydrodynamic Force Measurements: Boundary Slip of Water on Hydrophilic Surfaces and Electrokinetic Effects.** *Phys. Rev. Lett.*, **88**:076103, Feb 2002. 48
- [108] OLGA I. VINOGRADOVA AND GLEB E. YAKUBOV. **Dynamic Effects on Force Measurements. 2. Lubrication and the Atomic Force Microscope.** *Langmuir*, **19**(4):1227–1234, 2003. 48
- [109] LIWEN ZHU, PHIL ATTARD, AND CHIARA NETO. **Reliable Measurements of Interfacial Slip by Colloid Probe Atomic Force Microscopy. I. Mathematical Modeling.** *Langmuir*, **27**(11):6701–6711, 2011. 48
- [110] C. COTTIN-BIZONNE, B. CROSS, A. STEINBERGER, AND E. CHARLAIX. **Boundary Slip on Smooth Hydrophobic Surfaces: Intrinsic Effects and Possible Artifacts.** *Phys. Rev. Lett.*, **94**:056102, Feb 2005. 48
- [111] P. HUANG, J. GUASTO, AND K. BRUER. **Direct Measurement of Slip Velocities Using Three Dimensional Total Internal Reflection Velocimetry.** *Journal of Fluid Mechanics*, **566**:447–464, 2006. 48
- [112] C. I. BOUZIGUES, P. TABELING, AND L. BOCQUET. **Nanofluidics in the Debye Layer at Hydrophilic and Hydrophobic Surfaces.** *Phys. Rev. Lett.*, **101**:114503, 2008. 48
- [113] S.P. MCBRIDE AND B.M. LAW. **Viscosity dependent liquid slip at molecularly smooth hydrophobic surfaces.** *Phys. Rev. E*, **80**:060601, 2009. 48
- [114] A.P. BOWLES, C. HONIG, AND W. DUCKER. **No-Slip Boundary Condition for Weak Solid-Liquid Interactions.** *J. Phys. Chem. C*, **115**:8613–8621, 2011. 48
- [115] LIWEN ZHU, CHIARA NETO, AND PHIL ATTARD. **Reliable Measurements of Interfacial Slip by Colloid Probe Atomic Force Microscopy. III. Shear-Rate-Dependent Slip.** *Langmuir*, **28**(7):3465–3473, 2012. 48
- [116] J. P. ROTHSTEIN. **Slip on Superhydrophobic Surfaces.** *Annual Review of Fluid Mechanics*, **42**(1):89–109, 2010. 48
- [117] J.R.T. SNEDDON AND D. LOHSE. **Nanobubbles and micropancakes: gaseous domains on immersed substrates.** *J. Phys.: Condens. Matter*, **23**:133001, 2011. 49, 50
- [118] ABDELHAMID MAALI AND BHARAT BHUSHAN. **Nanobubbles and their role in slip and drag.** *Journal of Physics: Condensed Matter*, **25**(18):184003, 2013. 49
- [119] DEREK C. TRETHERWAY AND CARL D. MEINHART. **A generating mechanism for apparent fluid slip in hydrophobic microchannels.** *Physics of Fluids*, **16**(5):1509–1515, 2004. 49
- [120] YINGXI ZHU AND STEVE GRANICK. **Rate-Dependent Slip of Newtonian Liquid at Smooth Surfaces.** *Phys. Rev. Lett.*, **87**:096105, 2001. 49
- [121] DEREK C. TRETHERWAY AND CARL D. MEINHART. **Apparent fluid slip at hydrophobic microchannel walls.** *Physics of Fluids*, **14**(3):L9–L12, 2002. 49
- [122] J. OU, B. PEROT, AND J. ROTHSTEIN. **Direct velocity measurements of the flow past drag-reducing ultrahydrophobic surfaces.** *Physics of Fluids A*, **17**:103606, 2005. 49
- [123] C.-H. CHOI AND C.-JIN KIM. **Large Slip of Aqueous Liquid Flow over a Nanoengineered Superhydrophobic Surface.** *Physical Review Letters*, **96**(6):1–4, 2006. 49
- [124] P. JOSEPH, C. COTTIN-BIZONNE, J. BENPIT, C. YBERT, C. JOURNET, P. TABELING, AND L. BOCQUET. **Slippage of Water Past Superhydrophobic Carbon Nanotube Forests in Microchannels.** *Physical Review Letters*, **97**:156104, 2006. 49
- [125] A. MAALI, Y. PAN, B. BHUSAN, AND E. CHARLAIX. **Hydrodynamic drag-force measurement and slip length on microstructured surfaces.** *Physical Review E*, **85**:066310, 2012. 49
- [126] C. COTTIN-BIZONNE, E. BARENTIN, E. CHARLAIX, L. BOCQUET, AND J. BARRAT. **Dynamics of Simple Liquids at Heterogeneous Surfaces: Molecular Dynamics Simulations and Hydrodynamic Description.** *Eur. Biophysics Journal E*, **15**:427–438, 2004. 49
- [127] E. LAUGA AND A. DAVIS. **Hydrodynamic friction on fakir-like superhydrophobic surfaces.** *J. Fluid Mech.*, **661**:402–411, 2010. 49
- [128] R. SEEMANN, M. BRINKMANN, T. PFOHL, AND S. HERMINGHAUS. **Droplet Based Microfluidics.** *Rep. Prog. Phys.*, **75**:016601, 2012. 50
- [129] J. LEE, C. PARK, AND G. M. WHITESIDES. **Solvent Compatibility of Poly(dimethylsiloxane)-Based Microfluidic Devices.** *Anal. Chem.*, **75**:6544–6554, 2003. 50
- [130] R. DANGLA, F. GALLAIRE, AND C.N. BAROUD. **Microchannel deformations due to solvent-induced PDMS swelling.** *Lab on a Chip*, **10**(21):2972–2978, 2010. 50

REFERENCES

- [131] S. L. ANNA, N. BONToux, AND H. A. STONE. **Formation of dispersions using "flow focusing" in microchannels.** *Applied Physics Letters*, **82**(3):364–366, 2003. 51, 62, 76
- [132] EVA SANTINI, LIBERO LIGGIERI, LINDA SACCA, DANIELE CLAUSSE, AND FRANCESCA RAVERA. **Interfacial rheology of Span 80 adsorbed layers at paraffin oil–water interface and correlation with the corresponding emulsion properties.** *Colloids and Surfaces A: Physicochemical and Engineering Aspects*, **309**:270 – 279, 2007. 52
- [133] R.G. COX AND H. BRENNER. **The Slow Motion of a Sphere Through Viscous Fluid Towards a Plane Surface - II Small Gap Widths Including Inertial Effects.** *Chemical Engineering Science*, **22**:1753–1777, 1967. 54
- [134] Y. CHANG AND H. KEH. **Slow motion of a slip spherical particle perpendicular to two plane walls.** *Journal of Fluids and Structures*, **23**:647–661, 2006. 54
- [135] M. H. DAVIS. **Two Charged Spherical Conductors in a Uniform Electric Field: Forces and Field Strength.** *Quarterly Journal of Mechanics and Applied Mathematics*, **17**:499–511, 1964. 55, 68, 95
- [136] J. SJOBLom. *Encyclopedic Handbook of Emulsion Technology.* Marcel Dekker, New York, 2001. 61, 74
- [137] L.L. SCHRAMM. *Emulsions: Fundamentals and Applications in the Petroleum Industry.* Advances in Chemistry Series. American Chemistry Society, Washington, D.C., 1992. 61, 74
- [138] DJ McCLEMENTS. **Critical review of techniques and methodologies for characterization of emulsions stability.** *Critical Reviews in Food Science and Nutrition*, **47**(7), 2007. 61, 74
- [139] W.D. RISTENPART, J.C. BIRD, A. BELMONTE, F. DOLLAR, AND H.A. STONE. **Non-coalescence of oppositely charged drops.** *Nature*, **461**(7262):377–380, 2009. 63
- [140] J.C. BIRD, W.D. RISTENPART, A. BELMONTE, AND H.A. STONE. **Critical angle for electrically driven coalescence of two conical droplets.** *Physical Review Letters*, **103**(16), 2009. 63
- [141] B.S. HAMLIN, J.C. CREASEY, AND W.D. RISTENPART. **Electrically tunable partial coalescence of oppositely charged drops.** *Phys. Rev. Lett.*, **109**(9), 2012. 63
- [142] ABDou R. THIAM, NICOLAS BREMOND, AND JEROME BIBETTE. **Breaking of an Emulsion under an ac Electric Field.** *Physical Review Letters*, **102**(18):188304, 2009. 63
- [143] M. CHIESA, J. MELHEIM, A. PEDERSEN, S. INGEBRIGTSEN, AND G. BERG. **Forces Acting on Water Droplets Falling in Oil Under the Influence of an Electric Field: Numerical Predictions Versus Experiential Observations.** *European Journal of Mechanics B/Fluids*, **24**:717–732, 2005. 63
- [144] R AVEYARD AND D HAYDON. *An Introduction to the Principles of Surface Chemistry.* Cambridge University Press, 1973. 74
- [145] D. FENNELl EVANS AND HAKEAN WENNERSTROM. *The Colloidal Domain: Where Physics, Chemistry and Biology Meet.* Wiley-VCH, New York, 1999. 74
- [146] MILTON ROSEN. *Surfactants and Interfacial Phenomena.* Wiley, New York, third edition, 2004. 74
- [147] S.S. DUKHIN, G. KRETZSCHMAR, AND R. MILLER. *Dynamics of Adsorption at Liquid Interfaces: Theory, Experiment and Applications*, **1.** Elsevier, 1995. 74
- [148] P. JOOS AND V.B. FAInERMAN. *Dynamic Surface Phenomena.* VSP, 1999. 74
- [149] P.A. KRALCHEVSKY, K.D. DANOV, AND N.D. DENKOV. *Chemical Physics of Colloid Systems and Interfaces.* CRC Press, Boca Raton, FL, 2008. 74
- [150] D. A. EDWARDS, D. WASAN, AND H. BRENNER. *Interfacial Transport Processes.* Butterworth Heinemann, 1991. 74
- [151] B. V. DERJAGUIN. *Theory of Stability of Colloids and Thin Films.* Plenum Press: Consultants Bureau, New York, 1989. 74
- [152] L. SCRIVEN. **Dynamics of a fluid interface - equation of motion for Newtonian surface fluids.** *Chemical Engineering Science*, **12**(2):98–108, 1960. 75
- [153] B. NOSKOV AND D. GRIGORIEV. *Surfactants: Chemistry, Interfacial Properties, Applications.* Elsevier, 2001. 75
- [154] Y. ROTENBERG, L. BORUVKA, AND A.W. NEUMANN. **Determination of Surface Tension and Contact Angle From The Shapes of Axisymmetric Fluid Interfaces.** *Journal of Colloid and Interface Science*, **93**:169–183, 1983. 75
- [155] A. ADAMSON AND A. GAST. *Physical Chemistry of Surfaces.* John Wiley and Sons, Ltd., 6 edition, 1997. 75
- [156] P. HEIMENZ AND R. RAJAGOPOLAN. *Principles of Colloids and Surface Chemistry.* Marcel-Dekker, New York, 3 edition, 1997. 75
- [157] G. LOGLIO, U. TESEI, N. INNOCENTI, R. MILLER, AND R. CINI. **Non-equilibrium Surface Thermodynamics: Measurement of Transient Dynamic Surface Tension for Fluid-Fluid Interfaces by the Trapezoidal Pulse Technique.** *Colloids and Surfaces*, **57**:335–342, 1991. 75
- [158] J. BENJAMINS, A. CAGNA, AND E. LUCASSEN. **Viscoelastic properties of triacylglycerol/water interfaces covered by proteins.** *Colloids Surfaces A: Physicochem. Eng. Aspects*, **114**(245), 1996. 75
- [159] R. MYRVOLD AND F.K. HANSEN. **Surface elasticity and viscosity from oscillating bubbles measured by automatic axisymmetric drop shape analysis.** *J. Colloid Interface Sci.*, **207**(1):97–105, 1998. 75

REFERENCES

- [160] S. SHOJAEI-ZADEH, J.F. MORRIS, A. COUZIS, AND C. MALDARELLI. **Highly crosslinked poly(dimethylsiloxane) microbeads with uniformly dispersed quantum dot nanocrystals.** *J. Colloid Interface Sci.*, **363**(1):25–33, 2011. 76
- [161] J.T. CABRAL AND S.D. HUDSON. **Microfluidic approach for rapid multicomponent interfacial tensiometry.** *Lab on a Chip*, **6**(3):427–436, 2005. 76
- [162] J.D. MARTIN, J.N. MARHEFKA, K.B. MIGLER, AND S.D. HUDSON. **Interfacial Rheology Through Microfluidics.** *Adv. Materials*, **23**(3):426–432, 2011. 76
- [163] G.I. TAYLOR. **Disintegration of Water Droplets in an Electric Field.** *Proceedings of the Royal Society of London, A*, **280**:383–397, 1969. 78
- [164] P. BRAZIER-SMITH AND J. LATHAM. **Numerical Computations of the Dynamics of Disintegration of a Drop Situated in an Electric Field.** *Proceedings of the Royal Society of London, A*, **312**:277–289, 1969. 78
- [165] C.E. ROSENKILDE. **A Dielectric Drop in an Electric Field.** *Proceedings of the Royal Society of London, A*, **312**:473–494, 1969. 78
- [166] M. MIKSIS. **Shape of a Drop in an Electric Field.** *Physics of Fluids*, **24**:1967–1972, 1981. 78
- [167] J.D. SHERWOOD. **Breakup of Fluid Droplets in Electric and Magnetic Fields.** *J. Fluid Mech.*, **188**:133–146, 1988. 78
- [168] F. WOHLHUTER AND O.A. BASARAN. **Shapes and stability of pendant and sessile dielectric drops in an electric field.** *J. Fluid Mech.*, **235**:481–510, 1992. 78
- [169] O.A. BASARAN AND F. WOHLHUTER. **Effect of non-linear polarization on shapes and stability of pendant and sessile drops in an electric (magnetic) field.** *J. Fluid Mech.*, **244**:1–16, 1992. 78
- [170] E.J. STONE, J. LISTER, AND M. BRENNER. **Drops with conical ends in electric and magnetic.** *Proceedings of the Royal Society of London, A*, **455**:329–347, 1999. 78
- [171] N. DUBASH AND A. MESTEL. **Behavior of a conducting drop in a highly viscous liquid subject to an electric field.** *J. Fluid Mech.*, **581**:469–493, 2007. 78
- [172] D. RHODES AND E. YARIV. **The elongated shape of a dielectric drop deformed by a strong electric field.** *J. Fluid Mech.*, **664**:286–296, 2010. 78
- [173] E.M. FREER, K.S. KIM, G.G. FULLER, AND C.J. RADKE. **Shear and dilatational relaxation mechanisms of globular and flexible proteins at the hexadecane/water interface.** *Langmuir*, **20**(23):10159–10167, 2004. 80
- [174] P.A. RUHS, C. AFFOLTER, E.J. WINDHAB, AND P. FISCHER. **Shear and dilatational linear and nonlinear sub-phase controlled interfacial rheology of beta-lactoglobulin fibrils and their derivatives.** *J. Rheology*, **57**(3):1003–1022, 2013. 80
- [175] A.H. MARTIN, M.A.C. STUART, M.A. BOS, AND T. VAN VLIET. **Correlation between mechanical behavior of protein films at the air/water interface and intrinsic stability of protein molecules.** *Langmuir*, **21**(9):4083–4089, 2005. 80
- [176] A.C. CHAN AND P.J. CARTER. **Therapeutic antibodies for autoimmunity and inflammation.** *Nature Rev. Immun.*, **10**(5):301–316, 2010. 81
- [177] R.K. BRUMMITT, D.P. NESTA, L.Q. CHANG, S.F. CHASE, T.M. LAUE, AND C.J. ROBERTS. **Non-native Aggregation of an IgG1 Antibody in Acidic Conditions.** *J. Pharm. Sci.*, **100**(6):2087–2103, 2011. 81
- [178] J. McDONALD AND G. WHITESIDES. **Poly(dimethylsiloxane) as a Material for Fabricating Microfluidic Devices.** *Accounts of Chemical Research*, **35**:491–499, 2002. 94
- [179] KRASSIMIR D. DANOV, SIMEON D. STOYANOV, NIKOLAY K. VITANOV, AND IVAN B. IVANOV. **Role of surfactants on the approaching velocity of two small emulsion drops.** *Journal of Colloid and Interface Science*, **368**(1):342 – 355, 2012. 96

Declaration

I hereby declare that I have produced this thesis without the prohibited assistance of third parties and without making use of aids other than those specified; ideas taken over directly or indirectly from other sources have been identified as such. This paper has not previously been presented in identical or similar form to any other examination board.

The thesis work was conducted from September, 2007 to December, 2013 under the supervision of Professor Charles Maldarelli at The City College of New York.

Thomas F. Leary